# Spectroscopic investigation of the thermal stability of bound hydrogen in *a*-C : H

V. I. Ivanov-Omskiĭ, G. S. Frolova, and S. G. Yastrebov

*A. F. Ioffe Physicotechnical Institute, Russian Academy of Sciences, St. Petersburg*
(Submitted December 14, 1996)
Pis'ma Zh. Tekh. Fiz. **23**, 1–7 (April 12, 1997)

Equilibrium between free and bound hydrogen in amorphous hydrogenated carbon has been investigated by infrared spectroscopy. A quasireversible departure of hydrogen from the bound state is observed. The activation energy of the bound–quasifree hydrogen chemical reaction and the rate of return of hydrogen to the bound state are estimated. An energy diagram is proposed for the bound–quasifree hydrogen reaction. © *1997 American Institute of Physics.*
[S1063-7850(97)00104-3]

Hydrogenated amorphous carbon (*a*-C : H) is widely used in technology because of its remarkable properties, such as high electrical resistance, chemical stability, optical transparency over a wide range of wavelengths, and attractive tribological characteristics. These characteristics are commonly attributed to the hydrogen content in *a*-C : H in different states. Bound hydrogen can easily be detected from its infrared vibrational spectrum,[1] but free hydrogen can be detected only in thick films because of the low sensitivity of the nuclear magnetic resonance technique. In addition, the problem of the ''free'' state of hydrogen in *a*-C : H remains unresolved.

In the present paper we attempt to explain the ''free'' state of hydrogen in *a*-C : H by making an infrared spectroscopic analysis of the equilibrium between bound and free hydrogen. The optical transmission in the region of the vibrational frequency of carbon–hydrogen bonds in *a*-C : H was measured as a function of the aftergrowth annealing temperature. Layers of *a*-C : H were prepared by magnetron sputtering in an argon–hydrogen plasma (4 : 1) at a pressure of 10 mTorr in the working chamber. The substrate temperature was 200 °C. The argon ion energy was about 100 eV. The *a*-C : H layers were deposited on silicon substrates. Measurements of the direct transmission were made using a Specord 751R dual-beam spectrophotometer.

A typical fragment of the transmission spectra of *a*-C : H in the region of stretching vibrations of the C–H bonds is shown in Fig. 1. The band structure indicates that $sp^3$ carbon bonds predominate in the material.

The samples were annealed in vacuum at temperatures of 100–450 °C in both isochronous and isothermal regimes. The effect of annealing on the hydrogen state in the *a*-C : H layers was assessed by converting the transmission spectra to the optical density (the logarithm of the transmission coefficient) at the wavelength corresponding to the maximum of the absorption band. It was assumed that the film thickness does not depend on the annealing time and that the absorption coefficient depends linearly on the concentration of C–H bonds in the *a*-C : H film, i.e., the temperature dependence of the optical density corresponds to the temperature dependence of the bound hydrogen concentration. Figure 2 shows the optical density of the vibrational band of bound hydrogen as a function of the temperature of isochronous annealing for 1 h for two samples. For comparison, Fig. 2 also shows published data on the temperature dependence of the hydrogen concentration in *a*-C : H (Ref. 2). It can be seen that our temperature dependences of the hydrogen concentration agree reasonably well with the published data obtained by direct determination of the hydrogen concentration. Assuming that the decrease in the bound hydrogen concentration, obtained from the infrared spectra, is caused by its transition to a different state, we can write the temperature dependence of the hydrogen concentration in this state $N$ in the form

$$N = N_0(1 - \exp(-E_1/kT)), \tag{1}$$

where $E_1$ is the activation energy of the transition, $N_0$ is the concentration of bound hydrogen, $T$ is the temperature, and $k$ is Boltzmann's constant. Fitting curves for $E_1 \sim 0.5 \pm 0.2$ eV, shown by the solid curves in Fig. 2, gives reasonable agreement with experiment. Bearing in mind the amorphous nature of the material and the limited temperature range of the measurements, we were forced to confine ourselves to the accuracy given above. It can also be seen that the bound hydrogen state disappears as a result of annealing at temperatures of the order of 400–450 °C for 1 h, which also agrees reasonably well with published.[2]

However, after some time, the hydrogen bound state was found unexpectedly to be restored, even at room temperature. This circumstance indicated that, as a result of thermal annealing in vacuum, hydrogen leaving the bound state remains in the sample, without moving very far from its initial position. Figure 3 shows time dependences of the optical density near the vibrational frequency band of bound hydrogen at two temperatures, for *a*-C : H samples annealed first at $T = 450$ °C until the band disappeared completely (Fig. 2). It can be seen that the rate of recovery of the optical density increases with temperature. This recovery of the band suggests that a quasireversible process takes place under annealing, which may involve the thermal excitation of bound hydrogen to a state whose characteristic frequencies are not recorded in the spectral range studied. Note that not only the intensity, but also the profile of the band is restored.

The activation energy $E_1$ correlates reasonably well with the difference between the energy for the detachment of hydrogen from molecules such as ethylene $C_2H_6$, 5.2 eV, and the energy of formation of a free hydrogen molecule, 4.5 eV (Ref. 3). Assuming that the activation energy is the barrier

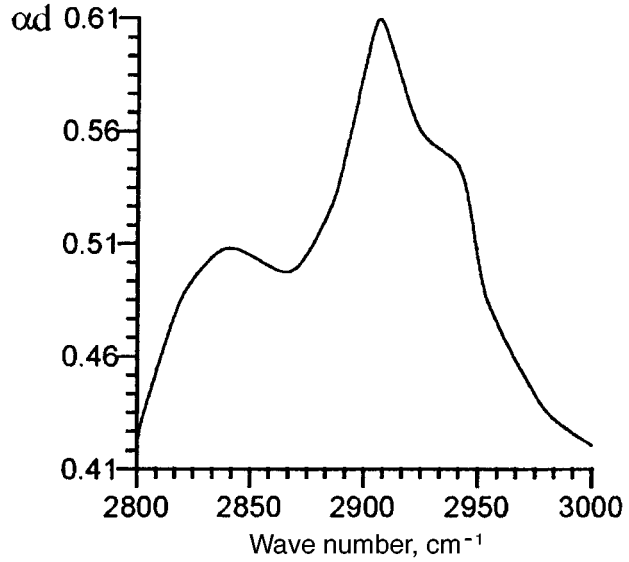


FIG. 1. Optical density ($\alpha d$) of the vibrational band of the C–H bond in $a$-C : H.

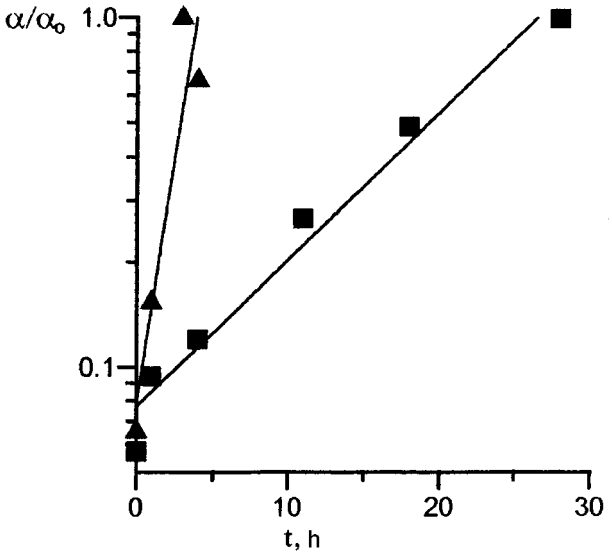


FIG. 3. Kinetics of recovery of the optical density of the band normalized to its maximum $\alpha_0$. The squares and triangles give the experimental data for the recovery of the sample at room temperature and 150 °C, respectively. The solid curves give the result of an exponential interpolation.

separating the bound and unbound hydrogen states, we can construct an energy diagram of the process, as shown in Fig. 4. The value of $E_2$, which determines the barrier height for the reverse reaction of recovery of the hydrogen bound state, can be estimated using the equation for the absolute reaction rate

$$V(T)=V_0\exp(-E_1/kT).$$

The exponential behavior of the curves in Fig. 3 agrees with this equation. Assuming that the preexponential factor $V_p$ does not depend on temperature, we have for the two temperatures $T_1$ and $T_2$:

$$E_2=k(T_1T_2/(T_1-T_2))\ln(V_1/V_2).$$

The ratio $V_1/V_2$ can be determined from the data plotted in Fig. 3. As a result, we obtain the estimate 0.15 eV for $E_2$. If

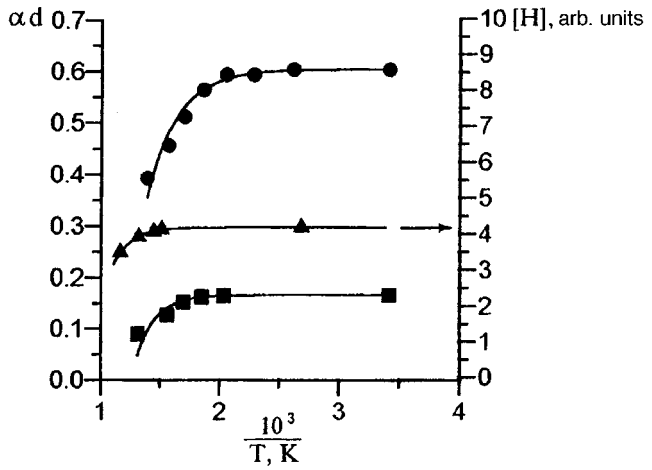


FIG. 2. Optical density of the band versus one-hour annealing temperature. The squares and circles gives the experimental points for two $a$-C : H samples and the triangles give the published data. The solid curves give the result of fitting *1* to the experimental points.

we attribute the reverse reaction to hydrogen tunneling to the bound state, we can estimate the order-of-magnitude width of the barrier between states *1* and *2* shown in Fig. 4. For this purpose, we write the frequency of the tunneling events as $\omega=\omega_0\exp(-d/d_0)$, where $d_0=\hbar/(2m_pE_2)^{0.5}$ ($\hbar$ is Planck's constant and $m_p$ is the proton mass). The frequency $\omega_0$ can be taken as the natural frequency of an oscillator with the binding energy $E_2$ corresponding to state *2*: $\omega_0=E_2/\hbar=2.2\times10^{14}$ s$^{-1}$. This procedure gives the barrier width $d\sim1.5$ Å, which corresponds to the distance between hydrogen in the excited state and its initial position. The similarity between the estimate and the half-width of a graphite ring suggests that fragments of the planes of the graphite-like component of the $a$-C : H structure may act as a possible storage area for the thermally excited hydrogen. The order-of-magnitude excited-state binding energy of hydrogen ($\sim0.15$ eV) is typical of the van der Waals forces. Such a bond may be expected in the interaction between hydrogen and an easily-polarizable $\pi$-electron system of graphite clusters. As a result of this interaction, hydrogen is adsorbed on graphite-like structure fragments, formed by carbon atoms in $sp^2$-states. With decreasing temperature, the hydrogen is transferred to the ground state, becoming bound to carbon atoms in the $sp^3$-state by tunneling through the barrier. Thus, at temperatures below 450 °C the hydrogen does not leave the $a$-C : H but is in bound or adsorbed states. We may thus assume that in the normal state, $a$-C : H contains no free hydrogen.

It should be stressed that these estimates of the parameters of the proposed model do not claim to be material constants, since they depend very much on the sample history, such as the substrate temperature during growth of the film.[2] These estimates merely serve to demonstrate the plausibility

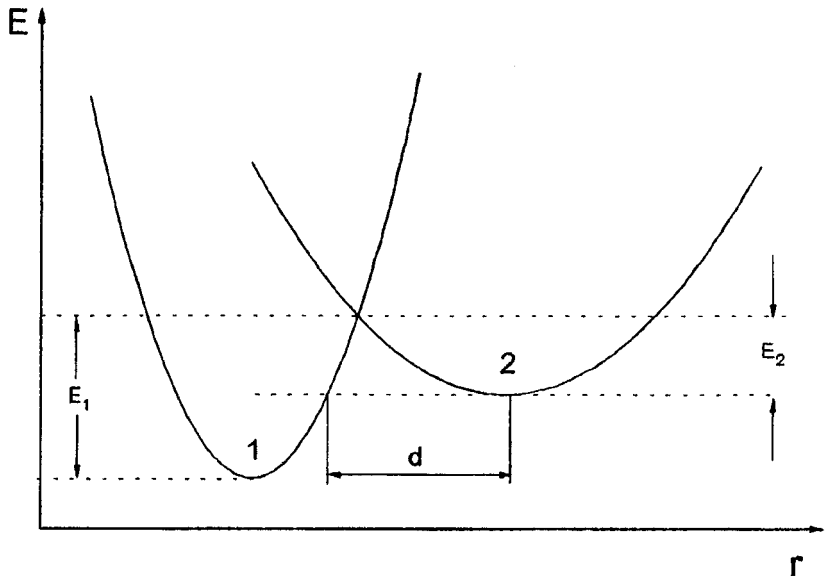


FIG. 4. Energy diagram showing the transition of hydrogen from the quasifree state *2* to the bound state *1*.

of the model and its suitability for interpolation for a given material technology.

This work was supported by Grant No. 96-02-16851-a from the Russian Fund for Fundamental Research and by a grant from the University of Arizona.

[1] A. Grill and V. Patel, Appl. Phys. Lett. **60**, 2089 (1992).
[2] A. Grill, in *Synthetic Diamond: Emerging CVD Science and Technology*, edited by K. Spear and J. P. Dismukes (Wiley, New York, 1994), p. 130.
[3] T. D. Moustakis, *ibid*, p. 145.

Translated by R. M. Durham

# Unbounded increase in the dimension of chaotic attractors in linear filtering

A. A. Kipchatov and E. L. Kozlenko

*N. G. Chernyshevskiĭ State University, Saratov; ''Kolledzh'' State Education and Science Center*
(Submitted November 13, 1996)
Pis'ma Zh. Tekh. Fiz. **23**, 8–13 (April 12, 1997)

An analysis is made of the limiting possibilities for adding complexity to chaotic oscillations in high-order filters. It is found that the limiting dimension of chaotic oscillation attractors in linear filters may increase to infinity, so that deterministic chaotic test oscillations with any desired dimension can be generated. © *1997 American Institute of Physics.* [S1063-7850(97)00204-8]

It has been established[1–6] that linear radiophysical and digital filters may add complexity to chaotic oscillations, i.e., they may cause the attractor trajectories to become entangled and increase their dimensions. Two ways of making attractors more complex are feasible: 1) for finite-response filters, the attractor trajectories reconstructed from output oscillations become elongated and repeatedly folded but their fine structure is conserved and their dimension only increases to finite scales of observation and is conserved for $\varepsilon \to \infty$ (observable increase in dimension); 2) for infinite-response filters, the trajectories of the reconstructed attractor become stratified in a fractal fashion and their dimension actually increases.[6] The increase in dimension for first-order filters is postulated to be unity, according to the hypothesis put forward by Badii and Politi,[1] and this is supported by experimental observations.[1,2,5] For higher-order filters however, the increase in dimension is unclear. In the present paper, we analyze the limiting possibilities for adding complexity to chaotic oscillations in high-order filters.

By analogy with Ref. 6, we consider the simplest chaotic oscillations generated by a quadratic map

$$x_n = 1 - \lambda x_{n-1}^2 . \tag{1}$$

For $\lambda = 1.9$ advanced chaotic oscillations occur in the system (1), and the series $\{x_n\}$ covers the interval $[-1,1]$ almost everywhere. The dimension of the attractor of these oscillations clearly tends to 1 from below.

The simplest first-order recursive filter has the form

$$z_n = \alpha z_{n-1} + x_n , \tag{2}$$

where $z_n$ is the output signal, $x_n$ are the input oscillations, and $\alpha$ is a coefficient determining the cutoff frequency of the filter. This type of digital filter corresponds to radio filters of the type $\dot{z} = \eta z + x$. The mechanism for increasing the complexity of chaotic oscillation attractors as they propagate through a first-order recursive filter, resulting in fractal stratification of the attractor, was analyzed in Ref. 6. Because of the linearity of these filters, the transition to $i$th-order filters can be made by a simple series connection of $i$ recursive first-order filters. We then obtain the chain

$$z_{n,i} = \alpha_i z_{n-1,i} + z_{n,i-1} , \tag{3}$$

$$z_{n,0} = x_n ,$$

where $i$ is the order number of the filter in the chain. Attractors reconstructed by the time delay method[7] from the output oscillations of a chain of recursive filters can be analyzed either qualitatively, using the attractor projections, or quantitatively, using their correlation dimension. However, neither method can reliably identify the level of complexity of the oscillations because of the increase in the dimension of the phase space and the substantial mixing of the attractor points. We therefore selected a method of visual analysis of the attractor structure using multiple Poincaré cross sections.

Clearly, the cross section of a volume gives a surface, the cross section of this surface gives a line, and the cross section of the line gives a point. By making successive cross sections, we can therefore obtain simple geometric transforms suitable for visual identification. The results of an analysis of the structure of the reconstructed attractors can be summarized as follows. A single recursive filter transforms an attractor from a line with $\alpha = 0$ (see Figs. 1a and 1d) to a surface with $\alpha \to 1$ (see Figs. 1b and 1e). The resulting attractor, reconstructed in three-dimensional phase space $(z_n, z_{n+1}, z_{n+2})$, is a parabolic trough (see Fig. 1f), whose structure is formed by lines of Poincaré cross sections. The entire surface is only realized for $\alpha \to 1$ (the filter cutoff frequency tends to 0). At higher filter cutoff frequencies, the surface of the trough becomes widely spaced and its structure is not observed so clearly (see Fig. 1b). In estimates of the correlation dimension, this has the result that a local slope, rather than a plateau, will be observed on the correlation interval, i.e., the dimension will increase from 1 on observation scales comparable with the attractor size to 2 for $\varepsilon \to 0$. It is thus clear that such complexity is impossible for periodic oscillations, since the finite number of points of which the periodic attractor consists, no matter how they are rearranged in phase space, cannot produce any fractal structure and thus does not add complexity to the attractor, and its dimension is conserved.

It then follows that oscillations whose attractor is clearly identified as a surface must be present at the exit of the first filter in order to identify the transformation of the attractor structure by a second-order filter. The propagation of oscillations through a second-order filter was therefore analyzed for $\alpha_1 = 0.8$. For $\alpha_2 = 0.1$, the filter gives a pattern of fractal stratification of the attractor surface (see Fig. 1c) in the reconstructed three-dimensional space, similar to the fractal stratification of the line for the first-order filter (see Fig. 1b). The relative stratification increases with increasing $\alpha_2$ and for $\alpha_2 = 0.8$, the double cross section of the four-dimensional embedding space $(z_n, z_{n+1}, z_{n+2}, z_{n+3})$ again yields a line

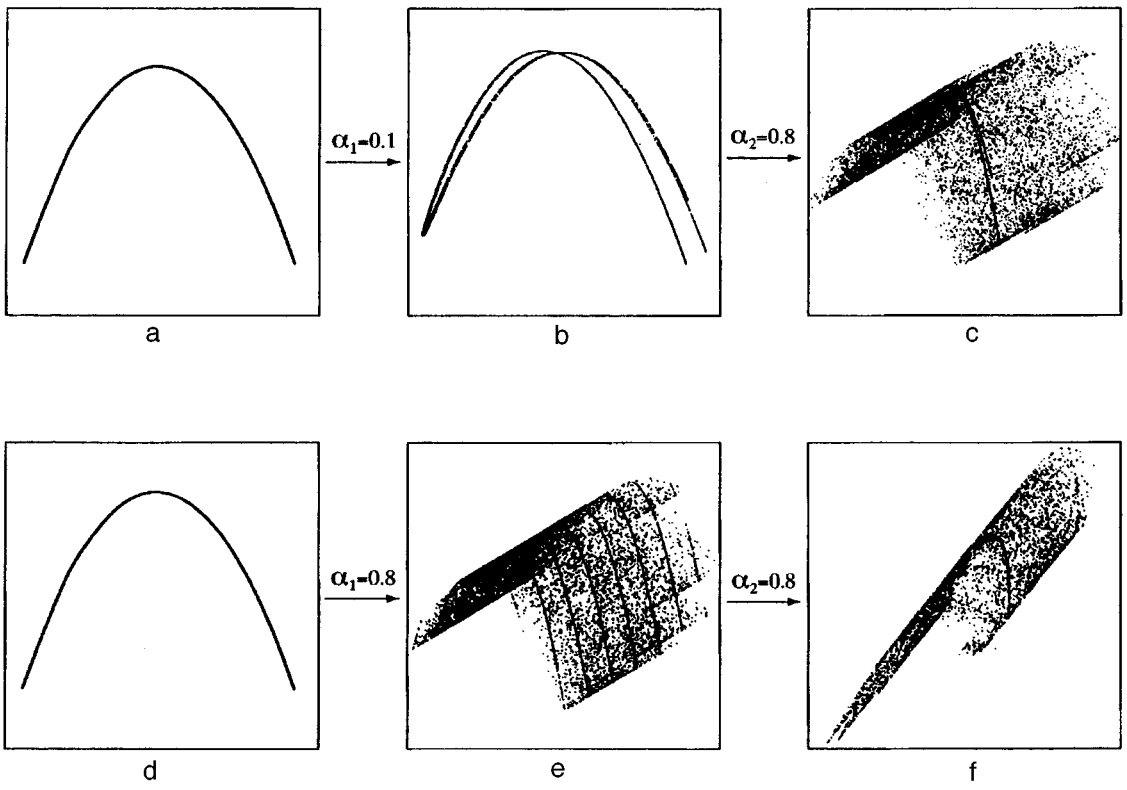


FIG. 1. Evolution of the attractor of a quadratic map during linear filtering: a, d — attractor of the input signal (quadratic parabola); b — attractor of the signal after passage through a single recursive filter, in the space $(x_n, x_{n+1}, x_{n+2})$ (for convenience of observation, the attractor is rotated relative to the axes), with the filter parameter $\alpha_1 = 0.1$; e — attractor of the signal after passage through a single recursive filter in the space $(x_n, x_{n+1}, x_{n+2})$ (the attractor is rotated relative to the axes), with the filter parameter $\alpha_1 = 0.8$, showing several cross sections along the coordinate $x_{n+1}$; c — attractor of the signal after passage through two recursive filters, in the space $(x_n, x_{n+1}, x_{n+2})$ (the attractor is rotated relative to the axes), with the filter parameters $\alpha_1 = 0.8$, $\alpha_2 = 0.1$, and the cross section coordinate $x_{n+1} = 0.2$; f — attractor of the signal after passage through two recursive filters in the space $(x_n, x_{n+1}, x_{n+2})$ (the attractor is rotated relative to the axes), with the filter parameters $\alpha_1 = 0.8$, $\alpha_2 = 0.8$, the coordinate of the first cross section is $x_{n+3} = 0.2$ and that of the second cross section $x_{n+1} = 0.2$.

(parabola), which indicates that the single cross section is a parabolic trough and the entire attractor is a three-dimensional volume (see Fig. 1f). This qualitative similarity between the topological structures of the attractors of initial unfiltered chaotic oscillations and the Poincaré cross sections of the attractor of chaotic oscillations after propagation through the filters, clearly illustrates the recurrence period of the increase in complexity of the chaotic oscillations as they propagate through high-order filters. The addition of each successive recursive filter yields qualitatively similar patterns of increasing complexity: the first first-order filter transforms a line into a surface by superfractalization, the second filter fractally stratifies the surface, transforming it into a three-dimensional volume, and the $n$th filter causes fractal stratification of the $n$-dimensional volume, and transforms it into an $n+1$-dimensional volume. The self-similar fractal structure of the attractor complexity as the order of the recursive filter increases, indicates that the nature of the initial signal is of fundamental importance in the filtering of chaotic oscillations. The mixing of the attractor trajectories (points) characteristic of chaos is selected by the filter as a fractal stratification of the attractor, where this stratification takes place in the direction of an additional degree of freedom coupled to the filter.

It can therefore be confirmed that the limiting dimension of the attractors of chaotic oscillations after passage through a filter is

$$S_{\text{out}} = D_{\text{in}} + i, \tag{4}$$

where $i$ is the order of the filter. Consequently, the dimension of the attractors of chaotic oscillations in linear filters may be increased to infinity, so that determinate test chaotic oscillations can be generated with any desired dimension.

At this point, the concept of limiting dimension should be specified, since an attractor generated as a result of recursive filtering is an inhomogeneous (or multifractal) structure, i.e., having different scales in different directions. This inhomogeneity is uniquely related to the filter coefficients $\alpha_i$, and becomes smaller as they increase. In addition, the dimension (capacity, information dimension, correlation dimension, and so forth) is by definition the exponent $D$ in the similarity relation $N(\varepsilon) = k\varepsilon^D$, as $\varepsilon \to 0$. Thus, the limiting dimension is taken here to mean the dimension which may be obtained for large $\alpha_i$ (weak inhomogeneity) and $\varepsilon \to 0$ (fine structure resolution). If the length of the data representation and their accuracy are finite, the dimension is determined in a bounded range of variation of $\varepsilon$, and for inhomogeneous attractors reconstructed after recursive filters, the

dimension is obtained as a function of the scale of spatial observation $D(\varepsilon)$ (Ref. 9), which decreases with increasing $\varepsilon$. When calculated using observable data, the limiting dimension may well not be achieved. In any case however, an unbounded increase in dimension is observed in the limit of strong filtering and infinite resolution and thus, the filtering of chaotic oscillations is one of the probable mechanisms for the onset of deterministic high-dimension oscillations, almost indistinguishable from noise, in real systems.

This work was supported financially by the Russian Fund for Fundamental Research (Grant No. 96-02-16753).

[1] R. Badii *et al.*, Phys. Rev. Lett. **60**, 979 (1988).
[2] F. Mitschke, M. Moller, and W. Lange, Phys. Rev. A **37**, 4518 (1988).
[3] J. Theiler and S. Eubank, Chaos **3**, 771 (1993).
[4] T. Sauer and J. Yorke, Int. J. Bifurcations Chaos **3**, 737 (1993).
[5] A. Kipchatov, L. Krasichkov, and A. Andrushkevich, *Nonlinear Circuits and Systems* [in Russian], Vol. 2, Moscow (1992), pp. 308–317.
[6] A. Kipchatov and L. Krasichkov, Pis'ma Zh. Tekh. Fiz. **21**(4), 1 (1995) [Tech. Phys. Lett. **21**, 131 (1995)].
[7] F. Takens, in *Dynamical Systems and Turbulence*, Springer Lecture Notes in Mathematics, Vol. 898, edited by D. A. Rand and L.-S. Young (Springer-Verlag, Berlin, 1980), p. 355.
[8] P. Grassberger and I. Procaccia, Phys. Rev. Lett. **50**, 346 (1983).
[9] A. Kipchatov, Pis'ma Zh. Tekh. Fiz. **21**(15), 90 (1995) [Tech. Phys. Lett. **21**, 627 (1995)].

Translated by R. M. Durham

# Materials with mixed conductivity in a $HfO_2$–$YO_{1.5}$–$PrO_{1.5}$ system

M. V. Kalinina and P. A. Tikhonov

*I. V. Grebenshchikov Institute of Silicate Chemistry, Russian Academy of Sciences, St. Petersburg*
(Submitted October 28, 1996)
Pis'ma Zh. Tekh. Fiz. **23**, 14–17 (April 12, 1997)

The phase composition and electrical properties of $HfO_2$–$YO_{1.5}$–$PrO_{1.5}$ systems have been determined. Studies have been made to identify how the specific electrical properties of these solid solutions are influenced by praseodymium oxide additives when the yttrium oxide content is constant, and how they are influenced by the interchangeability of praseodymium oxide with yttrium oxide when the hafnium dioxide content is kept constant. © *1997 American Institute of Physics.* [S1063-7850(97)00304-2]

As a result of recent investigations it has been shown that $HfO_2(ZrO)_2$–$Ln_2O_3$ solid solutions can be used to obtain a wide range of materials exhibiting different proportions of electron and ionic conductivity. According to our preliminary studies of the $HfO_2$–$YO_{1.5}$–$PrO_{1.5}$ system, the solid solutions exhibit fairly high electrical conductivity and a high proportion of electron conduction, which is important for the development of materials for high-temperature engineering. In addition, purely ionic conductors, used as solid electrolytes in high-temperature fuel cells and as oxygen detectors, have also been observed in this system.

The phase composition and electrical properties were determined for the following pseudobinary sections: $(HfO_2)_{0.5}(Pr_{1-y}Y_yO_{1.5})_{0.5}$, $(HfO_2)_{0.75}(Pr_{1-y}Y_yO_{1.5})_{0.25}$, and $(YO_{1.5})_{0.095}[(HfO_2)_{1-y}(YO_{1.5})_y]_{0.905}$.

The calculated mixtures of the initial oxides were pressed into tablets using a polyvinyl alcohol solution and were baked in an SShVL vacuum furnace at 1800 °C for 3 h (~0.1 Pa vacuum). The furnace and samples were then cooled rapidly and the samples subjected to *x*-ray phase analysis. Figure 1 shows the results obtained assuming that the $HfO_2$ monoclinic phase fixed at room temperature was in the tetragonal modification at 1800 °C.

A wide range of fluorite-type solid solutions is characteristic of this system.

Regions of existence of a tetragonal solid solution and a two-phase region of existence of tetragonal and cubic solid solutions were constructed in this three-component system. The boundaries of a heterogeneous region of coexisting fluorite-type and pyrochlore-type cubic solid solutions were determined.

The phase relationships in this system are fairly similar to those of the $HfO_2$–$DyO_{1.5}$–$PrO_{1.5}$ system described earlier.[1]

The ''blocking electrode'' method[2,3] was used to measure the conductivity in the 800–1400 °C range, separated into the ionic and electron components.

Isotherms of the electron, ionic, and total conductivity as a function of the sample composition were constructed for the first pseudobinary section of the three-component system at 1400 °C (Fig. 2). It can be seen that the sample having the composition $(HfO_2)_{0.5}$–$(PrO_{1.5})_{0.5}$ exhibits predominantly electronic conductivity. When praseodymium is replaced by yttrium, an increase in the ionic component is observed. This continuous increase in the ionic component confirms that this system has a wide range of existence of fluorite-structure solid solutions. In the region rich in hafnium dioxide, the

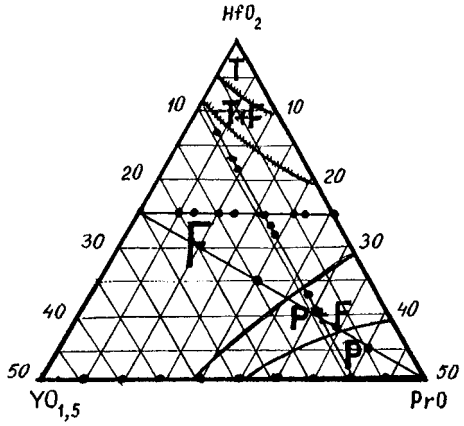


FIG. 1. Isothermal section (1800 °C) of $HfO_2$–$YO_{1.5}$–$PrO_{1.5}$ phase diagram.

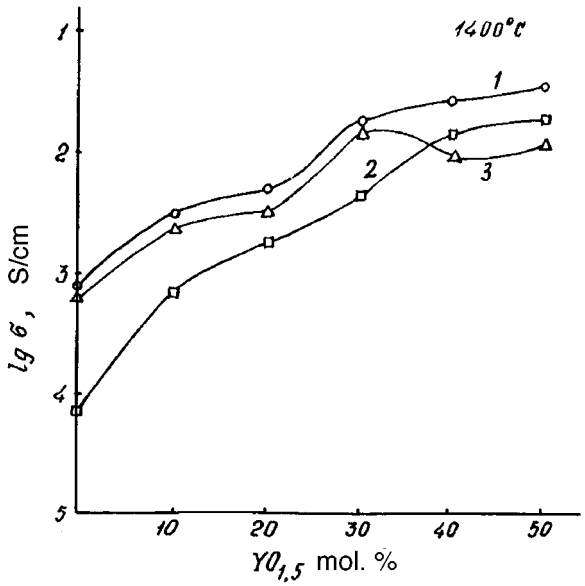


FIG. 2. Electrical properties of solid solutions for $(HfO_2)_{0.5}(Pr_{1-y}Y_yO_{1.5})_{0.5}$ section (1400 °C, high-purity helium). Notation: *1* — total conductivity, *2* — ionic conductivity, and *3* — electronic conductivity.

 1063-7850/97/040257-02$10.00  

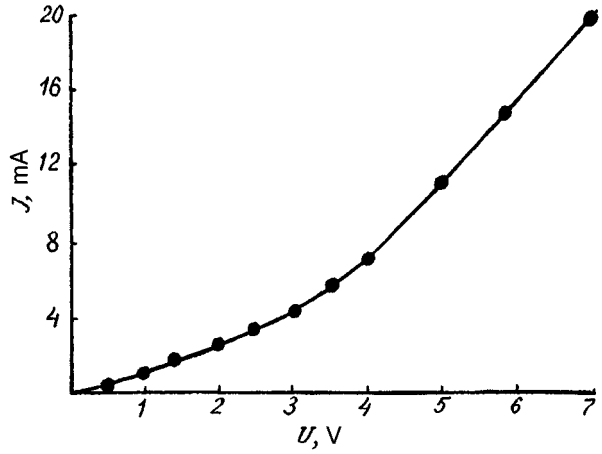


FIG. 3. Current-voltage characteristic of a sample having the composition $(HfO_2)_{0.828}(YO_{1.5})_{0.095}(PrO_{1.5})_{0.077}$ in a high-purity helium atmosphere at 1000 °C.

fluorite-type solid solutions are solid electrolytes, i.e., they possess predominantly ionic conductivity.

This behavior is also confirmed by the current-voltage characteristics for the appropriate samples. Figure 3 shows the current-voltage characteristic of a $(HfO_2)_{0.828}(PrO_{1.5})_{0.077}(YO_{1.5})_{0.095}$ sample in a high-purity helium atmosphere (dc current). The dissociation potential of 2.3 V is typical of $ZrO_2$ and $HfO_2$ fluorite-type solid solutions.[4]

These investigations have shown how the specific electrical characteristics of these ternary solid solutions are influenced by praseodymium oxide additives when the yttrium oxide content is kept constant, and also how they are influenced by the interchangeability of praseodymium oxide and yttrium oxide when the hafnium dioxide content is kept constant.

Thus, once we know the specific relationships between the structure and the properties, we can produce materials with controllable properties for different applications in modern technology.

[1] M. V. Kravchinskaya, P. A. Tikhonov, A. K. Kuznetsov, and F. Ganits, Dokl. Akad. Nauk SSSR **238**, 583 (1978).
[2] L. A. McClaine and C. P. Coppel, J. Electrochem. Soc. **113**, 80 (1966).
[3] P. A. Tikhonov. A. K. Kuznetsov, and M. V. Kravchinskaya, Zavod. Labor. No. 7 (1978).
[4] P. A. Tikhonov. A. K. Kuznetsov, M. D. Krasil'nikov, and M. V. Kravchinskaya, Zh. Fiz. Khim. **L1**(1), 143 (1977).

Translated by R. M. Durham

# Rearrangement of the shock wave structure in a decaying discharge plasma

A. S. Baryshnikov, I. V. Basargin, E. V. Dubinina, and D. A. Fedotov

*A. F. Ioffe Physicotechnical Institute, Russian Academy of Sciences, St. Petersburg*
(Submitted December 17, 1996)
Pis'ma Zh. Tekh. Fiz. **23**, 18–22 (April 12, 1997)

A study has been made of the change in the structure of a shock wave in a decaying discharge plasma with Mach numbers between 1.2 and 2. A novel method is proposed to investigate the rearrangement of the shock wave structure under transient conditions. The times of the main processes responsible for this effect are determined. © *1997 American Institute of Physics.* [S1063-7850(97)00404-7]

Rearrangement of the shock wave structure in a glow discharge plasma is a well-known effect.[1–3]. The main density discontinuity, whose amplitude decreases in the plasma, is accompanied by additional regions of abruptly increasing pressure and density. If the physical mechanism responsible for the effect were understood, it would be possible to find methods of predicting and controlling it. In the present paper, we study the structure of a shock wave in a discharge with Mach numbers between 1.2 and 2. Such an analysis will help towards understanding the physical mechanism of the effect for a moderate-intensity shock wave. Once the mechanism has been clarified, the main characteristics of the effect can then be determined quite easily for strong shock waves.

Various hypotheses have now been put forward as to the nature of the physical mechanism. In broad terms, these hypotheses can be divided into pure electrodynamic ones,[3,4] which merely attribute the effect to the presence of a charged component, especially electrons, and physicochemical hypotheses,[5] which explain the effect by means of complex physicochemical kinetics for conversion of heavy particles in the plasma. In order to unravel the complex pattern of the effect, we note that, under transient conditions, processes of a different nature usually have different time scales. By studying the entire spectrum of characteristic times for rearrangement of the structure, we can draw some conclusions on the main processes and the principal components responsible for the effect.

Transient conditions are created experimentally by switching off an external power supply whereby, after a certain time, the various components, electrons, ozone, and excited atoms, gradually disappear and the air regains its initial composition. The decay time is the sum of the delay time for launching the shock wave and the time taken for it to propagate to a particular spatial point. In each series of experiments, the delay time is increased and the shock wave structure is studied after every increase in the decay time. The amplitude of the structure peaks and the amplitudes of its harmonics are studied after the distribution has been expanded as a Fourier series. Only the change in the amplitude of the first peak at maximum shock wave velocity was investigated in Ref. 6. The analysis is complicated by the fact that a large amount of information must be processed because the results of separate experiments are analyzed for each time interval. The analysis is performed on a personal computer using well-known mathematical methods of processing experimental information.[7]

Figures 1 and 2 show typical pressure distributions in a shock wave in a glow discharge (Fig. 1a) and the pressure distribution in air without a discharge (Fig. 1b), as well as the change in the amplitude of the first and second harmonics of a Fourier-series expansion of the distribution as a function of the decay time (Figs. 2a and 2b).

The most important result is that the time taken to con-

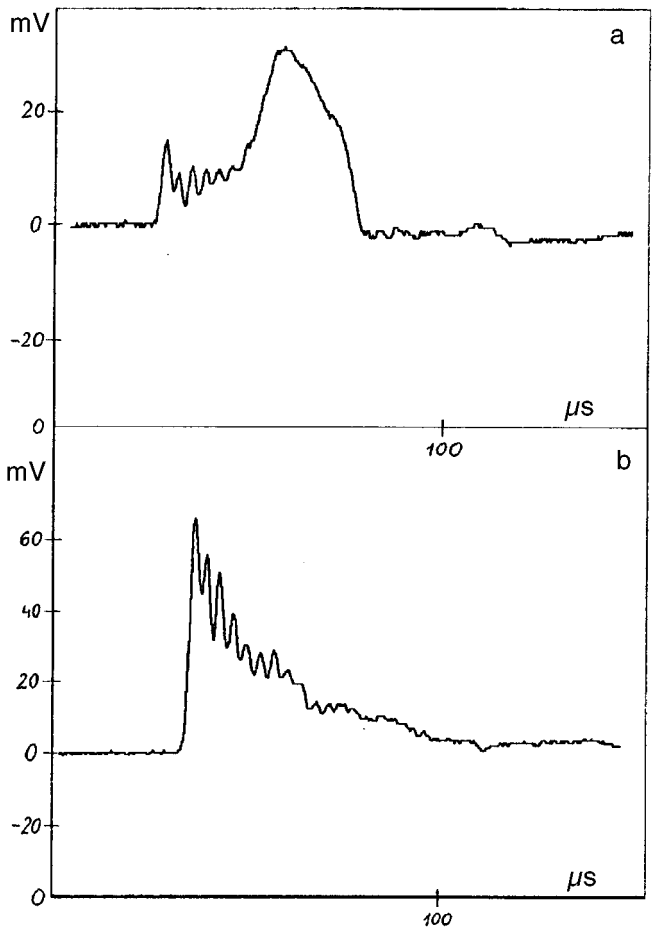


FIG. 1. Pressure distribution in a shock wave (air, shock wave velocity 625 m/s, pressure 33 torr): a — in a glow discharge plasma (voltage on electrodes 650 V, discharge current 1.0 A); b — in air without a discharge under the same conditions.

 1063-7850/97/040259-02$10.00  

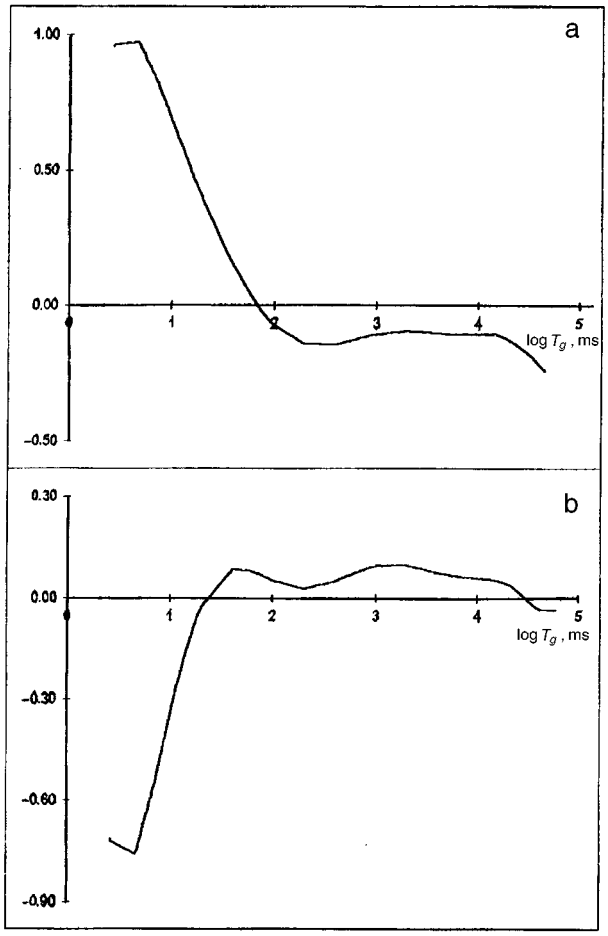


FIG. 2. Amplitude of the first (a) and second (b) harmonics of a Fourier-series expansion of the pressure distribution in a shock wave as a function of the discharge decay time.

vert from the distribution in Fig. 1a to that in Fig. 1b is approximately 100 s. This long time suggests that pure electrodynamic hypotheses cannot explain the effect, because the estimated time taken for the concentration of the charged components to decrease by two orders of magnitude is only 2 ms (Ref. 8). In addition, long-lived excited states of atoms and molecules still exist after some tens of seconds, a fairly high concentration of these being sustained by secondary formation processes in the gas.[8] The radiative time of some metastable states of oxygen is known to be measured in hours.[9]

The second characteristic time which could be accurately identified was 10 ms. After this decay time, the second harmonic of the Fourier series expansion changes abruptly and the amplitude of the harmonic is reduced by an order of magnitude (Fig. 2b). It should be noted that when the pressure in the plasma ahead of the shock wave is 33 torr, this time is the same as the characteristic deactivation time for most excited states in a decaying discharge.[8] This abrupt decrease in the amplitude of the second harmonic while the first remains the same, means that the depth of the pressure dip after the first pressure hump falls by an order of magnitude in the pressure distribution profile of the wave and the distribution is converted from a double-hump to a virtually single-hump profile.

In addition, there are various other time intervals over which the harmonic amplitude decreases, but not so abruptly as that at 10 ms. It may be postulated that these intervals correspond to secondary processes of excited component formation, after which the concentration of these excited components falls sharply and the effect disappears. On the basis of these investigations, we will be able to identify the specific mechanism responsible for the effect at a later date.

In conclusion, the authors would like to express their gratitude to the Russian Fund for Fundamental Research for supporting this research under Grant No. 96-01-00533.

[1] I. V. Basargin and G. I. Mishin, Pis'ma Zh. Tekh. Fiz. **11**, 209 (1985) [Sov. Tech. Phys. Lett. **11**, 85 (1985)].
[2] V. A. Gorshkov, A. I. Klimov, G. I. Mishin, A. B. Fedotov, and I. P. Yavor, Zh. Tekh. Fiz. **57**, 1893 (1987) [Sov. Phys. Tech. Phys. **32**, 1138 (1987)].
[3] I. V. Basargin and G. I. Mishin, Pis'ma Zh. Tekh. Fiz. **15**(8), 55 (1989) [Sov. Tech. Phys. Lett. **15**, 311 (1989)].
[4] G. I. Mishin, Pis'ma Zh. Tekh. Fiz. **11**, 274 (1985) [Sov. Tech. Phys. Lett. **11**, 112 (1985)].
[5] A. S. Baryshniko, ''Intense plasma energy release behind a shock wave and flow patterns,'' in: *Rarefied gas dynamics*, edited by A. E. Beylich, Proc. 17th Intern. Symposium on Rarefied Gas Dynamics (VCH, Weinheim, 1991), pp. 263–270.
[6] I. V. Basargin and G. I. Mishin, Zh. Tekh. Fiz. **66**(7), 198 (1996) [Tech. Phys. **41**, 742 (1996)].
[7] C. Lanczos, *Applied Analysis* (Prentice Hall, Englewood Cliffs, N.J., 1957) [Russ. transl. Fizmatgiz, Moscow, 1961].,
[8] Yu. P. Raĭzer, *Physics of Gas Discharges* [in Russian], Nauka, Mosow (1992).
[9] A. A. Radtsig and B. M. Smirnov, *Reference Data on Atoms, Molecules, and Ions* (Springer-Verlag, Berlin, 1985) [Russ. original, Atomizdat, Moscow, 1980].

Translated by R. M. Durham

# Qualitative boundary, abnormality, and structural transition

G. E. Skvortsov

*St. Petersburg State University*
(Submitted December 8, 1996)
Pis'ma Zh. Tekh. Fiz. **23**, 23–27 (April 12, 1997)

A qualitative boundary law and an abnormality relationship are formulated and their genetic link with the phenomenon of structural transition is demonstrated. This phenomenon includes phase transitions, dissociation and ionization, turbulence, and explosion. The formulated relationships are used to indicate classes of possible nonequilibrium effects. © *1997 American Institute of Physics.* [S1063-7850(97)00504-1]

Highly nonequilibrium processes are becoming increasingly important in physics, chemistry, and biology. Studies of these processes are generating new concepts, and their application is providing the basis of new technologies. These processes are extremely difficult to describe and qualitative analyses are especially valuable, for which fairly comprehensive and constructive relationships are required, such as those formulated in Ref. 1.

In the present paper, as a continuation of Ref. 2, which was concerned with the law of structural conditionality, we examine a quality boundary law and an associated abnormality relationship. The initial formulations of these relationships are extended and investigated in greater depth. Their correlations with the phenomenon of structural transition, and also with the phenomenon and effects of instability are demonstrated. The phenomenon of instability, its properties, and criteria were discussed earlier in great detail.[3]

1. An analysis is made of open systems in which processes are initiated by internal and external influences. The systems are characterized by a layer of structure, which depends on these influences and varies in the course of the process, so that we are dealing with a dynamic system, process.

The fundamental characteristic of the process is the degree of nonequilibrium, which is defined, according to the law of structural conditionality,[2] by the dimensionless product of the action factor $g$ and a corresponding structure factor $s[g]$:

$$|gs|: \quad V=\left|\frac{u}{v_{\mathrm{T}}}\right|, \quad E_i=\left|\frac{e}{\varepsilon_i}\right|, \ldots,$$

$$W_{\mathrm{in}}=\tau_i\left|\partial_t \ln\left|\frac{a_n}{a_{ns}}\right|\right|, \ldots, \tag{1}$$

where $u$ is the velocity of the medium, $v_T$ is the rms velocity of a structure-kinetic element, and $\varepsilon_i$ is its coupling and interaction energy ... (the complete set of these expressions and the corresponding notation are given in Ref. 2). In addition to the degree of equilibrium, the measure of action and the measure of change in structure should be used

$$G=|gs_0|, \quad S=|s[g]/s_0|, \quad s_0=s[0]. \tag{2}$$

According to their nature, the influences are subdivided into active and scale: active influences (1.1), (1.2) determine the gain and loss of mass, momentum, and energy while the scale influences (1.3) express the ratios of the space-time scales of these influences to the corresponding structural characteristics.

2. The qualitative boundary law can be formulated in general terms as follows: when an influence increases (or decreases) to a certain specific level, the system undergoes a qualitative change. An influence causing a qualitative change is active and its corresponding value is described as the qualitative boundary.

In an analytic description of a system (by means of equations of state, determining relations, responses), a qualitative change is observed as specific features in the main behavior: jumps in quantities and their derivatives, bifurcation points, and inversion intervals. These features reflect the abnormality.

An abnormality in the form of an inversion is characteristic of most highly nonequilibrium effects, such as the decay of a thermal flux with increasing temperature difference for a boiling crisis,[4] the decrease in current with increasing voltage (as in the Gunn effect), and anomalous relaxation in shock waves with a whole range of inversions.[5]

These effects and similar ones in terms of abnormality are directly related to the phenomenon of structural transition and ensuing instability.[6,7]

3. The qualitative boundary is usually achieved by a transition from one structure to another. This includes the phenomenon of structural transition, which is a generalization of various effects such as phase transitions, disintegration (dissociation and ionization), turbulence, nuclear fission, fast chemical reactions, cell multiplication, and so forth.

The natural qualitative criteria for a structural transition in accordance with the condition of transition normalization[2] for active processes have the form

$$gs\simeq 1: \quad u\simeq v_{\mathrm{T}}, \quad e\simeq\varepsilon_i, \ldots \tag{3}$$

The first condition implies a transition from subsonic to supersonic, and the second condition covers almost all the transition effects noted above.

In connection with the phenomenon of structural transition, the abnormality relationship may be formulated as follows: a structural transition is accompanied by anomalous behavior of the determining quantities. The reverse statement usually also holds: anomalous behavior of the determining quantities is caused by a structural transition. These state-

ments are extremely valuable for heuristic and experimental purposes (see Ref. 7).

4. The criterion for negative differential susceptibility is a manifestation of abnormality.

The basic relations for moderate nonequilibrium may be expressed in the quasilinear form $\Phi(gs)=K(gs)gs$, where $K$ is the susceptibility. The criterion has the form

$$K_d \equiv \frac{\partial \Phi}{\partial gs} = \frac{\partial K}{\partial gs} gs + K < 0. \quad (4)$$

It was shown in Ref. 3 that for a single determining quantity, this condition implies instability (the principle of abnormality was used for the first time in Ref. 3 to indicate the region of stability). In general, the susceptibility criterion is the only necessary condition for stability.

Logically, if the differential susceptibility is negative for small degrees of nonequilibrium, the sign in criterion (4) should be reversed. In particular, positive compressibility can explain the propagation of a stress-relief shock wave predicted by Ya. B. Zel'dovich. In this context, mention should also be made of the instability of a compressive shock wave under conditions of positive compressibility along the Hugoniot adiabatic curve, indicated in Ref. 6.

5. Among the wide range of applications of these relationships, we select the high-velocity impact of two small bodies. This effect may be expressed in terms of the ratio $\overline{e}_T = e_T/e$ of the kinetic energy $e_T$ after impact to the impact energy $e$, as a function of the degree of nonequilibrium $E_i = e/\varepsilon_i$, where $\varepsilon_i$ is the structural transition threshold closest to $e$.

For the case of head-on impact $e=(m_1 m_2/(m_1+m_2)) \times (v_1^2+v_2^2+2v_1v_2)$, for bodies of equal mass and velocity, criterion (3.2) becomes

$$2mv_c^2 = \varepsilon_i. \quad (5)$$

We first apply this criterion to the collision between xenon atoms in a shock wave to determine the lower (in terms of velocity) abnormal relaxation mode. Assuming $\varepsilon_1 = 0.5\varepsilon[\mathrm{Xe}^m] = 4.15$ eV (Ref. 8), we obtain the threshold velocity $v_c = 1.2$ km/s, which is the same as the value for the observed abnormal regime.[9]

We apply criterion (5) to the impact between two cubic bodies of $\sim 1$ mm edge. We assume that $\varepsilon_i$ are the energies of the structural transitions: $\varepsilon_1$ — melting, $\varepsilon_2$ — evaporation, $\varepsilon_3$ — dissociation, and so on.

The qualitative boundary law will be observed near velocities determined according to criterion (5) as a threshold change in the results of the impact such as a decrease in the particle cloud, an abrupt shift of the luminescence spectrum toward shorter wavelengths, a change in the duration of the postcollision process, fluctuations of $\overline{e}_T$, and so on. The instability is mainly observed as a spread in the threshold values of $v_c$, inhomogeneities of the explosion pattern, and fluctuations of the radiation intensity.

The author is not aware of any experiments in which such observations have been made. However, some results are available on the piercing of plates $\sim 1$ mm thick by a similar-diameter projectile,[10] which demonstrate various abnormalities: for example, the breakdown ''flare'' decreases with increasing velocity and also the piercing by the flare decreases to zero (Ref. 10, pp. 125–154). It should be assumed that the step dependence of the relative crater depth on the velocity for a thick target (see pp. 323–331) is related to criterion (5).

To conclude, we note that the initial application of these relationships, including the law of structural conditionality,[2] to natural evolving systems[11] yields broadly consistent results. However, in Ref. 11, no mention is made of the inversion abnormality of the structural transition. A closer comparison of the results will undoubtedly yield a whole range of interesting conclusions.


[1] G. E. Skvortsov, Pis'ma Zh. Tekh. Fiz. **16**(17), 15 (1990) [Tech. Phys. Lett. **16**, 1647 (1990)].
[2] G. E. Skvortsov, Pis'ma Zh. Tekh. Fiz. **23**(6), 85 (1997) [Tech Phys. Lett. **23**, 246 (1997)].
[3] E. N. Perevoznikov and G. E. Skvortsov, Zh. Tekh. Fiz. **52**, 2353 (1982) [Sov. Phys. Tech. Phys. **27**, 145 (1982)].
[4] S. S. Kutateladze, *Analysis of Similarity and Physical Models* [in Russian], Nauka, Leningrad (1986).
[5] G. I. Mishin, A. P. Bedin, N. I. Yushchenkova, G. E. Skvortsov, and A. P. Ryazin, Zh. Tekh. Fiz. **51**, 2315 (1981) [Sov. Phys. Tech. Phys. **26**, 1363 (1981)].
[6] A. S. Baryshnikov and G. E. Skvortsov, Zh. Tekh. Fiz. **49**, 2483 (1979) [Sov. Phys. Tech. Phys. **24**, 1401 (1979)].
[7] G. E. Skvortsov and N. Yu. Vasil'ev, Zh. Tekh. Fiz. **55**, 230 (1985) [Sov. Phys. Tech. Phys. **30**, 137 (1985)].
[8] A. A. Radtsig and B. M. Smirnov, *Reference Data on Atoms, Molecules, and Ions* (Springer-Verlag, Berlin, 1985) [Russ. original, Atomizdat, Moscow, 1980].
[9] G. K. Tumakaev, Z. A. Stepanova, and P. V. Grigor'ev, Zh. Tekh. Fiz. **61**(9), 149 (1991) [Sov. Phys. Tech. Phys. **36**, 1051 (1991)].
[10] Int. J. Impact. Eng. **5** (1987).
[11] A. V. Zhirmunskiı and V. I. Kuz'min *Criticality Levels in the Evolution of Natural Systems* [in Russian], Nauka, Leningrad (1990).


Translated by R. M. Durham

# Magnetic sensitivity of protein

E. G. Rapis

*Ichilov Hospital, Sourasky Medical Center, Sackler Faculty of Medicine, Tel-Aviv University, 63249 Tel Aviv, Israel*

(Submitted September 23, 1996)
Pis'ma Zh. Tekh. Fiz. **23**, 28–38 (April 12, 1997)

It is shown for the first time that protein acquires magnetic sensitivity when it condenses. A visual optical method is used to observe the dynamics of the formation of the magnetic properties. The magnetic sensitivity is established by a modified method of decoration with ferromagnetic iron. © *1997 American Institute of Physics.* [S1063-7850(97)00604-6]

1. The present paper reports results of experimental studies which have demonstrated for the first time the magnetic sensitivity of protein. A direct method of assessing the existence of magnetic properties during the condensation of protein was used to determine the magnetic sensitivity, by decorating the protein with ferromagnetic iron and simultaneously monitoring nonmagnetic metallic materials such as copper, aluminum, and so on.

The apparatus proposed by the author earlier was used,in which the condensation of protein is observed optically in an aqueous system as it undergoes evaporation *in vitro* at room temperature.[1–5]

By studying the dynamics of the condensation of pure protein at the macroscopic level in an open system far from thermodynamic equilibrium, using an optical polarizing microscope (monitoring the observations with a video apparatus), more detailed information was obtained regarding previous experimental investigations.[4,5] In addition to the previously described spiral, anisotropic, dichromic, coherent, and synchronous autowave oscillations, more than three cycles of diffusion activity processes were found, corresponding to several different time scales.

2. In the initial phase, the process developed rapidly and its various manifestations could be observed for a few seconds, minutes, hours, and for the first few days. Over these times, zones of merging, shallow centers appeared in a liquid droplet of the solution, accompanied by the formation of light fields, which then acquired clearly defined boundaries. These effects were observed against a background of previous and remaining traces of global autowaves. The fields became semitransparent hemispheres, which gradually underwent diffusion spreading (Fig. 1), moving counter to an opposite field.

The first penetrating dislocation cracks suddenly appeared through the center of a still liquid homogeneous mass of protein, dividing it dichotomously into two parts (right/left division in Figs. 2a and 2b, top/bottom division in Figs. 2c and 2d), according to the opposite motion of the fields.

The thin film of protein (liquid crystal phase) exhibited an ''optical pulsation'' consisting of a sudden consistent color change in the zone of a single domain. Two-colored autowaves generated so-called fingerprints on either side of defects.

Then, curved moving lines, forming the turns of a spiral, appeared in the denser, viscous mass of protein. These lines were connected to a single rounded zone of considerable size (or nucleus, Figs. 3b and 3c) in each block or domain. Dividing rectilinear defects appeared along the domain boundaries (Fig. 3a). The motion of the lines was either slow and gradual or abrupt (avalanche-like). These discretely packed lines of spiral turns spawned three-dimensional funnel-shaped vortex structures. The number of turns increased as they changed from liquid to dense vortex funnels. We stress that a pair of vortices always had the opposite direction of rotation with a rectilinear defect in between (Fig. 3a).

In the sample we frequently observed a phenomenon whereby the field (or center) of the ''mother'' spiral split into two oval blocks, linked by a single dividing line, similar to the division of an egg or cell of a living organism (Figs. 3a and 3b). The division was initiated at the center of the field width from a single curving line. Each oval could then be divided again into two, then four in a geometric progression.

3. After a few weeks, the process of change in the protein structure typically continued in the later phases. For example, after a few days, weeks, and months, new structural forms, given the name filaments, appeared in the optical surface zone of dense protein mass. These filaments were bounded by lines which appeared dashed with alternating darker and lighter zones (Fig. 4).

Quite frequently, two or four ''daughter'' spirals rotating

FIG. 1. Formation of transparent hemispheres with defined outer edges (a).


FIG. 2. The first dislocations (cracks) divide the still liquid homogeneous protein mass dichotomously through the central zone (right/left division — a, b) into two parts, upper and lower (c, d), according to the distribution of the counterpropagating fields.

in the opposite direction, were formed inside a mother spiral at the point where the ovals divided (Fig. 3) and these resembled the familiar spiral-in-spiral structures.

4. On reviewing the morphological and functional manifestations of the specific ordering of the protein as it condensed, we noted that, strange as it may seem, many of the properties are the same as those in media (far removed from biology) with strong magnetic fields. For example, on comparing the data obtained and described above on the behavior of the curved lines and vortices in condensing protein with the familiar lines and vortices in type II superconductors,[11–16] the following common properties were observed: a) the motion of the lines is gradual (diffusive) or avalanche-like,[11,12] and discretely packed lines form vortex spiral structures, initially liquid and then dense;[10–16] b) it was established that the appearance of the lines depends on changes in temperature;[11,12] c) curved defects are formed in the line zone;[11] d) the spiral turns (lines) of each vortex in one domain are linked to a common center (nucleus);[11] e) rectilinear fractures (defects) are formed at the boundary of each domain; f) pairs of three-dimensional funnel-shaped vortices are observed with a defect between them;[10–16] g) these structures are highly anisotropic;[12–16] h) a cycle of new lines and division in the active regions begins with bending of these lines at the center of the magnetic field width,[7,8] which is attributed to the law of opposite polarization.

It is also worth noting that, according to new data, the spiral vortex structures of DNA resembles the vortices of type II superconductors.[13,17]

5. A modified version[10] of the familiar method of decorating with iron was used to identify the magnetic sensitivity of protein during its condensation process.

The method was as follows: iron filings were placed on the surface of a viscous solution of protein (lysozyme) in a Petri dish. Exactly the same experiments were used as a control, except that copper and aluminum filings were placed on the surface of the lysozyme. All the experiments were carried out under the same macroconditions using the technique described above. The differences were that the protein hardened in the presence of the filings.

The experiments revealed that when iron, possessing magnetic properties, was added to the protein, unlike the copper and aluminum additives, which are nonmagnetic metals, the structure of the vortices and filaments changed qualitatively as the protein condensed. For example, the number of spiral turns in the vortices fell sharply (Fig. 5a), and the

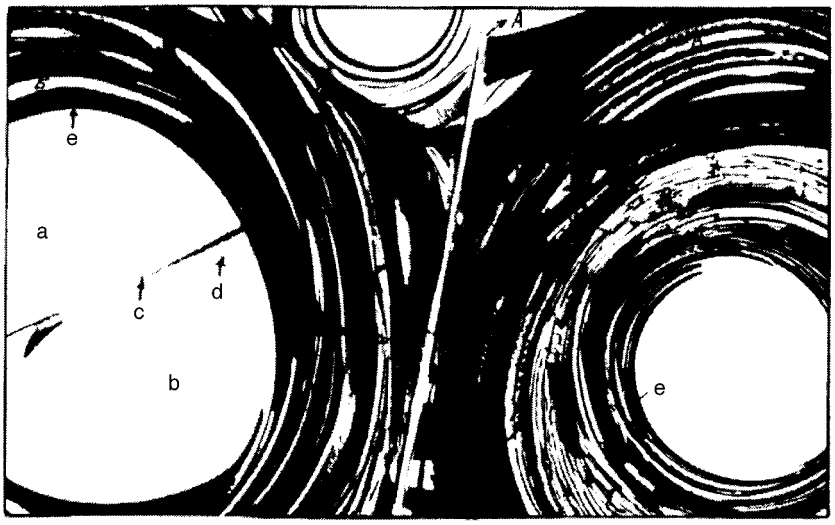


FIG. 3. Formation of a pair of opposite-rotating vortices (B, C) with an interspersed defect (A). The primary mother spiral (B) begins to split into two oval elliptical blocks (a, b) from curved lines at the center of the field width (c), similar to the division of a living egg or cell (downward division of a living snake egg — Pateria minaita). Optical phase (to 185) (By courtesy of Dr. Richard Boolootian BSCS, Boulder, Colorado). Thin optical lines at an angle of 45° to the vertical axis were formed on the inside of the pair of vortices (d) and zones of attraction consisting of solid black rings (or lines) appeared in the vortices, where rotating funnels (and thin lines) merged (e).

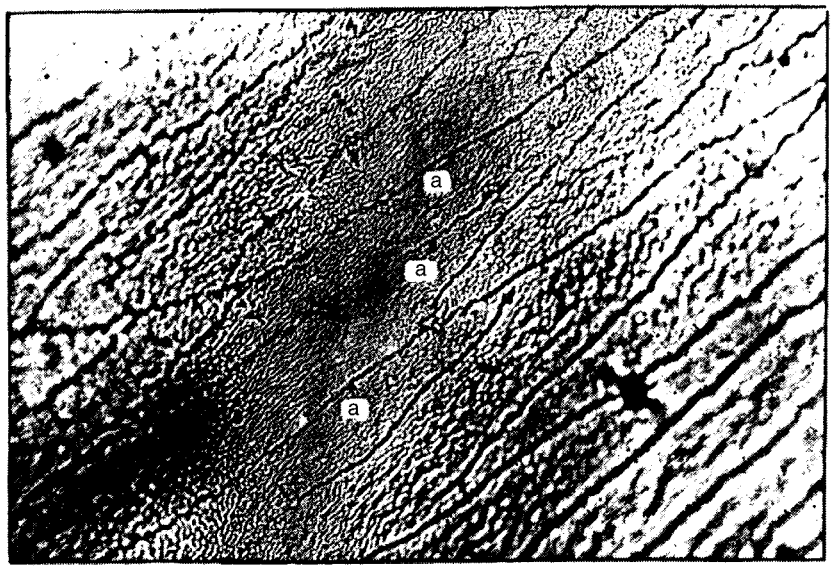


FIG. 4. Fields of equalized filaments with lines having contrasting dark and light zones, resembling dashed lines (a).

nucleus of the vortex became enlarged and changed shape (Fig. 5b). The filaments and their bounding lines became disordered, they diverged from a piece of iron like a ''Medusa's head'' (Fig. 6), acquiring a coarse dashed (broken) appearance (Fig. 6a). New structures were also observed in the form of thin semitransparent fibrous filaments (Fig. 7a), encircling particles of iron (Fig. 7b).

However, the most important result of this experiment was that sudden changes in the vortices and filaments, and structures not observed by us previously in protein, were only observed when the protein condensed in the presence of the ferromagnetic iron filings and not the nonmagnetic metals. It may be postulated that this pattern reflects the interaction between the magnetic fields of the protein and the iron.

6. Another factor, no less unexpected, was that many of the effects observed during the condensation of protein are similar and analogous to the known turbulent and chaotic behavior of various systems.

This observation particularly applies to the autowave oscillations described previously in the liquid phase,[1–4] which are now classified as turbulent and chaotic effects.[12,21,22]

In the denser phase, domain copies appear synchronously, in which more ordered zones in the form of straight lines (defects) alternate with less ordered sections of clearly increasing branching, in the form of spiral anisotropic lines and vortices, within each domain. Discretely and regularly packed turns and circles are replaced by irregularly distributed sections, where thin lines and turns clearly merge into solid black rings and bands, in other words, zones of attraction (Figs. 3 and 4), similar to those described in oscillating synchronous chaos.[20]

Dual behavioral features are also identified in the temporal dynamics: gradual motion of the lines clearly alternates with a sudden avalanche-like appearance of copies.

These spatial and temporal characteristics and features of the process are characteristic of systems exhibiting chaotic behavior.[18–23]

The appearance of the structural forms described (such as helical vortices, and so on) does not depend on the size and scale of the domain, being repeated at the microscopic


FIG. 5. Change in the structure of the vortices when iron filings are added to the protein: the number of turns and their decoration with iron decreases (a) while the nucleus becomes larger and changes shape (b).

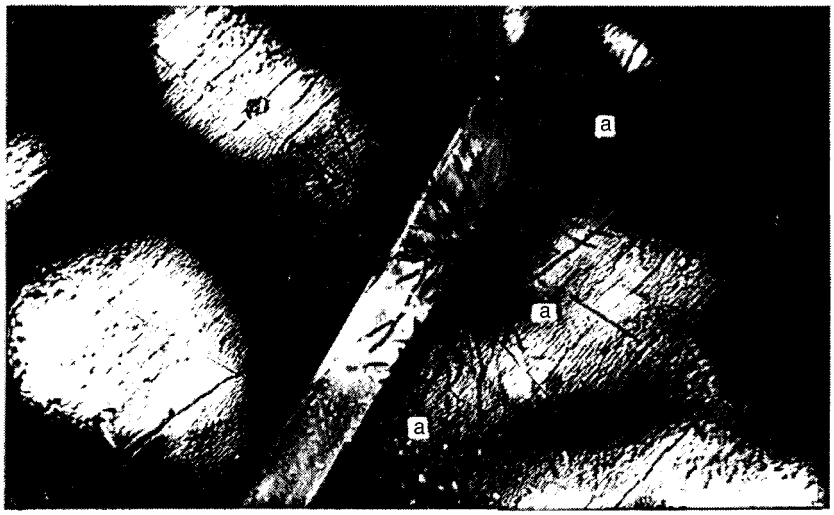


FIG. 6. Damage to the structure of the filaments and their bounding lines. They become disordered, encircling pieces of iron like a ''Medusa's head'' and acquiring a coarse dashed pattern (a).

and macroscopic levels (i.e., when observed under the microscope and with the naked eye) and is repeated on any level, which is consistent with the generally accepted data on the helical structure of protein at the molecular level.

When discussing these structural characteristics of protein and attempting to understand their role, it should be borne in mind that the formation of helical vortices in any material, or the creation of strongly rotating fields, is a source of turbulence at any structural level,[8,9] and is also an analog of magnetic fields and a key factor in their generation.[21]

7. On this basis, it may be hypothesized that in energy terms, the transition of a protein from the liquid to the solid state may be associated not only with turbulent (chaotic) hydrodynamics, generating pairs of vortex structures, but also with the magnetic properties of the protein, comprising MHD turbulent instability and dynamics.

However, in order to refine this hypothesis, we also need to determine the direction of transport of the angular momentum, since it is known that MHD turbulent instability and dynamics caused by MHD turbulent instability, is accompanied by internal transport of the angular momentum, which is not the case in simple turbulent hydrodynamics.[8,9]

In this respect, the following observation was made: when a mass of protein begins to condense, the appearance of a rectilinear defect, separating pairs of domains, is immediately followed by the formation of thin discrete lines in each domain. These lines move in opposite directions, extending from the outside inward on either side of a defect, near its upper boundary and are therefore distributed inside each of the two pair domains and two vortices. These dashes (lines) are most frequently positioned at an angle of 45° to the defect. Twisting lines (Figs. 3d and 4), spiral turns, and an internal elbow begin to be formed from these lines. A thick black angular line, or attraction zone, often at an angle of 60° and sometimes more, frequently appears suddenly in this zone at the site of the discrete lines or replaces them.

Thus, a pair of contrarotating vortices is formed with an interspersed fracture and two differently directed angular zones on the inside of each vortex. This structure was a basic one in the solid phase of protein.

It is possible that the internal distribution of the optically

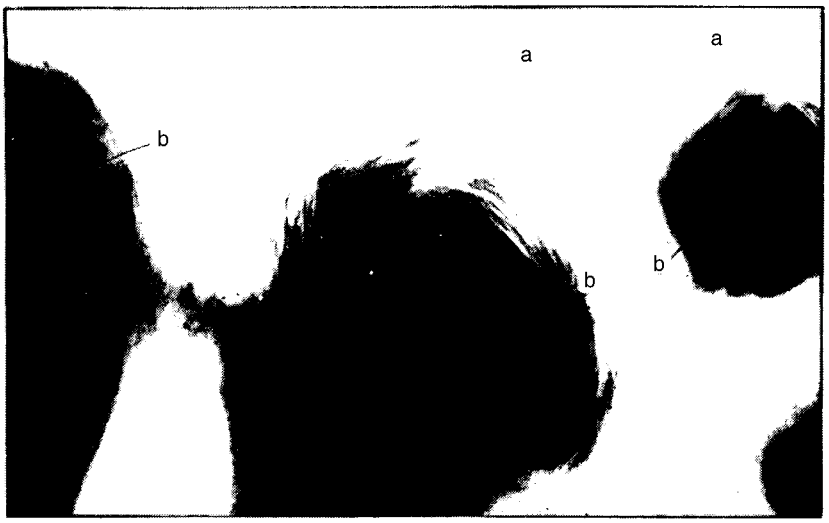


FIG. 7. Formation of new structures in the form of thin white semitransparent fibrous filaments (a) encircling pieces of iron (b).

observable lines reflects the unknown direction of transport of the angular momentum, and may serve as an additional argument in support of the hypothesis.

However, even more important confirmation is provided by the observation that condensing protein is magnetically sensitive (see experimental data).

8. Thus it has been established that a magnetized material (iron filings) influences the self-organization process of protein, altering the nature of its flow, which is observed as a decrease in the spiral turns and vortices, an increase and change in the domain nuclei, and the appearance of new structures. This is the key issue in the present study.

These data, combined with various others presented above, indicate that protein possess as yet unknown properties and that there may be a link between the turbulent (chaotic) and magnetic properties, which are observed during condensation. On this basis, we put forward the hypothesis of MHD turbulent instability and dynamics during the protein phase transition.

We assume that this hypothesis requires quantitative verification and a more comprehensive in-depth study. These as yet merely qualitative observations most likely reflect some aspects of the complex phenomenon of protein condensation.

However, it may be considered that the proposed method of visualizing the cooperative phenomenon of magnetic and turbulent (chaotic) properties in the transition phase of protein opens up promising new approaches to the detailed study of the self-organization mechanism with allowance for these factors.

To conclude, I should like to thank Professors D. Amir, M. Amus', A. Arel', M. Klinger, Yu. Neéman, and I. Prigozhin for their moral support in these studies, for discussions of the results and proposed hypotheses, and for valuable comments.

[1] E. G. Rapis, Pis'ma Zh. Tekh. Fiz. **14**, 1560 (1988) [Sov. Tech. Phys. Lett. **14**, 679 (1988)].
[2] E. G. Rapis and G. Yu. Gasanova, Zh. Tekh. Fiz. **61**, 462 (1991) [Sov. Phys. Tech. Phys. **36**, 406 (1991)].
[3] E. G. Rapis, A. S. Botin, and A. N. Zaikin, *Abstracts of Papers Presented at the International Conference on the 100th Anniversary of F-Groups* [in Russian], Leningrad, 1991.
[4] E. G. Rapis, Pis'ma Zh. Tekh. Fiz. **21**(9), 13 (1995) [Tech. Phys. Lett. **21**, 321 (1995)].
[5] E. G. Rapis, Tech. Phys. Lett. **21** (1995).
[6] E. G. Rapis, Symmetry, Culture Science **6**, 439 (1995).
[7] A. Boebinger *et al.*, Physica B **201**, 500 (1994).
[8] N. Brummell *et al.*, Science **269**, 1970 (1995).
[9] J. F. Hawley, Science **269**, 1365 (1995); R. F. Service, Science **271**, 1804 (1996).
[10] D. Bishop *et al.*, Science **255** (1995).
[11] T. Matsuda *et al.*, Science **271**, 1393 (1996).
[12] F. Nori, Science **271**, 1373 (1996).
[13] D. K. Nelson, Nature (London) **375**, 356 (1995).
[14] E. Zeldov *et al.*, Nature (London) **375**, 373 (1995).
[15] P. B. Allen, Nature (London), **375**, 729 (1995).
[16] U. Welp *et al.*, Nature (London) **376**, 729 (1995).
[17] R. Podgornik and V. A. Parsegian, Macromolecules **23**, 2200 (1990).
[18] H. H. Stølum, Science **271**, 1710 (1996).
[19] M. Dennin, Science **272**, 388 (1996); [19a] E. J. Heller, Nature (London) **380**, 583 (1996).
[20] J. F. Heagy *et al.*, Phys. Rev. Lett. **73**, 3528 2(1994).
[21] R. E. Ecke *et al.*, Science **269**, 1704 (1995).
[22] A. Karma, Nature (London), **379**, 118 (1996).
[23] Q. Ouyang *et al.*, Nature (London) **379**, 143 (1996).

Translated by R. M. Durham

# Critical importance of the single-level approximation to account for the highly nonmonotonic dependences of carrier lifetimes on recombination impurity concentration

V. A. Kholodnov and P. S. Serebrennikov

*Theory Department, State Science Center of the Russian Federation, Orion State Scientific-Industrial Organization, Moscow*

(Submitted December 4, 1996)
Pis'ma Zh. Tekh. Fiz. **23**, 39–45 (April 12, 1997)

This paper is a continuation of an analysis regarding an increase in the lifetimes of nonequilibrium electrons $\tau_n$ and holes $\tau_p$ by several orders of magnitude, observed with increasing concentration of recombination centers. It is shown that a substantial increase in $\tau_n$ and $\tau_p$ may also occur for three charge states of the recombination impurities $N$, and the curves $\tau_n=f(N)$ and $\tau_p=f(N)$ may each have two minima and maxima. © *1997 American Institute of Physics.* [S1063-7850(97)00704-0]

It has been reported[1–4] that in semiconductors with impurity recombination of nonequilibrium carriers,[5–9] the dependences of the electron and hole lifetimes, $\tau_n$ and $\tau_p$, on the recombination impurity concentration $N$, which generally decrease with increasing $N$, may have a section where the lifetimes increase by several orders of magnitude because of the nonequilibrium filling of the recombination level. A model of two possible charge states (to be specific, neutral and negative singly-charged states with the concentrations $N_0$ and $N_-$) of the recombination impurities (single-level approximation) was used in Refs. 1–4. However, this effect is observed when $\delta_1=N_-^e/N_0^e\gg 1$ (Refs. 2 and 4), where $N_-^e$ and $N_0^e$ are the corresponding equilibrium concentrations. This implies that capture of electrons by negative singly-charged centers may play a significant role, which was neglected in Refs. 1–4. Given the feasibility of obtaining long lifetimes for large $N$, as demonstrated in Refs. 1–4, our aim in the present paper is to study how critical the single-level approximation is to the existence of this effect. A slight deviation from the equilibrium state is analyzed, as in Refs. 1–4. This may be achieved by recording weak optical radiation by semiconductors.

Let us assume that nonequilibrium electrons and holes, having the concentrations $\Delta n=n-n_e$ and $\Delta p=p-p_e$, are only formed by interband excitation or by injection from contacts, where $n$ and $p$ are the electron and hole concentrations, and $n_e$ and $p_e$ are their equilibrium values. As in Refs. 1–4, we assume that there are shallow, completely ionized donors with the concentration $N_D$ and that the recombination impurities are acceptors, which, unlike the model used in Refs. 1–4, are in a negative doubly-charged state,[5–9] with the concentration

$$N_{-2}=N-N_0-N_- \tag{1}$$

with the equilibrium value $N_{-2}^e=\delta_2 N_0^e$ (two-level approximation). Neutral atoms capture electrons with probability $w_{01}$ and thermally generate holes; singly charged centers capture both electrons and holes with probabilities $w_{21}$ and $w_{10}$, respectively, and also thermally generate both types of carriers; doubly charged centers capture holes with probability $w_{21}$ and thermally generate holes. Thus, the rate of recombination of the electrons is

$$R_n=w_{01}nN_0+w_{12}nN_- -w_{01}\delta_1^{-1}n_eN_- -w_{12}\delta_1\delta_2^{-1}n_eN_{-2}, \tag{2}$$

and that of the holes is

$$R_p=w_{10}pN_- +w_{21}pN_{-2}-w_{10}\delta_1 p_eN_0 -w_{21}\delta_1^{-1}\delta_2 p_eN_- . \tag{3}$$

In the steady-state case, the charge state of the recombination impurity atoms is determined by

$$R_n=R_p, \tag{4}$$

$$\frac{\partial N_0}{\partial t}=-w_{01}nN_0+w_{01}\delta_1^{-1}n_eN_- +w_{10}pN_- -w_{10}\delta_1 p_eN_0=0. \tag{5}$$

The equation of neutrality for a nondegenerate semiconductor in thermodynamic equilibrium[6–8] may be expressed in the form

$$N=\frac{n_{t1}}{2}[1+\delta_1+\delta_2(\delta_1)]Y(\delta_1),$$

$$Y(\delta_1)=\frac{(B_1+A_1\delta_1-\delta_1^2)}{\delta_1\cdot[\delta_1+2\delta_2(\delta_1)]}, \tag{6}$$

where

$$\delta_2(\delta_1)=\delta_1^2\frac{n_{t1}}{n_{t2}},\quad A_j=2\frac{N_D}{n_{tj}},\quad B_j=4\frac{p_{tj}}{n_{tj}}, \tag{7}$$

$n_{tj}$ and $p_{tj}$ are the equilibrium carrier concentrations when the Fermi level coincides with the recombination level ($j=1$ corresponds to the lower level and $j=2$ corresponds to the upper level). To derive expressions (6) and (7), we assumed, as in Refs. 2 and 4, that the degeneracy factors of the acceptor levels are $g_1=g_2=1/2$ (Refs. 6–8).

If the carrier concentrations and the concentrations of their trapping centers have small deviations from their equilibrium values, $\Delta N_0=N_0-N_0^e$, $\Delta N_-=N_--N_-^e$, and $\Delta N_{-2}=N_{-2}-N_{-2}^e$, respectively, Eqs. (1)–(5) can be linearized with respect to these deviations. Then, using the Poisson equation

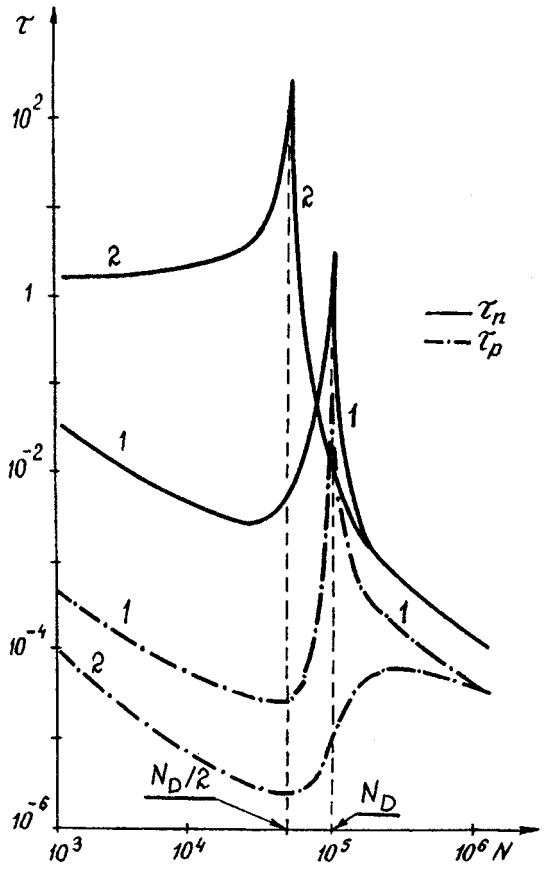


FIG. 1. Lifetimes of electrons $\tau_n$ and holes $\tau_p$ versus concentration $N$ of two-level recombination impurities for large and small differences between the energies of the upper and lower recombination levels $\mathscr{E}_{t2}$ and $\mathscr{E}_{t1}$: *1* — $\mathscr{E}_{t2}-\mathscr{E}_{t1}=23kT$, *2* — $\mathscr{E}_{t2}-\mathscr{E}_{t1}=5kT$, where $k$ is Boltzmann's constant, and $T$ is the temperature. It is assumed that: $n_{t1}=10^{-4}n_i$, $N_D=10^5 n_i$, $w_{10}/w_{01}=10^2$, $w_{10}/w_{12}=10^3$, and $w_{10}/w_{21}=10^{-1}$. The times are measured in units of $1/(n_i w_{10})$ and $N$ is measured in units of $n_i$.

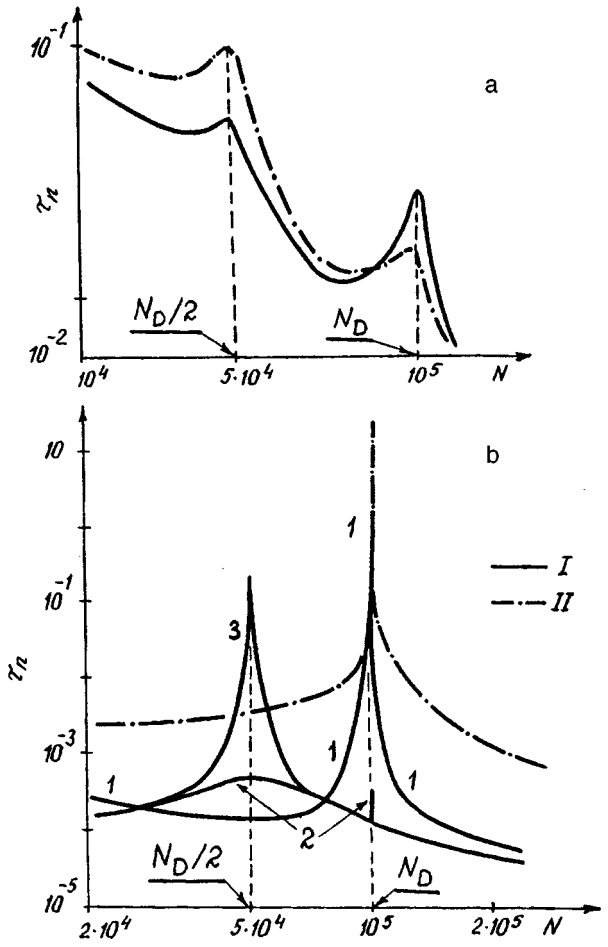


FIG. 2. Electron lifetimes $\tau_n$ versus recombination impurity concentration $N$: a — for a two-level system with average spacing $\mathscr{E}_{t2}-\mathscr{E}_{t1}=17\,kT$ (*I*) and $\mathscr{E}_{t2}-\mathscr{E}_{t1}=16\,kT$ (*II*) between the upper and lower levels; b — for the single-level systems $N_0$, $N_-$ (*II*) and $N_-$, $N_{-2}$ (*I*): *1* — $\mathscr{E}_{t2}-\mathscr{E}_{t1}=25kT$, *2* — $\mathscr{E}_{t2}-\mathscr{E}_{t1}=17.5kT$, and *3* — $\mathscr{E}_{t2}-\mathscr{E}_{t1}=5kT$. It is assumed that: $n_{t1}=10^{-4}n_i$, $N_D=10^5 n_i$, $w_{10}/w_{01}=10^2$, $w_{10}/w_{12}=10^3$, and $w_{10}/w_{21}=10^{-1}$. The times are measured in units of $1/(n_i w_{10})$ and $N$ is measured in units of $n_i$.

$$\mathrm{div}(\Delta E)=\frac{4\pi q}{\varepsilon}\cdot(\Delta p-\Delta n-\Delta N_- -2\Delta N_{-2}), \tag{8}$$

as in Ref. 4, we obtain

$$R_n=\frac{\Delta n}{\tau_n}+a_n\mathrm{div}(\Delta E),\quad R_p=\frac{\Delta p}{\tau_p}+a_p\mathrm{div}(\Delta E), \tag{9}$$

where

$$\frac{1}{\tau_n(\delta_1)}=\frac{\delta_1 n_{t1}}{2}\cdot\left[w_{01}x_1+\left(w_{12}-\frac{w_{01}}{\delta_1}\right)x_2 - w_{12}\frac{\delta_1}{\delta_2}x_3+(w_{01}\delta_1^{-1}+w_{12})Y(\delta_1)\right], \tag{10}$$

$$\frac{1}{\tau_p(\delta_1)}=\frac{2p_{t1}}{\delta_1 x_4}\cdot\left[w_{21}x_3+\left(w_{10}-w_{21}\frac{\delta_2}{\delta_1}\right)x_2-w_{10}\delta_1 x_1\right] +(w_{10}\delta_1+w_{21}\delta_2)\frac{n_{t1}}{2}Y(\delta_1), \tag{11}$$

the dependences of $x_1$, $x_2$, $x_3$, and $x_4$ on $\delta_1$ are determined by the system of equations

$$x_1+x_2+x_3=0, \tag{12}$$

$$(w_{01}\delta_1+w_{10}B_1)\cdot\left(\frac{x_2}{\delta_1}-x_1\right)+w_{10}\delta_1 Y(\delta_1)x_4=w_{01}Y(\delta_1), \tag{13}$$

$$x_4-2x_3-x_2=1, \tag{14}$$

$$\left(w_{12}+w_{21}\frac{B_1\delta_1}{\delta_1^3}\right)\cdot\left(\frac{\delta_1}{\delta_2}x_3-x_2\right)+w_{21}\frac{\delta_2}{\delta_1}Y(\delta_1)x_4 =w_{12}Y(\delta_1), \tag{15}$$

$a_n(\delta_1)$ and $a_p(\delta_1)$ are coefficients, and $\Delta E$ is the change in the electric field strength caused by the deviations of $n$, $p$, $N_0$, $N_-$, and $N_{-2}$ from their equilibrium values. We use the same terminology for the lifetimes $\tau_n$ and $\tau_p$, even when quasineutrality is violated.[4] This is justified because in the equation (fourth-order) for the spatial distribution of $\Delta n$ (or $\Delta p$), the coefficient preceding the term in $\Delta n$ (or $\Delta p$) is always $1/\tau_n$ (or $1/\tau_p$) (Ref. 10), as in interband recombination.[11]

By defining the values of $\delta_1$, we can obtain the curves $\tau_n(N)$ and $\tau_p(N)$ using Eqs. (6), (7), and (10)–(15). It can be seen from Fig. 1 that, as in the single-level problem,[1–4] these may have a section where the lifetimes increase by more than two or three orders of magnitude (or even more). Unlike the single-level approximation,[2–4] the maxima of these functions are not generally observed at the point $N=N_D$ and their positions do not coincide for $\tau_n(N)$ and $\tau_p(N)$. Two maxima and two minima may even be observed (Fig. 2a). This behavior is caused by the nonequilibrium filling of the levels[2,4] and by the different curves of $\tau_n(N)$ and $\tau_p(N)$ for single-level $N_0$, $N_-$ (lower level) and $N_-$, $N_{-2}$ (upper level) systems because of the additional charge $(-2qN_{-2})$ in the latter case. For example, a maximum of $\tau_n(N)$ for the $N_0$, $N_-$ system can only occur for $N=N_D$ (Refs. 2 and 4), whereas for the $N_-$, $N_{-2}$ system, maxima can occur for $N=N_D$ and for $N=N_D/2$ (Fig. 2b). When $n_{t2}/n_i$ is fairly large and $n_{t1}\ll n_i$, where $n_i$ is the intrinsic carrier concentration, maxima of $\tau_n(N)$ are obtained for both systems for $N=N_D$ (Fig. 2b). Thus in a two-level system $\tau_n(N)$ has one maximum for $N=N_D$ (Fig. 1). With decreasing $n_{t2}$, two maxima of $\tau_n(N)$ are observed for the $N_-$, $N_{-2}$ system (Fig. 2b), so that in a certain range of values of $n_{t2}/n_{t1}$, two minima and two maxima are formed in a two-level system (Fig. 2a). As $n_{t2}$ decreases further, the curve $\tau_n(N)$ for the $N_-$, $N_{-2}$ system has only one maximum at $N=N_D/2$, and the curve $\tau_n(N)$ for $N=N_D$ for the $N_-$, $N_{-2}$ system is lower than that for the $N_0$, $N_-$ system (Fig. 2b). Thus, there is again one peak but at $N=N_D/2$ (Fig. 1).

A detailed physical interpretation of these results can be made by using the principle of partial components of reciprocal carrier lifetimes.[2,4] However, this requires a large amount of journal space[4] and thus will be reported separately.

The authors are grateful to the Russian Fund for Fundamental Research for supporting this work (Grant No. 96-02-17196).

[1] A. A. Drugova and V. A. Kholodnov, Pis'ma Zh. Tekh. Fiz. **18**(1), 23 (1992) [Sov. Tech. Phys. Lett. **18**, 8 (1992)].
[2] A. A. Drugova and V. A. Kholodnov, Solid State Electron. **38**, 1247 (1995).
[3] A. A. Drugova and V. A. Kholodnov, *Proceedings of the International Symposium on Semiconductor Device Research*, Charlottesville (1995), Vol. 1, pp. 197–200.
[4] V. A. Kholodnov, Fiz. Tekh. Poluprovodn. **30**, 1011 (1996) [Semiconductors **30**, 538 (1996)].
[5] A. G. Milnes, *Deep Impurities in Semiconductors* (Wiley, New York, 1973) [Russ. transl., Mir, Moscow, 1977].
[6] J. S. Blakemore, *Semiconductor Statistics* (Pergamon Press, Oxford, 1962) [Russ. transl. Mir, Moscow, 1964].
[7] P. S. Kireev, *Physics of Semiconductors* [in Russian], Vyssh. Shkola, Moscow (1969).
[8] J. S. Blakemore, *Solid State Physics*, 2nd ed. (Cambridge University Press, Cambridge, 1985) [Russ. transl., Mir, Moscow, 1988].
[9] R. A. Smith, *Semiconductors* (Cambridge University Press, Cambridge, 1959) [Russ. transl. Mir, Moscow, 1982].
[10] F. Stockmann, *Proceedings of the Photoconductivity Conference*, New York, 1956, pp. 269–286.
[11] V. A. Kholodnov, Semicond. Sci. Tech., to be published (1997).

Translated by R. M. Durham

# Numerical simulation of a porous cooling effect observed when a hypersonic stream of viscous gas with a decaying shock wave flows round a wall

S. A. Isaev, A. I. Leont'ev, V. V. Nosatov, and G. S. Sadovnikov

*Academy of Civil Aviation, St. Petersburg; N. É. Bauman State Technical University, Moscow*
(Submitted December 16, 1996)
Pis'ma Zh. Tekh. Fiz. **23**, 46–50 (April 12, 1997)

The concept of porous cooling observed when a hypersonic stream of viscous gas with a decaying shock wave flows round a wall is substantiated by means of a finite-difference solution of the Reynolds equations, closed by using a two-parameter dissipative turbulence model.
 [S1063-7850(97)00804-5]

A numerical analysis of the influence of blowing on the thermophysical characteristics of the hypersonic flow of a viscous gas near a wall with a thermally stressed section in an oblique shock wave incidence test is aimed at substantiating the prospects offered by the concept of porous cooling for the development of new heat protection systems for power installations on modern aircraft. A software package was developed for solving the Navier–Stokes equations for laminar flow using a method of determination, and solving the Reynolds equations, closed by means of a two-parameter model of dissipative turbulence for turbulent flow, and this software was tested for a set of calculations of continuous and stalled supersonic and hypersonic flows of a viscous gas.[1,2] The classical problems of flow in plane-parallel and expanding channels, in a stepped channel with a rear-facing step, and in a hypersonic air intake were also considered. It should be noted that the MacCormack[3] explicit–implicit scheme is used to discretize the convective terms of the equations.

In the present study this software package is used to analyze the laminar flow of a hypersonic stream of viscous gas around a planar wall when a generated oblique shock wave is incident on it, as in Ref. 1, in the calculation zone between the wall and the wedge-shaped surface of the shock generator. To reduce the size of this region, it is assumed that the stream is symmetric about an upper reference plane, it is parallel to the wall, and emerges from the sharp edge of an oblique shock wave generator. Thus, an analysis is made of the evolution of a hypersonic flow of viscous gas in a channel of variable through cross section with a central convergent section. The physicochemical conversions which may take place at these flow velocities, are neglected in this solution of the problem. The initial conditions are defined assuming that the stream is uniform within the calculation zone. Moreover, the gas parameters at all the calculation points are assumed to be equal to those in the unperturbed stream. The stream parameters are kept constant at the entrance to the zone, while ''soft'' boundary conditions or conditions for continuation of the solution, are imposed at the exit. Conditions of attachment are satisfied in the calculation process at the lower wall, and the wall temperature is kept constant. Conditions corresponding to those at a thermally insulated wall are assumed at the upper surface of the shock generator.

When calculations of supersonic flows with shock waves are made using high-order approximation schemes, especially the MacCormack scheme,[3] the solution must be made monotonic because pulsations of a nonphysical, purely computational, nature are usually observed in the ranges of high gradients of the flow-determining parameters. In the present paper, as in Ref. 4, we use a procedure which involves introducing a diffusion constant exclusively at points of nonmonotonicity, i.e., in regions of computational ''ripple.'' Oscillations originating from the scheme are thereby eliminated.

In our investigations, the calculation region was divided by a mesh dense near the walls, especially near the lower wall, and in the region of incidence of the shock wave, where a separation zone was formed. The mesh contained $81\times 61$ calculation points. The minimum mesh size at the lower wall was selected as around $10^{-4}$. It should be noted that the height of the channel through cross section at the exit from the region was taken as the characteristic linear dimension, and the velocity and density of the incoming stream were selected as the scales for making the variables dimensionless. The results of calculations of the flow of a hypersonic stream of viscous gas around an impermeable wall and around a wall with a porous cooling section, in the presence of a decaying shock wave were compared assuming laminar flow (the Reynolds number is 5000). The Mach number was set at 8.2 and the ratio of the wall temperature to that of the gas blown across the porous section was assumed to be 0.27. The porous cooling section was located at the most thermally stressed point (between $x=14$ and $x=16$), corresponding to the point where the shock impacts on the wall. The blown gas pulse was fixed at 5%.

Figures 1 and 2 give the results of a comparative analysis of the flow around a wall without and with blowing. The fields of the flow characteristic near the wall were analyzed when the solution had stabilized, i.e., after steady-state gas flow had been achieved. This state was obtained for dimensionless times greater than 15. The steady-state flow pattern of the viscous gas in the boundary layer reveals a zone of flow stagnation near the wall at the most thermally stressed point, i.e., at the point of incidence of the shock wave. A separation zone is formed at this point although this is fairly weakly defined when there is no blowing. As was to be expected, the presence of a cooled insert does not have any significant influence on the flow field. This is confirmed by a comparative analysis of the pressure and temperature distri-

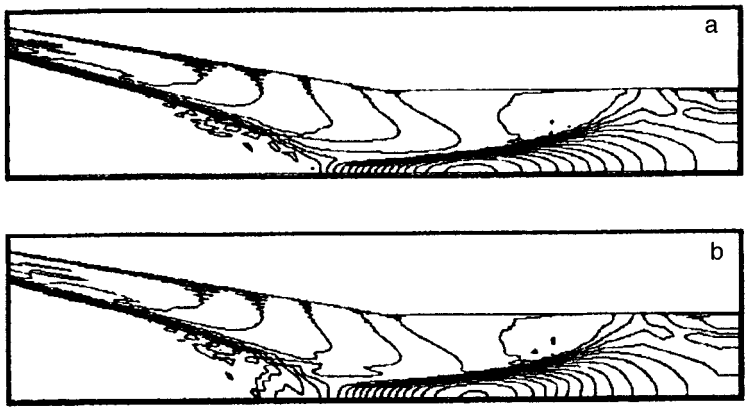


FIG. 1. Comparative analysis of calculated isobar patterns obtained when a hypersonic stream of viscous gas with a decaying shock wave flows around a wall with (a) and without (b) blowing across part of the wall. The lines are plotted: a — with step 1 between 1 and 17 and b — with step 1 between 1 and 18 (the pressures are relative to the pressure in the incoming stream).

bution patterns in the boundary layer with and without blowing. The transformation of the surface distributions of the relative values of the static pressure and heat flux with time demonstrates the establishment of the process in flow around a wall without blowing, with the formation of a thermally stressed zone, corresponding to the point of interaction between the shock and the boundary layer at the plate. From an analysis of the curves in Fig. 2, it is interesting to note that the flow pattern and the distribution pattern of the force and thermal loads is broadly established by the time $T=10$. Blowing has very little influence on the relative pressure profile at the wall. Only a slight increase in pressure is observed at the point when gas blowing is initiated. An analysis of the calculated distributions of the thermal characteristics at the wall shows that blowing across a porous insert can essentially remove the thermal load on the wall, which is responsible for the efficiency of this type of cooling. This conclusion is supported by physical experiments.[5] This numerical analysis has therefore confirmed the concept of porous cooling of thermally stressed sections of streamlined components in objects of various types. It has been noted

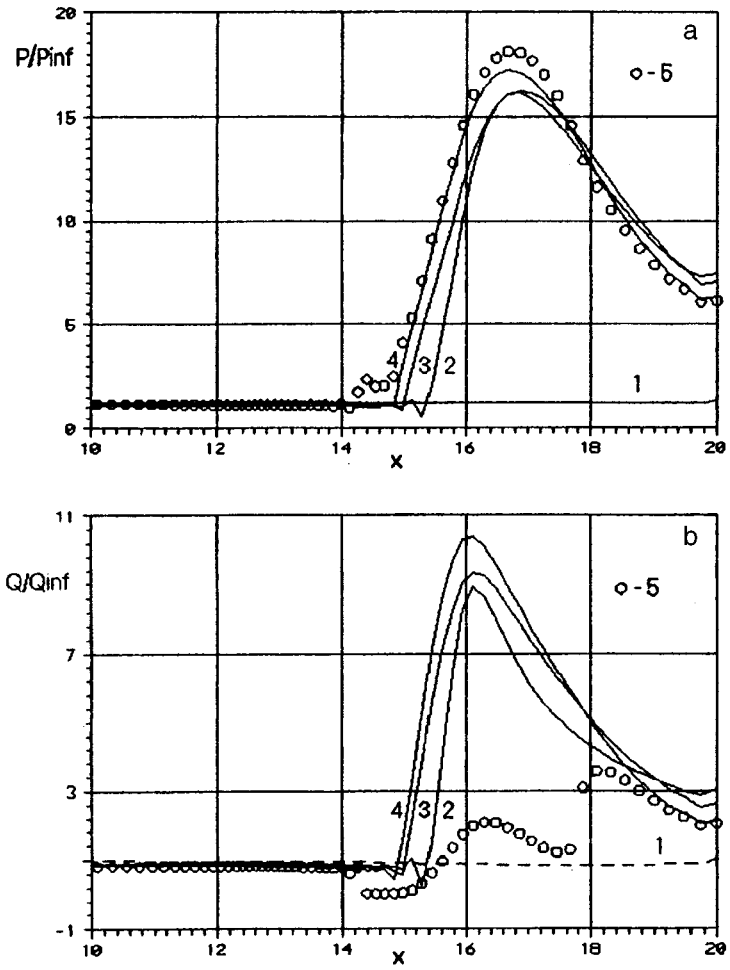


FIG. 2. Comparison of the distributions of the relative pressure $P/P_{\text{inf}}$ (a) and the relative heat flux $Q/Q_{\text{inf}}$ (b) along the wall at various times without (*1–4*) and with blowing (*5*). Here the subscript ''inf'' describes the flow parameter for hypersonic flow along a planar plate. The numbered curves correspond to the following times: *1* — $T=3$; *2* — 10; *3* — 15; *4* — 20; and *5* — 20.

that this type of cooling has a local effect, which does not significantly influence the streamline flow pattern of the object.

This work was supported financially by the Russian Fund for Fundamental Research under Grant No. 96-01-00298.

[1] V. M. Epifanov, S. A. Isaev, and V. V. Nosatov, *Abstracts of papers presented at the International Symposium on Heat Transfer Enhancement in Power Machinery (HTEPM' 95)* MSTU, Moscow 1995. Vol. 2. pp. 151–152.
[2] S. A. Isaev, V. V. Nosatov, and G. A. Sadovnikov, *Proceedings of the Third Minsk International Forum ''Heat and Mass Exchange – MMF-96''*, Vol. 1, *Convective Heat and Mass Exchange*, Part. I [in Russian], ITMO, Minsk (1966), pp. 105–108.
[3] R. V. MacCormack, Aerokos. Tekh. **1**(4), 114 (1983).
[4] D. L. Book, J. P. Boris, and K. Hain, J. Comput. Phys. **18**, 248 (1975).
[5] M. Holden and S. Sweet, AIAA Paper No. 2475, 1 (1994).

Translated by R. M. Durham

# Fabrication of indium arsenic-antimony-bismuthide multilayer heterostructures by ''capillary'' liquid-phase epitaxy

R. Kh. Akchurin, V. A. Zhegalin, T. V. Sakharova, and S. V. Seregin

*M. V. Lomonosov State Academy of High-Precision Chemical Technology, Moscow;*
*Institute of Chemical Problems in Microelectronics, Moscow*
(Submitted November 10, 1996)
Pis'ma Zh. Tekh. Fiz. **23**, 51–55 (April 12, 1997)

Low-temperature ''capillary'' liquid-phase epitaxy is used to grow $InAs_{1-x-y}Sb_xBi_y/InSb_{1-y}Bi_y$ multilayer epitaxial heterostructures on InSb(111)A substrates. The heterostructures contained up to sixty epitaxial layers of thickness between 0.05 and 0.15 $\mu$m, which was controlled by the epitaxial growth conditions. The heterostructures were investigated by scanning electron microscopy and secondary-ion mass spectrometry, and results are presented.
 [S1063-7850(97)00904-X]

Solid solutions of indium arsenic-antimony-bismuthide ($InAs_{1-x-y}Sb_xBi_y$) are attractive materials for the sensing elements of far-infrared ($\lambda = 8-14$ $\mu$m) photodetectors utilizing the intrinsic photoconduction effect. However, the scope for epitaxial deposition of materials with $E_g(77\ \mathrm{K}) < 0.15$ eV is limited by the increased technological difficulties involved in obtaining solid solutions of the required composition ($x \approx 0.6-0.7$), the limited solubility of bismuth in solid solutions ($y \leqslant 0.005$), and also by defects in the epitaxial layers because of the lack of suitable substrate materials to fabricate isoperiodic heterostructures.[1,2]

Numerical estimates were made in Ref. 3 to show that, in principle, a material having the fundamental optical absorption edge at $\lambda \geqslant 12$ $\mu$m at 77 K can be fabricated using multilayer elastically stressed $InAs_{0.39}Sb_{0.61}/InAs_{1-x}Sb_x$ superlattice heterostructures ($x > 0.73$), formed on InSb substrates. Recent success in the fabrication of these heterostructures by molecular-beam epitaxy and gas-phase epitaxy using organometallic compounds and in the development of efficient photodetectors utilizing these materials has stimulated increased interest in these solid solutions.[4–6] According to estimates made in Ref. 7, it is preferable to use elastically stressed $InAs_{1-x-y}Sb_xBi_y/InSb$ heterostructures for this purpose. In order to achieve values of $E_g(77\ \mathrm{K}) = 0.12$–$0.14$ eV, the predicted composition of the $InAs_{1-x-y}Sb_xBi_y$ solid solutions will be in the range $x \approx 0.86-0.92$, allowing for the maximum solubility of bismuth as a function of temperature, and the critical thicknesses of the epitaxial layers to conserve the elastic stresses will be in the range of $0.05-0.1$ $\mu$m.

The feasibility of using ''capillary'' liquid-phase epitaxy to form multilayer elastically stressed $InAs_{1-x-y}Sb_xBi_y$ heterostructures was analyzed in Ref. 8. In accordance with the calculated data, epitaxial layers of uniform composition with sharp heteroboundaries are best achieved by forming heterostructures with alternating epitaxial layers of $InAs_{1-x-y}Sb_xBi_y$ (active layers) and $InSb_{1-y}Bi_y$ (auxiliary stretching layers), grown on an InSb substrate from fluxes of indium and bismuth alloys.

In the present paper, we report results of experimental studies on the development of these structures by the method described above. According to estimates made in Ref. 8, epitaxial layers of subcritical thickness can be grown successfully from presupercooled solutions, at epitaxy temperatures no higher than 300°C, under isothermal conditions, where the time of contact between the solution and the substrate should not exceed 1–3 s. The uniformity of the thickness and composition of the epitaxial layers over the substrate length can be improved by increasing the flux velocity of the liquid in the gap and by using ''relaxation'' types of epitaxy (where the flux is stopped briefly after the solutions are exchanged in the working space between the substrates). The epitaxial growth processes were carried out in an S-3348 liquid-phase epitaxy system in a high-purity hydrogen atmosphere. A flow-through type of graphite container was used with a growth channel 250 $\mu$m thick. The InSb(111)A substrates were subjected to standard chemical treatment. Immediately before epitaxial growth, the substrates underwent additional treatment in the reactor of the liquid-phase epitaxy system to eliminate any defects from the pre-epitaxial treatment and to remove the oxide film. This treatment involved slightly dissolving the surface layer $5-7$ $\mu$m thick by contact between the substrate and an unsaturated In–Sb–Bi flux at 270–280°C. Subsequent cooling in the range of 10–20°C at a rate of 0.4°C/min resulted in the growth of an $InSb_{1-y}Bi_y$ buffer layer $3-5$ $\mu$m thick. The heterostructures were formed by a relaxation type of liquid-phase epitaxy under the following conditions: epitaxy temperature 230–260°C, initial supercooling of solutions 5–20°C, flow-thrugh time 1 s, and pause time 1.4 s.

By regulating the number of flow-through cycles, we obtained heterostructures with between eight and sixty layers. The composition of the $InAs_{1-x-y}Sb_xBi_y$ layers was investigated by secondary ion mass spectrometry with layer-by-layer ion etching using an IMS-3F system. We used a $Cs^+$ primary ion source, with a primary beam energy of 6.5 keV, a beam current of 100 nA, and a secondary ion sampling zone of 60 $\mu$m. The reference samples were epitaxial layers of known composition ($x = 0.96-0.92$) determined by x-ray spectral analysis. The distribution of the concentrations of the main components, arsenic, tin, and antimony, was investigated over the thickness of the epitaxial layers. The surface and cleaved sections of the heterostructures were examined using a Hitachi-800 field-emission scanning electron

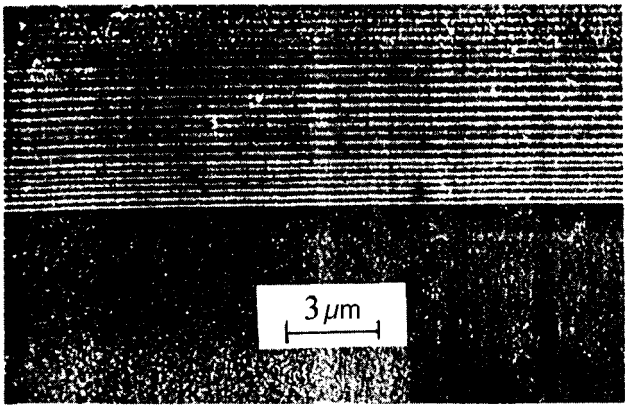


FIG. 1. Electron micrograph of a cleaved section of a $InAs_{1-x-y}Sb_xBi_y/InSb_{1-y}Bi_y$ heterostructure grown on an (111)A InSb substrate.

microscope with incident electron beam energies $E=1-20$ keV.

The thickness of the epitaxial layer was between 0.05 and 0.15 $\mu$m, depending on the growth conditions, and no appreciable spread was observed over the area of the heterostructures (Fig. 1). The distribution profiles of the main components over the thickness of the epitaxial layers obtained by secondary ion mass spectrometry confirm that the heteroboundaries are fairly abrupt (Fig. 2). The InAs concentration in the active layers was 6–7 mol.%.

The results of these preliminary experiments have therefore demonstrated that multilayer heterostructures formed by $InAs_{1-x-y}Sb_xBi_y$ solid solutions with epitaxial layers hundredths of a micron thick can be produced by capillary liquid-phase epitaxy. This enables the elastic stresses to be conserved as a means of influencing $E_g$. By optimizing the compositions and thicknesses of the epitaxial layers, it may well be feasible to use elastically stressed $InAs_{1-x-y}Sb_xBi_y/InSb_{1-y}Bi_y$ heterostructures, fabricated by liquid-phase epitaxy, in infrared technology.

The authors are grateful to T. I. Gromov and P. B. Orlov for their assistance with investigations of the heterostructure samples.

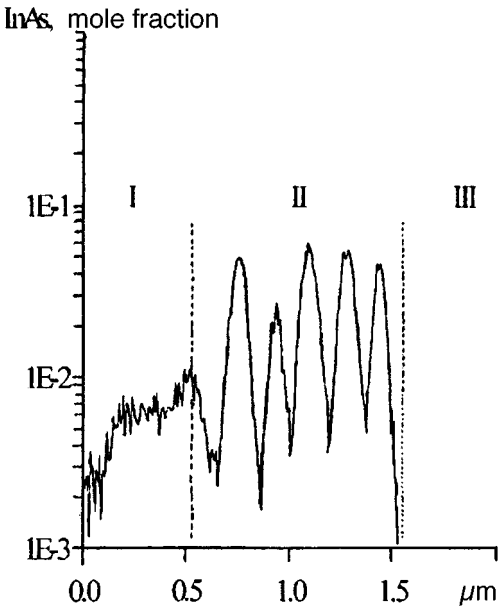


FIG. 2. Concentration profile of a multilayer $InAs_{1-x-y}Sb_xBi_y/InSb_{1-y}Bi_y$ heterostructure, measured by secondary ion mass spectrometry (*I* — coating layer, *II* — main layers, and *III* — buffer layer).

This work was partially supported financially by the State Committee for Higher Education (Grant No. E 460-6, 1994).

[1] R. Kh. Akchurin and T. V. Sakharova, Pis'ma Zh. Tekh. Fiz. **18**(10), 16 (1992) [Tech. Phys. Lett. **18**, 307 (1992)].
[2] R. Kh. Akchurin, V. A. Zhegalin, and T. V. Sakharova, Neorg. Mater. **31**, 1431 (1995).
[3] G. C. Osbourn, J. Vac. Sci. Technol. B **2**, 176 (1984).
[4] S. R. Kurtz, R. M. Biefeld, L. R. Dawson *et al.*, Appl. Phys. Lett. **53**, 1961 (1988).
[5] S. R. Kurtz, L. R. Dawson, Th. E. Zipperian *et al.*, IEEE Electron. Dev. Lett. **11**, 54 (1990).
[6] Z. M. Fang, K. Y. Ma, R. M. Cohen, and G. B. Stringfellow, J. Appl. Phys. **67**, 1187 (1990).
[7] R. Kh. Akchurin and O. V. Akimov, Fiz. Tekh. Poluprovodn **29**, 362 (1995) [Semiconductors **29**, 183 (1995)].
[8] R. Kh. Akchurin and D. V. Komarov, Zh. Tekh. Fiz. (1997) [Tech. Phys. *in press*, (1997)].

Translated by R. M. Durham

# Hydrodynamic characteristics of the propagation of polymerization waves in liquid media

A. S. Segal' and A. V. Kondrat'ev

*State Institute of Precision Mechanics and Optics, St. Petersburg (Technical University)*
(Submitted December 12, 1996)
Pis'ma Zh. Tekh. Fiz. **23**, 56–61 (April 12, 1997)

An analysis is made of the hydrodynamic characteristics of the propagation of thermal polymerization waves in liquid media without hardening of the final polymer product. The process is described mathematically using a system of equations for the dynamics and the heat and mass transfer in a reacting liquid medium, written in the Boussinesq approximation and assuming the simplest overall polymerization reaction. © *1997 American Institute of Physics.* [S1063-7850(97)01004-5]

Thermal waves of polymerization reactions, observed and studied for the first time by Chechilo and colleagues,[1,2] demonstrate a particular example of wave chemical phenomena in condensed media. Compared with other similar phenomena (see, for example, Ref. 3), they have many characteristic features, which were studied in detail by Pojman and colleagues in a series of experiments and allow the process to be visualized directly.[4,5] In particular, when a wave propagates in the direction of the gravitational force, the following effects are observed: 1) the wavefront remains planar and horizontal, despite any slope of the reactor and/or heat losses through the side walls; 2) the front may be preceded by powerful vortex motion of the liquid; 3) pulsation or ''spin'' wave propagation regimes may be established; and 4) polymer ''fingers'' may grow near the front. In the present paper, we report a numerical simulation of the propagation process of a polymerization wave, which can reproduce some of these effects.

The process is described mathematically by using a system of equations for the dynamics and for the heat and mass transfer in a reacting medium, written in the Boussinesq approximation and implying the simplest ''monomer → polymer''overall kinetic polymerization reaction:

$$\partial M/\partial t+(\mathbf{V}\cdot\nabla)M=\nabla\cdot(D\nabla M)-W, \tag{1}$$

$$\rho c[\partial T/\partial t+(\mathbf{V}\cdot\nabla)T]=\nabla\cdot(\lambda\nabla T)+Q\rho W, \tag{2}$$

$$\rho[\partial\mathbf{V}/\partial t+(\mathbf{V}\cdot\nabla)\mathbf{V}]=-\nabla_p+\nabla(2\mu S)+\rho\mathbf{g}(\beta_T\delta T+\beta_M\delta M), \tag{3}$$

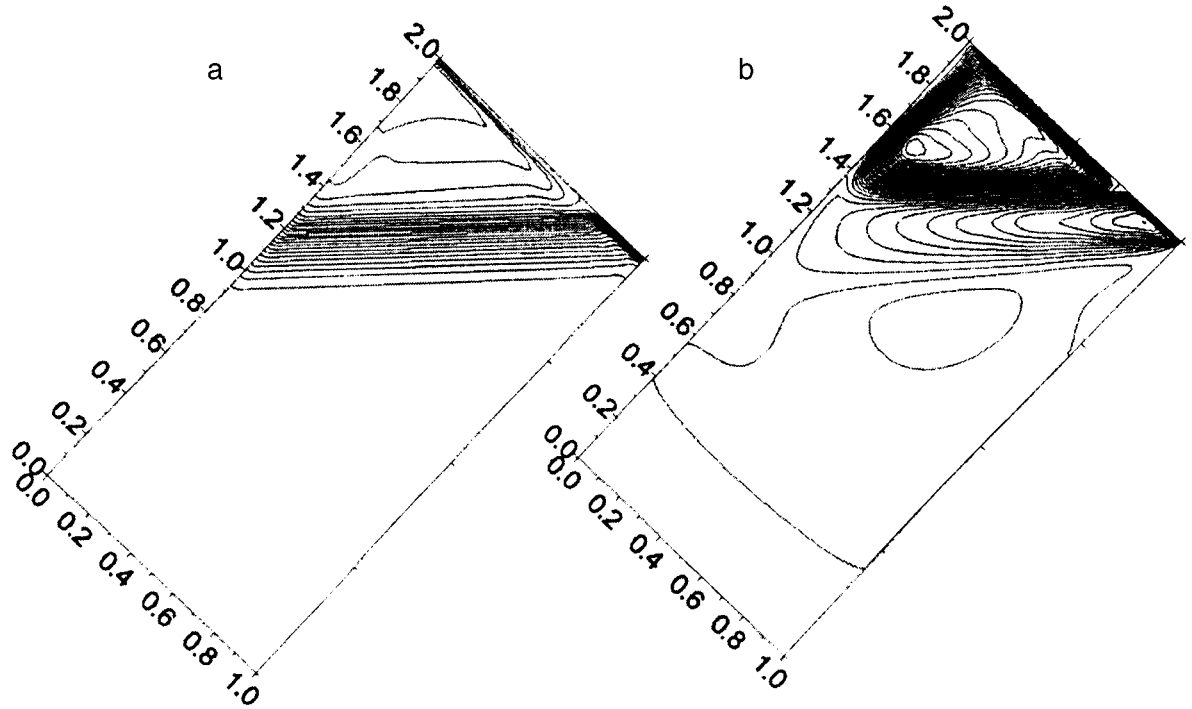


FIG. 1.

 1063-7850/97/040276-03$10.00  

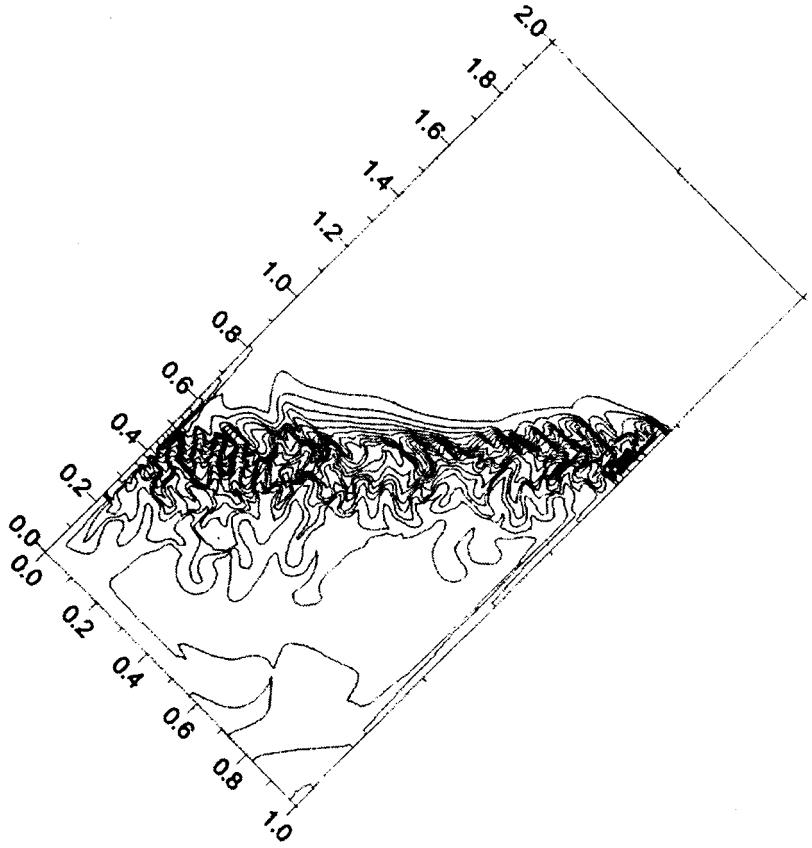


FIG. 2.

$$\nabla \cdot \mathbf{V} = 0, \tag{4}$$

where $\mathbf{V}$ is the velocity vector of the medium, $M$ is the monomer (mass fraction) concentration, $T$ is the temperature, $W$ is the reaction rate, $p$ is the dynamic pressure, $t$ is the time, $\rho$ is the density, $c$ is the specific heat, $Q$ is the reaction energy, $D$ is the binary diffusion coefficient of the monomer–polymer mixture, $\lambda$ is the thermal conductivity, $\mu$ is the dynamic viscosity, $\beta_T$ and $\beta_M$ are the coefficients of thermal expansion and concentration compression, respectively, $\mathbf{g}$ is the vector of the acceleration due to gravity, $\nabla$ is Hamilton's vector operator, and $S$ is the strain rate tensor. The dependence of the reaction rate on the temperature and monomer concentration is expressed in the form

$$W = k_0 \exp(-E/RT) M, \tag{5}$$

where $k_0$ is a preexponential factor, $E$ is the activation energy, and $R$ is the universal gas constant.

An analysis is made of the propagation of a wave in a plane rectangular reactor, initiated from the hot upper wall. Then, the ''ignition'' boundary conditions are set at this wall: $M = 0$,

$$T = T_m = T_0 + Q/c, \tag{6}$$

where $T_0$ is the initial temperature of the medium and $T_m$ is the temperature of adiabatic propagation of the reaction. The other walls are assumed to be impermeable to the medium and adiabatic: $\partial M/\partial n = 0$, $\partial T/\partial n = 0$, where $n$ is the normal coordinate to the corresponding wall. For the velocity vector, we use standard conditions of attachment and impermeability at all walls ($\mathbf{V} = 0$). At zero time, the reactor is assumed to be filled with cold monomer ($M = 1$, $T = T_0$).

The system (1)–(5), with the appropriate initial and boundary conditions, was solved using a partially implicit finite-difference system with an approximation of the spatial derivatives on a spaced MAC-mesh (see, for example, Ref. 6), which linearizes the initial problem. The transition to a new time layer was made by a method of splitting by physical processes and coordinates.

Let us now discuss the results of these calculations. We analyze the behavior of a polymerization wave in a tilted reactor inclined at an angle of 45° to the vertical. The calculations were made for a range of kinetic parameters $k_0$ and $E$ of the reaction which ensures diffusion and thermal stability of the process[7] (no pulsation or spin regimes).

In the first series of calculations, allowance was only made for thermal expansion of the medium caused by the heat released during the polymerization reaction. From the very beginning of the process, the heated liquid was observed to rise along the hot upper wall, transferring heat to the upper corner of the reactor. This caused a buildup of more vigorously heated liquid in this zone and generated a plane horizontal reaction front, which then began to propagate downward (see Fig. 1a, which shows the temperature field contours at one point in time). In Fig. 1b, which shows the current contours at the same time, the lower counterclockwise-rotating vortex is caused by this rise of unreacted liquid along the hot upper wall. The upper vortex is formed because the temperature in the reaction zone is

slightly higher than the temperature $T_m$ maintained at the upper wall (this can be seen from Fig. 1a). In this context, the upper wall was ''cold'' for the reacted liquid behind the front, which resulted in a downward flow of liquid, forming a clockwise vortex.

Note that the vortex motion of the liquid near the front rapidly equalizes the temperature field and stabilizes the front in the horizontal direction. This behavior occurs because the characteristic time for natural convection is shorter than the characteristic times for conduction and chemical reaction, so that free convection is the dominant process (simple estimates yield the following values for these characteristic times: $\tau_{\text{free conv}} \approx 0.25$ s, $\tau_{\text{cond}} \approx 57$ s, and $\tau_{\text{chem}} \approx 5.6$ s).

Allowance for concentration compression of the medium in the course of polymerization (shrinkage) abruptly alters the pattern of wave propagation. In this case, stability is lost because of the interaction between two opposing trends, thermal expansion and concentration compression. It has been established that this interaction may give rise to double-diffusion convection,[5] which induces the growth of polymer fingers at the wavefront, followed by the decay of these fingers into droplets, which sink slowly to the bottom of the reactor. Figure 2 gives the contours of the monomer concentration field, which show the growth of polymer fingers and a layer of heavy cold polymer deposited at the bottom.

The results of this numerical simulation have therefore qualitatively reproduced the main experimentally observed characteristics of the propagation of a polymerization wave in a liquid medium in the range of diffusion thermal stability.


[1] N. M. Chechilo, R. Ya. Khvilivitskiĭ, and N. S. Enikolopyan, Dokl. Akad Nauk SSSR **204**, 1180 (1972).
[2] N. M. Chechilo and N. S. Enikolopyan, Dokl. Akad Nauk SSSR **214**, 1131 (1974).
[3] *Oscillations and Traveling Waves in Chemical Systems*, edited by R. J. Field and M. Burger (Wiley, New York, 1985) [Russ. transl., Mir, Moscow, 1988].
[4] J. A. Pojman, J. Am. Chem. Soc. **113**, 6284 (1991).
[5] J. A. Pojman *et al.*, J. Phys. Chem. **96**, 7466 (1992).
[6] C. A. F. Fletcher *Computational Methods in Fluid Dynamics* [Russ. Transl., Mir, Moscow, 1991]
[7] A. Bayliss and B. J. Matkowsky, J. Comput. Phys. **71**, 147 (1987).


Translated by R. M. Durham

# Thick-layer glycerin-containing bichromated gelatin for recording volume holograms

Yu. N. Denisyuk, N. M. Ganzherli, I. M. Maurer, and S. A. Pisarevskaya

*A. F. Ioffe Physicotechnical Institute, Russian Academy of Sciences, St. Petersburg*
(Submitted December 17, 1996)
Pis'ma Zh. Tekh. Fiz. **23**, 62–65 (April 12, 1997)

A thick-layer light-sensitive material consisting of glycerin-containing bichromated gelatin has been prepared and used to record real-time volume holograms with 0.44 $\mu$m helium–cadmium laser radiation. The thickness of the layers is 400–600 $\mu$m. The holographic sensitivity of the material is 1 J/cm$^2$. The highest diffraction efficiency of holograms recorded using a symmetric system with parallel beams is 32%. © *1997 American Institute of Physics.* [S1063-7850(97)01104-X]

In earlier studies, we proposed and investigated a thick-layer light-sensitive material consisting of gel-like bichromated gelatin, designed to record volume holograms.[1,2] This material has the advantage that the image is reconstructed directly in the hologram recording process, and in layers of around 2 mm thick, and the diffraction efficiency of holograms recorded using a symmetric system with parallel beams may be 17–18%. However, the inadequate diffraction efficiency and the limited information storage time render this material unsuitable for many practical applications.

Another type of self-developing layer of bichromated gelatin with glycerin additives of up to 93% by weight of dry glycerin, having a layer thickness of around 5–10 $\mu$m after drying, is described in the literature.[3] The glycerin in these layers functions as a plasticizer and is also used to store some water molecules which, because of the presence of hydrogen bonds, perform the developing process. In addition, a higher rate of accumulation of photogenerated Cr(V) ions can be achieved because of the good electron-donor properties of glycerin.

We prepared and investigated self-developing glycerine-containing layers of bichromated gelatin, which were around 400–600 $\mu$m thick after drying. The layer fabrication technology differed very little from the casting technology for these thin layers. A molten solution of 6% bichromated gelatin, to which we added 93% glycerin and 5% ammonium bichromate by weight of the dry gelatin, was poured onto a glass substrate at 40 °C. After being left to gel in a refrigerator for 24 h, the layers were then dried at room temperature for several days, during which they decreased in thickness; for example, layers having an initial thickness of 2 mm decreased to 400 $\mu$m.

The main holographic characteristics of the layers were determined by recording holograms of two plane waves, formed from 0.44 $\mu$m helium–cadmium laser radiation. The interfering beams propagated symmetrically with respect to the normal to the surface of the layer and the angle of convergence of the beams was 14°. The diameter of the exposed spot was 10 mm. The power density of the radiation in the plane of the hologram was of the order of 4 mW/cm$^2$. The reconstructed wave appeared in the first few seconds of the hologram recording process. A typical curve of the diffraction efficiency versus the exposure is plotted in Fig. 1. It can be seen that this curve has two peaks with the highest diffraction efficiency being observed at the second peak. For 0.5 mm thick layers, this maximum diffraction efficiency is 32% for an exposure of 5.4 J/cm$^2$. With allowance for the parameters of the exposing radiation, the holographic sensitivity of this material can be estimated as 1 J/cm$^2$, which is better than that of the gel-like bichromated gelatin layers described by us previously.

An increase in the angle of convergence of the interfering beams during the hologram recording process reduces the highest attainable diffraction efficiency to 21%, when this angle is 20° (spatial frequency $\nu = 790$ mm$^{-1}$), 6% for 30° (1180 mm$^{-1}$), and 2% for 40° (1330 mm$^{-1}$). Assuming that a hologram diffraction efficiency of 1% is sufficient, the resolution of the self-developing layers of glycerin-containing bichromated gelatin may be taken to be 1200 mm$^{-1}$.

Measurements were also made of the angular selectivity of the holograms recorded with an angle of convergence of 14° as a function of the exposure. The readout wavelength was $\lambda = 0.63$ $\mu$m. Figure 2 gives the diffraction efficiency as a function of the angle of incidence of the reconstructing radiation for exposures of 5.4 J/cm$^2$ (curve *1*), 1 J/cm$^2$ (curve *2*), and 0.5 J/cm$^2$ (curve *3*). The angular selectivity improves with increasing exposure and is 40′ at the half-maximum of the distribution for the hologram with the highest diffraction efficiency (curve *1*). The thickness of the bichromated gela-

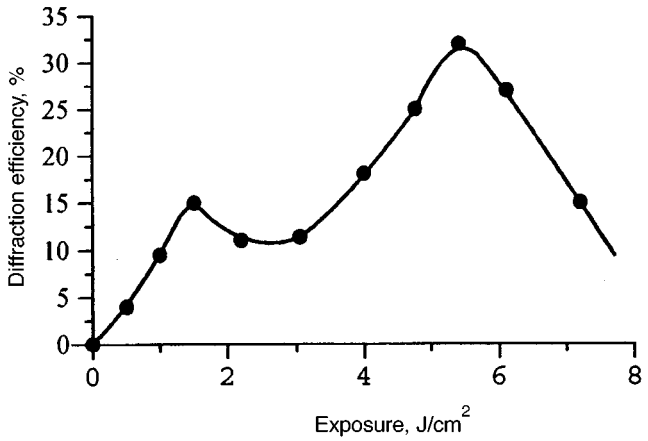


FIG. 1. Diffraction efficiency of the holograms as a function of exposure.

 1063-7850/97/040279-02$10.00  

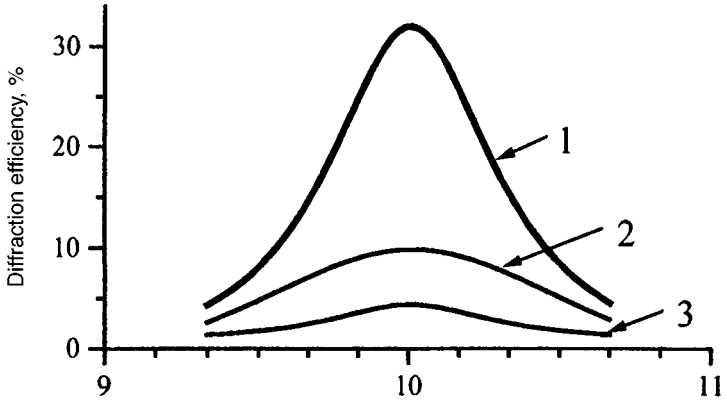


FIG. 2. Diffraction efficiency of the holograms as a function of the angle of incidence of the readout beam for different exposures: *1* — 5.4 J/cm$^2$, *2* — 1 J/cm$^2$, and *3* — 0.5 J/cm$^2$.

tin layer on which the hologram was recorded was 400 $\mu$m. An estimate of the effective layer thickness corresponding to an angular selectivity of 40′, made using a formula derived in Ref. 4 in an approximation valid for low diffraction efficiency, yields a value of the order of 150 $\mu$m. Having regard to the approximate nature of this theoretical estimate of the effective layer thickness, the agreement between the theoretical estimate and the real thickness may be considered to be satisfactory.

It should be noted that, as well as having the capacity for self-development of a latent image, the proposed thick-layer light-sensitive material can also store recorded holographic information for a fairly long time without any appreciable deterioration in the diffraction efficiency because water molecules are stored as complexes with glycerin in the dried layer of gelatin. The layer thickness only decreases negligibly over time as a result of drying out. Exposure of the recorded holograms to radiation from a mercury lamp for a fairly long time also causes no significant changes in the holographic characteristics.

This light-sensitive material is fairly easy and cheap to produce. The layers may be used for recording three-dimensional images by the method of referenceless selectograms and also for investigations of optical memories.

This work was supported by the Russian Fund for Fundamental Research (Grant 95-02-03887) and also by the CRDF Fund (Grant RE2-162).

[1] Yu. N. Denisyuk, N. M. Ganzherli, and I. A. Maurer, Pis'ma Zh. Tekh. Fiz. **21**(17), 51 (1995) [Tech. Phys. Lett. **21**, 703 (1995)].
[2] Yu. N. Denisyuk, N. M. Ganzherli, and I. A. Maurer, Proc. SPIE **2688**, 42 (1995).
[3] V. V. Sherstyuk, A. N. Malov, S. M. Maloletov, and V. V. Kalinkin, Proc. SPIE **1238**, 218 (1989).
[4] Yu. N. Denisyuk, Zh. Tekh. Fiz. **60**(6), 59 (1990) [Sov. Phys. Tech. Phys. **35**, 669 (1990)].

Translated by R. M. Durham

# Growth of delta-doped silicon layers by molecular beam epitaxy with simultaneous low-energy ion bombardment of the growth surface

Sh. G. Shengurov, V. N. Shabanov, and A. V. Shabanov

*N. I. Lobachevskiĭ Physicotechnical Scientific-Research Institute, Nizhniĭ Novgorod State University*
(Submitted September 23, 1996)
Pis'ma Zh. Tekh. Fiz. **23**, 67–72 (April 12, 1997)

It is shown that high-quality structures may be fabricated by applying a potential to the substrate to obtain *n*- and *p*-type delta-layers during low-temperature growth of epitaxial layers from subliming silicon sources doped with antimony or gallium. © *1997 American Institute of Physics.* [S1063-7850(97)01204-4]

Delta-doped layers are attracting interest among researchers because of the possibility of producing fundamentally new electronic devices.[1,2] Delta-doped silicon layers are usually obtained by molecular-beam epitaxy, either combined with solid-phase epitaxy[1,3,4] or with low-energy ion implantation.[5,6] These techniques are used because of the need to suppress segregation effects inherent in conventional molecular beam epitaxy, as a result of which it is impossible to obtain layers with an dopant concentration close to the solid-phase solubility limit and abrupt transition regions. However, these methods use relatively high temperatures ($\geqslant 650°$C) to anneal the layers, which increases the diffusion spreading of the dopant concentration profile in the delta-layer.

However, it has been established[7,8] that segregation of the dopant can be reduced by applying a negative potential to the substrate during the growth process when silicon is evaporated using an electron gun. The low-energy $Si^+$ ions formed by ionization of the molecular flux activate trapping of dopant (mainly donors) from the adlayer. Appreciable thermionic emission was also established during the sublimation of silicon.[9,10] We observed an increase in the transport coefficient of donor and acceptor dopants during the epitaxial growth of silicon, when a negative potential was applied to the substrate.[10–13]

In the present paper, we demonstrate the feasibility of applying a potential to the substrate to obtain *n*- and *p*-type delta-layers during the low-temperature growth of epitaxial layers from subliming silicon sources doped with antimony or gallium.

The layers were grown by a procedure described in Refs. 10–13. The sources of the silicon and dopant fluxes were rectangular silicon blocks cut from KÉS-0.01, KDG-0.06, and KDG-0.005 single crystals. The substrates were rectangular wafers of (110) and (100) oriented KÉF-0.005 or KDB-0.01 silicon. The substrate and the source were placed parallel to each other in a growth chamber and were heated by passing a current. The growth rate of the layers was $\sim 0.8-0.9$ nm/s and the residual gas pressure during growth did not exceed $1.3\times 10^{-5}$ Pa.

After high-temperature (1330°C) purification of the substrate surface from any passivating oxide film, the temperature was reduced to 700°C and a $\sim 1$ $\mu$m thick buffer layer was grown. During this growth process, the substrate temperature continued to decrease to $\sim 520°$C. A negative potential relative to the source, $V=30-300$ V, was then applied to the substrate for time $t=3$ s and the layer growth continued. A layer 30–200 nm thick was grown after the potential was switched off.

Figure 1 gives the results of a secondary ion mass spectroscopic (SIMS) analysis of the antimony distribution over the depth of an epitaxial structure grown on Si(100) with the brief application of a potential $V=-100$ V. The structure consisted of a 1 $\mu$m thick buffer layer, a $\delta$-layer, and a 60 nm thick upper layer. The profile has one peak caused by an increase in the dopant concentration at the instant when the potential is applied, and another peak near the surface of the layer, which is caused by the buildup of antimony on the growth surface as a result of its segregation and is a fraction of a monolayer thick.[14]

The thickness of the $\delta$-layer cannot be estimated directly because of the ion mixing effect of the SIMS profile. However, it can be seen that the peak inside the epitaxial structure and the peak near the surface are of similar width and height, which suggests that the thickness of the internal doped layer is small (less than 8 nm) and the dopant concentration in it is fairly high.

The SIMS data also indicate that the boundary of the $\delta$-layer is abrupt. It should be noted that the impurity concentration in the upper layer is close to the concentration in the buffer layer.

Similar SIMS profiles were obtained for the gallium-doped layers. Figure 2 gives the calculated hole concentration profile in the $\delta$-layer for a two-dimensional concentration of electrically active dopant $N_s=5.64\times 10^{11}$ cm$^{-2}$ and a background acceptor concentration $N_a=5\times 10^{15}$ cm$^{-3}$. Also plotted are the experimentally measured concentrations determined from capacitance-voltage measurements. In our view, satisfactory agreement is observed between the calculated and measured values, particularly at high concentrations. The asymmetry of the measured profile is probably caused by some asymmetry in the doping of the $\delta$-layer. In addition, the $\delta$-doping approximation is evidently not satisfied at low dopant concentrations ($<5\times 10^{17}$cm$^{-3}$).

It was also established that as the applied potential is increased, the maximum dopant concentration increases somewhat. For example, for layers doped with gallium, application of the potential $V=-300$ V to the substrate increased the concentration by a factor of approximately 2.7 compared with the case $V=-100$ V.

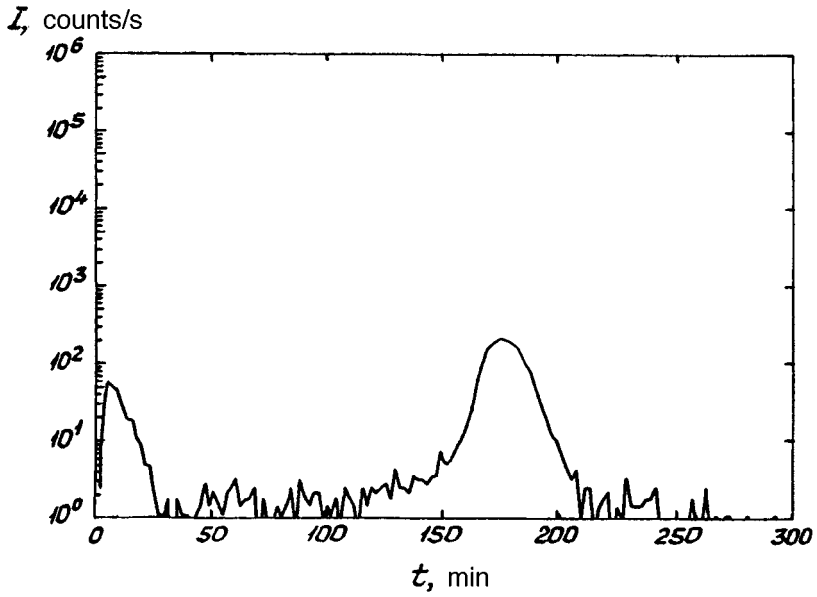


FIG. 1. SIMS profile of the antimony distribution over the thickness of a silicon epitaxial layer grown under the short-lived (3 s) application of a potential $V=-100$ V to the substrate.

Capacitance-voltage measurements of structures with $\delta$-doped layers showed that the maximum concentrations were $\sim 1.5\times 10^{13}$ cm$^{-2}$ for $n$-type layers and $4\times 10^{14}$ cm$^{-2}$ for $p$-type layers. According to the C–V data, the carrier concentration profiles are very steep (the half-width of the hole profile is $\sim 2$ nm).

All the layers were single-crystal, regardless of the doping level, and the electron diffraction patterns only contained Kikuchi lines. When examined under a transmission electron microscope, layers having a surface concentration $N_s \leqslant 1.5\times 10^{13}$ cm$^{-2}$ revealed a low dislocation density ($\sim 10^3$ cm$^{-2}$), whereas layers having the concentration $N_s \sim 4\times 10^{14}$ cm$^{-2}$ revealed a pileup of dislocation loops with the density $\sim 10^5$ cm$^{-2}$.

The formation of sharp dopant concentration peaks in epitaxial layers grown under the pulsed application of a potential may be explained as follows. It is known that gallium and antimony are dopants which segregate at the surface at low growth temperatures.[4,14,15] As a result, a thin adlayer of dopant is always present on the surface of the growing layer. When a negative potential is applied to the substrate, dopants from the adlayer begin to be efficiently trapped by the growing layer under the ion bombardment. We established earlier[13] that the degree of ionization of the silicon flux incident on the substrate is $10^{-7}-10^{-6}$. Thus, during growth of the doped layer, the ion dose did not exceed $10^{10}$ cm$^{-2}$, i.e., there are $\sim 50$ atoms trapped by the dopant layer per incident ion. Some of the atoms become embedded in the layer as a result of doping with recoil atoms.[14] However, a substantial increase in the concentration of implanted dopant cannot be explained by a negligible flux of low-energy ions. A more likely mechanism is the activation of dopant trapping, for example, by rearrangement of the surface and the generation of surface defects. Similar conclusions were reached by other researchers who performed similar experiments using high energies and ion fluxes.[7,8] The increase in the maximum dopant concentration with increasing potential is most likely caused by an increase in the density of defects generated in the surface layer under bombardment by higher-energy ions, and may also be caused by an ion focusing effect.

Thus, by using the ion component of the molecular flux from the subliming silicon source and applying a small negative potential, $\delta$-doped layers having a surface concentration of $\sim 1.5\times 10^{13}$ cm$^{-2}$ for $n$-type layers and $\sim 4\times 10^{14}$ cm$^{-2}$ for $p$-type layers can be obtained at low growth temperatures ($\sim 520$°C).

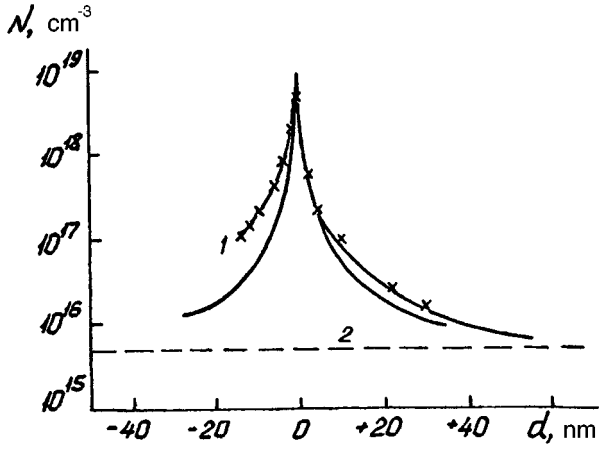


FIG. 2. Calculated hole concentration profile in the delta-layer (solid curve), hole profile measured with a C–V profilometer (*1*), and background acceptor concentration (*2*).


[1] A. A. Van Gorkum, K. Nakagawa, and Y. Shiraki, J. Appl. Phys. **65**, 2485 (1989).
[2] G. H. Dohler, Surf. Sci. **73**, 97 (1978).
[3] A. V. Zotov, A. A. Saranin, V. G. Livshits, and E. A. Khramtsova, Pis'ma Zh. Tekh. Fiz. **15**(24), 1 (1989) [Sov. Tech. Phys. Lett. **15**, 954 (1989)].
[4] S. I. Stenin, B. Z. Kanter, and A. I. Nikiforov, Rost. Kristallov. **18**, 81 (1990).
[5] M. W. Denhoff, T. E. Jackman, J. P. McCaffrey *et al.*, Appl. Phys. Lett. **54**, 1332 (1989).
[6] N. Djebbar, J. Gutierrez, H. Charki *et al.*, Thin Solid Films, **184**, 37 (1990).

[7] R. A. A. Kubiak, W. Y. Leong, and E. H. I. Parker, Appl. Phys. Lett. **46**, 565 (1989).
[8] F. Schaffler and H. Jorke, Thin Solid Films. **184**, 75 (1990).
[9] A. V. Kozhukhov, B. Z. Kanter, B. M. Turovskiı, and S. M. Chesnokov, Poverkhnost' **4**, 160 (1989).
[10] P. V. Pavlov, V. N. Shabanov, V. G. Shegurov, and A. V. Kozhukhov, Poverkhnost' **11**, 153 (1990).
[11] V. G. Shengurov and V. N. Shabanov, Poverkhnost' **12**, 98 (1993).
[12] V. G. Shengurov and V. N. Shabanov, Vysokochist. Veshchest. **2**, 52 (1995).
[13] V. G. Shengurov and V. N. Shabanov, *Abstracts of Papers Presented at the Twelfth International Conference ''VIP-95''* [in Russian], Zvenigorod, 1995, p. 164.
[14] G. E. Becker and J. C. Bean, J. Appl. Phys. **48**, 3395 (1977).
[15] Y. Ota, J. Electrochem. Soc. **124**, 1795 (1977).

Translated by R. M. Durham

# Irregular dynamics of a chain of circle maps with quasiperiodic excitation

T. E. Vadivasova, O. Sosnovtseva, and V. S. Anishchenko

*Saratov State University*
(Submitted December 16, 1996)
Pis'ma Zh. Tekh. Fiz. **23**, 73–79 (April 12, 1997)

An analysis is made of the spatial evolution of quasiperiodic regimes in a chain of coupled circle maps. Mechanisms for the appearance of strange nonchaotic dynamics and the properties of irregular attractors are analyzed. © *1997 American Institute of Physics.*
[S1063-7850(97)01304-9]

Chains and grids of individual elements possessing nontrivial dynamics represent a very simple model of a distributed medium and have thus been studied fairly intensively.[1–9] Compared with other one-dimensional maps, the circle map

$$x(n+1)=x(n)+\Omega-(K/2\pi)\sin(2\pi x(n)),\ \mod 1$$

possesses far richer dynamics. This map demonstrates various periodic, quasiperiodic, and chaotic regimes. A chain consisting of such elements provides greater scope for studying various scenarios in the evolution of nontrivial dynamics but so far, has been very little studied.

It may be postulated that, under certain conditions, the unidirectional influence of preceding elements on subsequent ones, assuming the existence of quasiperiodic oscillations in these elements, should generate so-called nonchaotic strange attractors, i.e., fractal sets possessing no mixing property. The concept of nonchaotic strange attractors was introduced in Ref. 10. Studies[11,12] have shown that the strange nonchaotic attractor is typical of systems with quasiperiodic excitation. Various mechanisms are known for the destruction of ergodic qausiperiodic oscillations, resulting in nonchaotic strange attractors: 1) a torus crisis, where a fractal structure is formed at the instant when a stable invariant curve (which is a mathematical transform of two-frequency quasiperiodic oscillations) comes in contact with an unstable one in a certain set of points[12,13] and 2) loss of torus smoothness.[14] Thus, the concept of irregular dynamics should include not only chaotic regimes but also regimes corresponding to strange nonchaotic behavior.

The aim of the present paper is to analyze the mechanisms for the evolution of chaotic and nonchaotic oscillations in a chain of unidirectionally coupled circle maps.

The discrete model studied may be written in the form :

$$x_0(n+1)=x_0(n)+\theta_0,\ \mod 1$$

$$x_1(n+1)=x_1(n)+\Omega_1-(K_1/2\pi)\sin(2\pi x_1(n))+A\cos(2\pi x_0(n)),\quad \mod 1$$

$$x_j(n+1)=x_j(n)+\Omega_j-(K_j/2\pi)\sin(2\pi x_j(n))+\gamma\cos(2\pi x_{j-1}(n)),\quad \mod 1$$

where $j=2,\ 3,\ldots,\ m$ is the number of the partial cell (the spatial coordinate), and $n$ is the discrete time. All partial cells ($j>1$) are assumed to be identical. The influence of the preceding cell on the subsequent one is described by the coupling coefficient $\gamma$. The cell having the number $j=1$ is influenced by the cell of number $j=0$, possessing the rotation number $\theta_0$. If $\theta_0$ is irrational, this influence is quasiperiodic (in a flow system this corresponds to two-frequency excitation with the frequency ratio $\omega_1/\omega_2=\theta_0$). The excitation intensity is characterized by the parameter $A$.

We briefly list the effects observed in the chain for different parameters.

1. In the supercritical region ($K>1$), when $A=0$, chaos may be observed as a result of a finite number of doubling bifurcations along the chain (similar to the results obtained in Refs. 3 and 5). However, a very weak qausiperiodic excitation destroys the chaos and leads to the formation of nonchaotic strange attractors. Figure 1a shows $(x_0-x_j)$ projections of the phase trajectories for cells with $j=4,\ 5,\ 6$. The parameters were: $K=1.55$, $\Omega=0.5$, $\gamma=0.13$, and $A=0$. In this case, chaotic dynamics appear in the fifth cell. The Lyapunov exponent for this subsystem is $\lambda=+0.0434$. The following cells do not add positive Lyapunov exponents and appear to relay the chaotic dynamics formed in the fifth cell. Figure 1b gives phase portraits for the same cells, for the same parameters, and the same initial conditions, but with a weak quasiperiodic excitation $A=0.001$ having the rotation number equal to the golden mean $\theta_0=0.5(\sqrt{5}-1)$. Instead of chaos, a nonchaotic strange attractor regime ($\lambda=-0.0516$) is observed in the fifth and following cells. A further increase in the excitation leads to fractalization of the invariant curve in cells with $j<5$.

2. A quasiperiodic influence on the elements of the chain in the range $K>1$ may not only destroy but may also induce the evolution of chaotic dynamics along the chain. For example, when $K=1.65$, $\Omega=0.5$, $A=0.15$, and $\theta_0=0.5(\sqrt{5}-1)$, a nonchaotic strange attractor regime is established in the first cell ($j=1$), whereas in the following cells, the development of chaos may be observed for a certain range of variation of the coupling parameter $\gamma \in [0.13,0.29]$. For $\gamma=0.2$ each successive cell $j=2,3\ldots9$ adds a positive Lyapunov exponent to the Lyapunov characteristic exponent. Thus, hyperchaos evolves along the chain. Outside this range of $\gamma$ values, no chaos appears in any cell.

3. Under conditions of fairly strong coupling along the chain, chaos stabilization may be observed, similar to that studied in Ref. 4. For example, for the parameters $K=2.0$, $\Omega=0.5$, $A=0.15$, and small $\gamma\sim0.1-0.2$, an almost linear increase in the Kolmogorov entropy $H_j=\Sigma_{i=1}^{j}\lambda_i^+$ with increasing $j$ is observed in the first thirty cells. With increasing

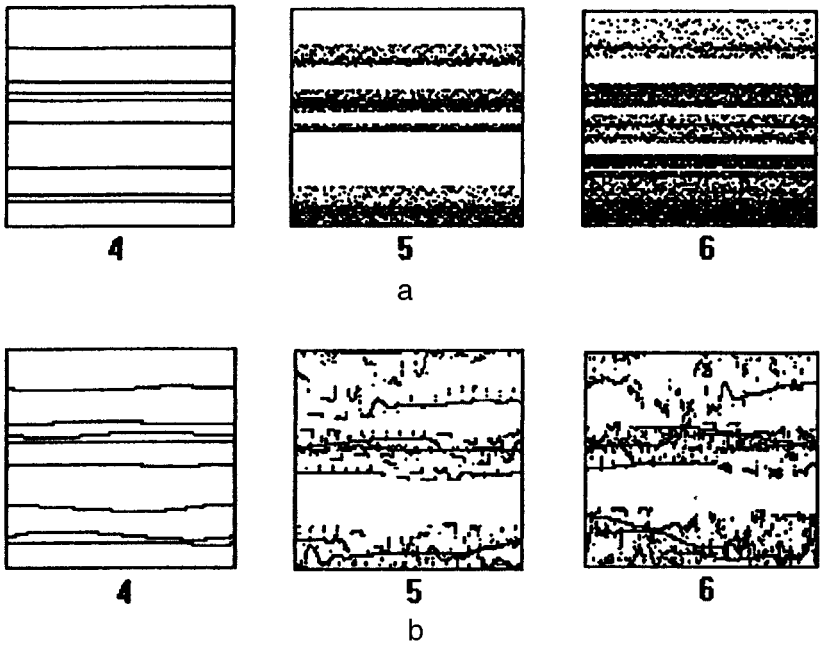


FIG. 1. $(x_0-x_j)$ projections of phase portraits for $j=4,\ 5,\ 6$ for $K=1.55$, $\Omega=0.5$, and $\gamma=0.13$: a — without any external excitation $A=0$; b — with external quasiperiodic excitation $A=0.001$.

coupling parameter $\gamma$, the following cells cease to add positive Lyapunov exponents and the entropy ceases to increase along the chain (for example, for $\gamma=0.4$ the entropy is stabilized from the second cell onward).

4. Whereas in the supercritical region $(K>1)$, two types of nontrivial dynamics may develop along the chain, for $K<1$ chaotic behavior is excluded (for $K<1$ the partial cell is a reversible one-dimensional map, which cannot possess chaotic dynamics either in its own right or under external excitation). Studies have shown that this case is typified by the evolution of nonperiodic, nonchaotic oscillations along the chain. This evolution takes place for various values of the cell parameters and degrees of coupling.

5. It should be noted that in the subcritical region $(K<1)$, a strange nonchaotic attractor may appear not only as a result of the destruction of two-frequency quasiperiodic oscillations (invariant curve) but also as a result of the destruction of three-frequency quasiperiodic oscillations (and clearly, in the general case of $N$-frequency quasiperiodic oscillations). Figure 2a gives $(x_0-x_j)$ projections of the phase trajectories in cells with $j=4,\ 5,\ 6$ for the case of a quasiperiodic influence with the rotation number $\theta_0=\sqrt{2}-1$ (silver mean) on the first element of the chain with the excitation amplitude $A=0.058$. The parameters of the chain elements are $K=0.8$ and $\Omega=0.610074$, which corresponds to a qua-

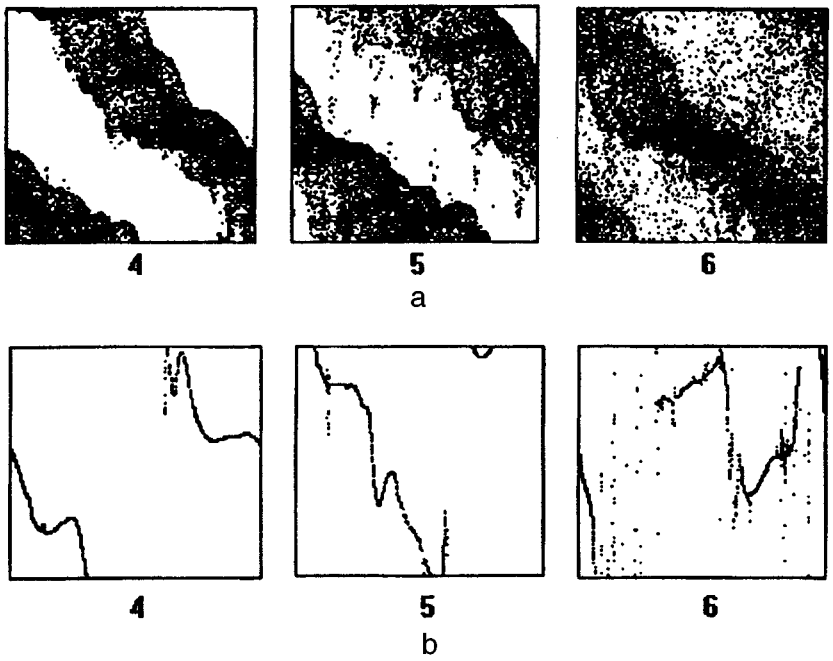


FIG. 2. a — $(x_0-x_j)$ projections of phase portraits; b — Poincaré cross section in the plane $x_1=0.5$ for $j=4,\ 5,\ 6$ where $K=0.8$, $\Omega=0.610074$, $\gamma=0.2$, and $A=0.058$.

siperiodic regime in a partial cell with a rotation number approximately equal to the golden mean. The coupling parameter $\gamma$ is 0.2. A three-frequency quasiperiodic regime is established in the first elements of the chain. Its evolution with increasing $j$ is difficult to identify from the two-dimensional projection of the phase portrait. Thus, a cross section of the phase portrait in a plane, which can reduce the dimensionality of the set to unity, is introduced to analyze the dynamics. Figure 2b shows $(x_0 - x_j)$ projections of the phase portrait cross sections in the plane $x_1 = 0.5$ for $j = 4,\ 5,\ 6$. The cross sections are constructed with an accuracy of $10^{-4}$. It can be seen that for $j = 4,\ 5$ the curve obtained in the cross section is smooth, which corresponds to the three-frequency quasiperiodic regime. The sixth cell reveals fractalization of the curve in the cross section, similar to the fractalization of the invariant curve corresponding to two-frequency quasiperiodic oscillations.

In summary, these investigations have shown that a chain of circle maps is typically characterized by effects already studied for chains with different partial elements (such as period doubling bifurcations and the evolution of chaos along the spatial coordinate, multistability, saturation of chaos along the chain, and so forth), as well as by new effects arising from the possibility of quasiperiodic regimes. A typical consequence of defining a quasiperiodic regime even in the zeroth element of the chain (quasiperiodic excitation) is the appearance of coarse nonchaotic strange attractors over a wide range of parameters in cells from a certain number $j$.

A chain of circle maps also provides scope for introducing mismatch between the cell parameters which control their rotation numbers, so that multifrequency, quasiperiodic regimes may be obtained and their destruction may be studied. Such an investigation will form the subject of further experiments.

This work was partially financed by a grant from the Russian State Committee on Higher Education in Fundamental Natural Science (Grant No. 95-0-8.3-66).

[1] A. V. Gaponov-Grekhov, M. I. Rabinovich, and I. M. Starobinets, JETP Lett. **39**, 688 (1984).
[2] S. P. Kuznetsov, Izv. Vyssh. Uchebn. Zaved. Fiz. **27**(6), 87 (1984).
[3] S. P. Kuznetsov and A. S. Pikovskiĭ, Izv. Vyssh. Uchebn. Zaved. Radiofiz. **28**, 308 (1985).
[4] V. S. Anishchenko, D. É. Postnov, and M. A. Safonova, Pis'ma Zh. Tekh. Fiz. **12**, 1505 (1985) [Sov. Tech. Phys. Lett. **12**, 622 (1985)].
[5] V. S. Anishchenko, I. S. Aranson, D. E. Postnov, and M. I. Rabinovich, Dokl. Akad. Nauk SSSR **286**, 1120 (1986) [Sov. Phys. Dokl. **31**, 169 (1986)].
[6] J. P. Crutchfield and K. Kaneko, *Directions in Chaos* (World Scientific, Singapore, 1987).
[7] K. Kaneko, Physica D **37**, 60 (1989).
[8] A. P. Kuznetsov and S. P. Kuznetsov, Izv. Vyssh. Uchebn. Zaved. Radiofiz. **34**(2), 142 (1991).
[9] S. P. Kuznetsov, Chaos Solitons Fractals **2**, 281 (1992).
[10] C. Grebogi, E. Ott, S. Pelikan, and J. Yorke, Physica D **13**, 261 (1994).
[11] M. Ding, C. Grebogi, and E. Ott, Phys. Rev. A **39**, 2593 (1989).
[12] U. Feudel, J. Kurths, and A. Pikovsky, Physica D **88**, 176 (1995).
[13] J. F. Heagy and S. M. Hammel, Physica D **70**, 140 (1994).
[14] V. S. Anishchenko, T. E. Vadivasova, and O. Sosnovtseva, Phys. Rev. E **53**, 4451 (1996).

Translated by R. M. Durham

# Free oscillations in a ferroelectric liquid crystal

A. P. Fedoryako, M. N. Pivnenko, E. V. Popova, and V. P. Seminozhenko

*Institute of Single Crystals, National Academy of Sciences of Ukraine, Kharkov*
(Submitted November 27, 1996)
Pis'ma Zh. Tekh. Fiz. **23**, 80–85 (April 12, 1997)

A description is given of experimental investigations in which free electromechanical oscillations are obtained for the first time in ferroelectric liquid crystals. © *1997 American Institute of Physics.* [S1063-7850(97)01404-3]

Resonance effects have been observed in studies of forced electromechanical oscillations in a ferroelectric liquid crystal.[1] The authors supposed that these effects were caused by a chevron texture in the sample, but this supposition was not substantiated. Since the chevrons divide the crystal single domain into separate elements, the discreteness of the material and the interaction between structural elements must be taken into account in the deformation process. It is extremely important to estimate the parameters of the statistical ensemble of molecules which is involved in the oscillatory motion and determines the inertial properties of the resonant structure. We propose to study free oscillations rather than forced oscillations to determine the inertial properties of resonant structures. We then describe experimental investigations, in which free electromechanical oscillations were obtained for the first time in a ferroelectric liquid crystal and were observed as a nonmonotonic relaxation to bulk polarization equilibrium. The moment of inertia of a structural element is estimated. Oscillatory resonant structures are interesting as a new direction in the study of dynamic processes in these crystals, and may extend the range of practical application of liquid crystals.

For the investigations we used a binary mixture of the achiral smectic *C* 2-(4-octyloxyphenyl)-5-octylpyrimidine and the chiral additive bis-4,4′-(2-*s*-methylpentyl)-terphenyldicarboxylate. These compounds have frequently been used to study the nature of spontaneous polarization.[2] The composition used (additive concentration = 19.7 wt.%) has the following phase transition temperatures:

$$I \xrightarrow{66\ ^\circ\mathrm{C}} \mathrm{Sm}A \xrightarrow{60\ ^\circ\mathrm{C}} \mathrm{Sm}C^*,$$

where $I$ is the isotopic phase, Sm$A$ is a smectic $A$, and Sm$C$* is a chiral smectic $C$. The spontaneous polarization $P_S$ is 9 nC/cm$^2$ at $T=58$ °C. The crystal was placed between glasses having a transparent conducting coating. Planar boundary conditions were achieved by applying an orientant. The layer thickness was 24 $\mu$m and was normalized by means of spacers. The lower glass was clamped firmly to a heating element, while the upper glass was left free. To the cell we applied rectangular heteropolar voltage pulses of 10 ms duration, which generated an electric field $E$ of up to $10^4$ V/cm. Measurements were made of the polarization reversal current induced by reversal of the electric field polarity in the sample. In the temperature range $\Delta T<4$ °C, we observed complex, multifrequency, slowly decaying oscillations against the background of the polarization reversal pulse (Fig. 1a; $\Delta T=T^*-T$ is the difference between the Sm$A\rightarrow$Sm$C$* phase transition temperature and the observation temperature). The instant of reversal of the electric field polarity is taken as the origin in Fig. 1a.

The maximum amplitude and power of these oscillations are comparable with the amplitude of the current and the power of the polarization reversal pulse. The oscillations have the highest intensity at $\Delta T=1.75$ °C and $E=8.75\times10^3$ V/cm. In this case, the oscillation power is at least three orders of magnitude higher than the noise of the measuring apparatus. The frequency spectrum covers between 4 and 16 kHz. The decay time of the oscillations is around 10 ms. The high temporal stability of all the oscillation characteristics should be noted. The oscillatory response to each pulse repeats the previous one with a relative deviation of less than $10^{-3}$. This stability allowed us to acquire data for 100 or more cycles, and increased the signal-to-noise ratio by more than an order of magnitude. This is necessary at the edges of the temperature range of the oscillations, $\Delta T<1$ °C and $\Delta T>3$ °C, where the amplitude of the oscillations does not exceed the noise level. The transient nature of the process rules out simple methods of spectral analysis. Thus, the entire time interval of the oscillations was divided into overlapping segments, of duration such that the assumption of a steady-state process was valid, to some degree of accuracy, within each segment. Fourier analysis was used in an individual segment. The frequencies and amplitude ($A$) of the spectral components obtained referred to the time at the center of the segment. The oscillation spectrum for the initial time (Fig. 1b) characterizes the establishment of the oscillations i.e., the mechanism for transfer of energy from the field reversal pulse to the free decaying oscillations. Most of the energy is transferred to the rapidly decaying components at frequencies of 6.6 and 8.1 kHz, which decay over a period of up to 1.5 ms. The spectral components at frequencies of 4.7 and 5.9 kHz have a decay rate an order of magnitude lower.

We obtained temperature dependences of the amplitude of the various spectral components of the oscillations in order to study the conditions for the establishment of these oscillations (Fig. 2a). Each spectral component has a value of $\Delta T$ for which the amplitude is largest at the onset of oscillation. This value of $\Delta T$ corresponds to the point where the period of the oscillations coincides with the half-height width of the polarization reversal pulse ($\Delta\tau$). The duration of the polarization reversal pulse depends on the relation between the rotational viscosity $\gamma_\varphi$, the electric field strength, and the spontaneous polarization:[3]

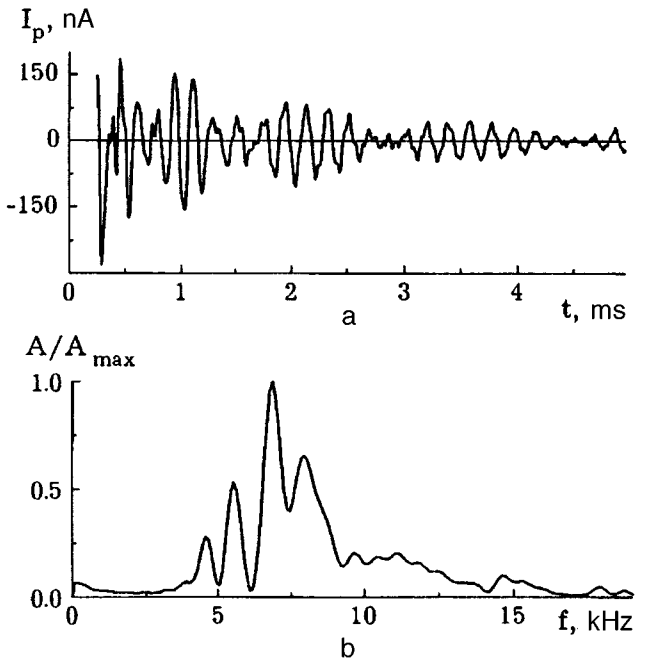


FIG. 1. Time dependence of the polarization reversal current (a) and oscillation spectrum (b) for $\Delta T = 1.7$ °C and $E = 8.75 \times 10^3$ V/cm.

$$\Delta\tau = \frac{1.8\gamma_\varphi}{P_S E}. \tag{1}$$

As $\Delta T$ increases at constant $E$, the rotational viscosity increases monotonically and $\Delta\tau$ increases, causing redistribution of energy from the high-frequency components of the oscillation spectrum to the low-frequency components. In this case, the frequencies of the spectral components remained the same, which suggests that a resonant structure may exist with a set of natural frequencies.

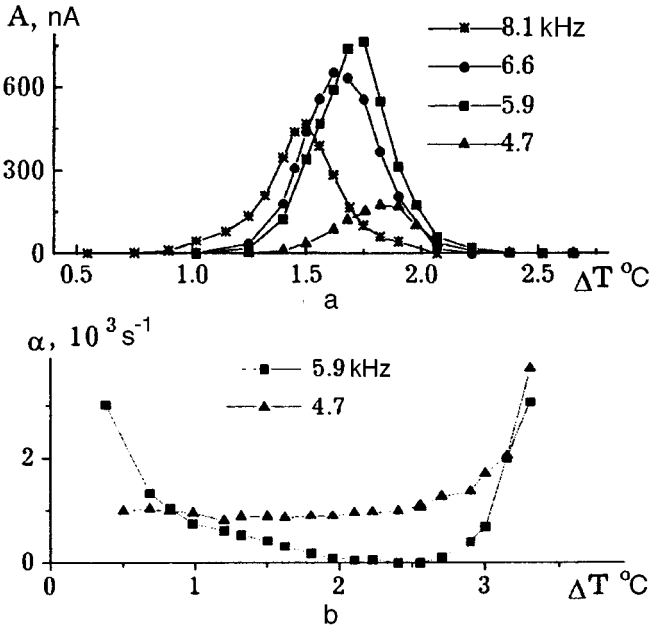


FIG. 2. Temperature dependences of the oscillation amplitude (a) and the damping rate (b) at different frequencies.

The time behavior of the oscillation amplitude is exponentially decaying, and is described by the damping rate $\alpha$, which has different values for the different spectral components. Two oscillation modes may be identified according to the value of $\alpha$, which are probably associated with different structures in the crystal. The first oscillation mode includes rapidly decaying oscillations ($\alpha > 2 \times 10^4$ s$^{-1}$), which have an initial amplitude comparable with the polarization reversal pulse. These are the spectral components with frequencies of 6.6 and 8.1 kHz in Fig. 1b. According to the inertial theory of the dynamic behavior of a liquid crystal, the equation of motion for the director **n** has the form:[4]

$$\sigma \frac{\partial^2\varphi}{\partial t^2} = K \frac{\partial^2\varphi}{\partial x^2} - \gamma_\varphi \frac{\partial\varphi}{\partial t} - P_S E \sim \varphi, \tag{2}$$

where $\sigma$ is the moment of inertia per unit volume, $\varphi$ is the azimuthal angle of the director, and $K$ is the elasticity constant. It is easy to see that the damping rate is related to the viscosity and the moment of inertia as follows:

$$\alpha = \frac{\gamma_\varphi}{2\sigma}. \tag{3}$$

For the first oscillation mode, Eq. (3) yields $\sigma \sim 3 \times 10^{-6}$ g/cm, which corresponds to a structural element having the characteristic size $\sim 20\ \mu$m. Since the diameter of zigzag defects on a chevron structure is 22–24 $\mu$m, it may be postulated that these determine the parameters of the first oscillation mode. The second oscillation mode ($\alpha \sim 10^3$ s$^{-1}$) is not described by Eq. (2), since the density of the moment of inertia, in accordance with Eq. (3), is $\sim 3 \times 10^{-5}$ g/cm, which increases the characteristic size of a structural element by an order of magnitude. Temperature dependences of $\alpha$ were obtained for this oscillation mode. Figure 2b gives the curves of $\alpha(\Delta T)$ for the spectral components at frequencies of 4.7 and 5.9 kHz. Assuming that the oscillation energy is dissipated as heat on account of the viscosity of the crystal, a monotonic increase in the damping rate may be expected with increasing coefficient $\gamma_\varphi$. However, the damping rate decreases near the Sm$A \rightarrow$Sm$C^*$ phase transition and has a minimum for $\Delta T$ around 2.5 °C. This behavior of $\alpha(\Delta T)$ is typical of all spectral components of the second oscillation mode. Components whose decay is determined by the inertial properties of the moving glass substrate are also observed.

In this report, we have confined ourselves to qualitative reasoning. The results of a more detailed and quantitative analysis will be published separately.

The authors are grateful to L. A. Kutulya and V. V. Vashchenko for synthesizing the ferroelectric liquid crystals and chiral additive, and also for valuable discussions during this work.

[1] A. Jakli and L. Bata, Liquid Cryst. **7**, 105 (1990).
[2] M. V. Loseva, E. A. Pozhidaev, A. Z. Rabinovich *et al.*, Itogi Nauki Tekhn. Ser. Fiz. Khim. [in Russian], VINITI, Moscow (1990).
[3] K. Sharp, Ferroelectrics **84**, 119 (1988).
[4] B. J. Edwards, A. N. Beris, and M. Grmela, Mol. Cryst. Liquid. Cryst. **201**, 51 (1991).

Translated by R. M. Durham

# A negative-feedback garnet laser

N. V. Bystrov and S. M. Zakharov

*P. N. Lebedev Physics Institute, Russian Academy of Sciences, Moscow*
(Submitted December 15, 1996)
Pis'ma Zh. Tekh. Fiz. **23**, 86–88 (April 12, 1997)

A reduction in the time taken to achieve cw lasing from milliseconds to microseconds is obtained in an actively mode-locked Nd:YAG laser when weak, slow-response, negative feedback was inserted. The laser is designed to illuminate the photoinjector cathode of an electron accelerator.  [S1063-7850(97)01504-8]

Photoinjectors are being increasingly widely used instead of thermionic cathodes and bunchers in electron accelerators.[1] Electron bunching is achieved by appropriate laser illumination of a photocathode. Depending on the frequency of the accelerating field and the duration of the acceleration cycles, the requirements for the laser vary widely: micropulse length between 1 and 200 ps, pulse repetition rate between 50 MHz and 3 GHz, and train (macropulse) length between a few and hundreds of microseconds. The parameters required for our accelerator[2] were 100 ps, 150 MHz, and $>100$ $\mu$s, respectively. Such long trains can be cut from a continuous series of micropulses generated by a mode-locked, cw-pumped laser. Pulsed quasi-cw pumping is energetically more favorable, but then the duration of the transient processes must be taken into account. Calculations[3] have shown that when initially disordered modes are actively mode-locked, the lasing in a Nd:YAG laser becomes cw within milliseconds, whereas in a single-mode field, this is achieved within microseconds. Mode disorder is especially observed in the spiky structure characteristic of free running in solid-state lasers and before mode locking is implemented it is desirable to achieve nonspiky free running. This condition can be achieved by incorporating passive or active negative feedback. Amplitude feedback is implemented, but the frequency and phase structures of the cavity modes are clearly efficiently influenced. Passive feedback is based on nonlinear effects (conversion to the second harmonic, two-photon absorption), it has an almost instantaneous response, and is effective for short (of the order of 1 $\mu$s) trains.[4,5] However, if the two-photon absorption is accompanied by an appreciable buildup of conduction electrons, the slow-response component may dominate in the response. The response time is governed by the lifetime of the conduction electrons.[5] Active feedback is achieved using electrooptic materials, it usually has a slow response, and is suitable for operation with long trains.

In the laser described, quasi-cw pumping of up to 1.5 ms duration was provided by a uniform artificial line. Its wave impedance (0.5 $\Omega$) was matched with an 800 J flashlamp. The garnet crystal used had a diameter of 0.5 cm and a length of 6 cm. The cavity formed by a 40% plane mirror and a nontransmitting spherical mirror ($R=280$ cm) was tuned to the 150 MHz intermode beat frequency. A thermostatically controlled acoustooptic modulator was supplied with a power of up to 20 W by a 75 MHz pulse generator. The percent modulation was 10%. A KDP electrooptic modulator with a double-pass half-wave voltage of 200 V and a photodiode with a time resolution of 1 $\mu$s and an output signal amplitude of less than 10 V formed a negative feedback loop. This weak feedback was sufficient to alter fundamentally both the nature of the free running and the mode-locked lasing. The spiky structure usually observed for free running (Fig. 1a) completely disappears (Fig. 1b) and the time taken to reach cw lasing under active mode locking is reduced from approximately a millisecond (Fig. 1c) to microseconds (Fig. 1d). Note that the oscilloscope traces in Fig. 1c are remarkably similar to those in Fig. 4 in Ref. 3, in which the cavity tuning precision and the time taken to reach cw lasing were determined from the nature of the oscillations.

The time resolution of the traces in Fig. 1 is inadequate to identify the micropulses. To observe these pulses, the signal from a coaxial photocell was fed directly to the deflection plates of an S1-75 oscilloscope, which were swept by a 75 MHz sinusoidal signal from the same generator as the acoustooptic modulator. Thus, two pulses can be identified in Fig. 2, one formed by the superposition of all even micropulses in the train and the other formed by the superposition of all odd micropulses (some hundreds of thousands of pulses). Although the exact pulse profile cannot be determined because

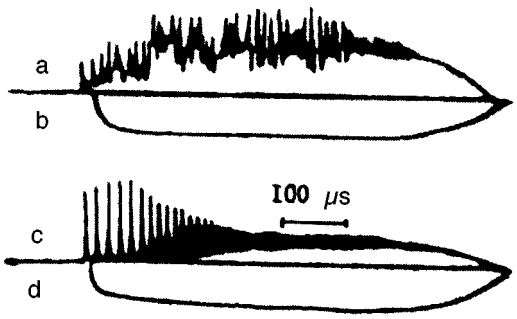


FIG. 1.

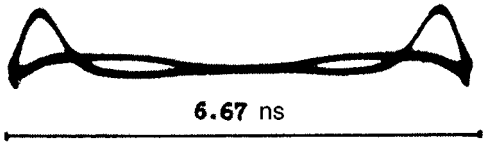


FIG. 2.

of the time resolution of the oscilloscope, the clear superposition of the pulses indicates that they are fairly identical, at least in terms of energy. Note that the duration of illumination of the electron-beam tube was selected so as to cut out the laser pulse tail and avoid the associated blurring of the micropulse image.


[1] C. Travier, Nucl. Instrum. Meth. Phys. Res. A **340**, 25 (1994).
[2] A. Agafonov *et al.*, Nucl. Instrum. Meth. Phys. Res. A **341**, 375 (1994).
[3] D. J. Kuizenga, Opt. Commun. **22**, 156 (1977).
[4] A. V. Babushkin *et al.*, Kvantovaya Elektron. (Moscow) **16**, 2036 (1989) [Sov. J. Quantum Electron. **19**, 1310 (1989)].
[5] S. A. Bakhramov *et al.*, Kvantovaya Elektron. (Moscow) **23**(5), 479 (1996).
[6] K. P. Komarov *et al.*, Kvantovaya Elektron. (Moscow) **13**, 802 (1986) [Sov. J. Quantum Electron. **16**, 520 (1986)].
[7] K. Burneĭka *et al.*, Kvantovaya Elektron. (Moscow) **15**, 1658 (1988) [Sov. J. Quantum Electron. **18**, 1034 (1988)].



Translated by R. M. Durham

# Investigation of inhomogeneous kinetic processes in a gaseous medium excited by multiply charged ions

A. P. Budnik, I. V. Dobrovol'skaya, P. P. D'yachenko, and S. V. Kozel

*A. I. Leĭpunskiĭ Physics and Power Institute, State Science Center of the Russian Federation, Obninsk*
(Submitted November 22, 1996)
Pis'ma Zh. Tekh. Fiz. **23**, 89–94 (April 12, 1997)

The space–time characteristics of track structures in a gaseous medium excited by multiply charged ions have been studied theoretically for the first time and the influence of these structures on the quality of the radiation beam from lasers has been assessed. A model has been developed to describe the diffusion and drift of heavy particles at all stages of the track evolution process. © *1997 American Institute of Physics.* [S1063-7850(97)01604-2]

It has recently been shown[1] that in the active media of gas lasers excited by multiply charged ions (including fission fragments), strong fluctuations in the concentration of some components of the medium may be observed as a result of track effects. Studies of track effects are of scientific and practical importance because the optical microinhomogeneities of the active media, induced by these fluctuations, may determine the quality of the radiation beam produced by the high-energy wide-aperture quantum amplifiers now being developed,[2] whose active media are excited directly by fission fragments.

We shall briefly explain the fundamental reasoning behind this model. Following Ref. 1, we represent the pumping process as a superposition of deterministic continuous and random pulse components. The pulse component simulates the near transits of the multiply charged ions, and the continuous component simulates the distant transits. The near transit of the multiply charged ions is a random process and the time of incidence of the ions near a selected point is described by a Poisson distribution. We shall then investigate the case where most of the track cores[1)] decay sooner than the next multiply charged ion transit closest to the core, and the track sheaths overlap repeatedly within the core lifetime. We only take into account the strong fluctuations induced by the track cores and we neglect the weak ones induced by the sheaths. The evolution of the core of a multiply charged ion track can then be approximated as a process taking place against a background of constant homogeneous pumping. This approximation imposes upper and lower limits on the permissible values of the specific pump power.

Assuming that the ion track is axisymmetric, and neglecting any inhomogeneity along the axis of the track, we shall describe its evolution in the plane perpendicular to the axis of the track using the system:[4,5]

$$\frac{\partial f_0}{\partial t}+\frac{v}{3}\nabla_r\left(-\frac{v}{\nu}\nabla_r f_0+\frac{eE_c}{m_e\nu}\frac{\partial f_0}{\partial v}\right)+\frac{1}{v^2}\frac{\partial}{\partial v}\left(\frac{E^2e^2}{3m^2\nu}v^2\frac{\partial f_0}{\partial v}\right)+S_0(f_0,N_{ik})=0, \tag{1}$$

$$\frac{\partial N_{ik}}{\partial t}=\frac{1}{r}\frac{\partial}{\partial r}\left[r\left(D_{ik}\frac{\partial N_{ik}}{\partial r}-\mu_{ik}EN_{ik}\right)\right]+f_{ik}, \tag{2}$$

$$\frac{1}{r}\frac{\partial}{\partial r}(rE)=-4\pi e(N_e-N_i), \tag{3}$$

where $t$ is the time, $r$ is the distance from the axis of the track, $v$ is the electron velocity, $f_0(r,v,t)$ is the electron velocity distribution function, $N_e(r,t)$ and $N_i(r,t)$ are the electron and total ion concentrations, $N_{ik}(r,t)$ is the concentration of particles of species $k$, $E(r,t)$ is the electric field strength, $e$ and $m$ are the electron charge and mass, $\nu(\varepsilon)$ is the electron–atom collision frequency, $\varepsilon$ is the electron energy, $S_0(f_0,N_{ik})$ is the collision integral, $D_{ik}$ and $\mu_{ik}$ are the diffusion coefficient and mobility of particles of species $k$, and $f_{ik}$ are terms describing the creation and annihilation of particles of species $k$.

The system of equations (1)–(3), with appropriate initial and boundary conditions,[4,5] can be used to simulate the evolution of the track core. Calculations were made for a mixture of helium and cadmium vapor. The helium atom concentration was assumed to be close to the optimum for pumping by a hard ionizer, while the Cd atom concentration was slightly exaggerated ($1.1\times10^{17}$ cm$^{-3}$) to permit applicability of the model. The system of plasma-chemical processes and radiative transitions in He-Cd was constructed using data from Refs. 6 and 7 and was described in detail in Refs. 1 and 8. In total, the model allowed for 19 plasma components (electrons, He and Cd atoms, $He^+$ and $Cd^+$ ions in the ground and excited states, $He_2$ molecules, and $He_2^+$ and $Cd_2^+$ molecular ions), 54 plasma-chemical reactions, and 16 radiative transitions.

A typical result of the mathematical simulation is plotted in Fig. 1. After the transit of the multiply charged ions, the $He^+$ ion concentration undergoes the strongest perturbation. The concentration of the molecular $He_2^+$ ions is less perturbed. It increases initially as a result of the conversion of atomic $He^+$ ions to molecular ions, and then decreases because of charge transfer and diffusion. An increase in the concentration of molecular $He_2^+$ helium ions as a result of charge transfer between the $He_2^+$ ions and cadmium atoms increases the concentration of $Cd^+$ ions in the upper laser level for the $\lambda=441.6$ nm transition. The track core decays as a result of plasma-chemical processes, radiative transitions, and diffusion.

Allowance for the diffusion of heavy particles reduces the amplitude of the fluctuations compared with the calcula-

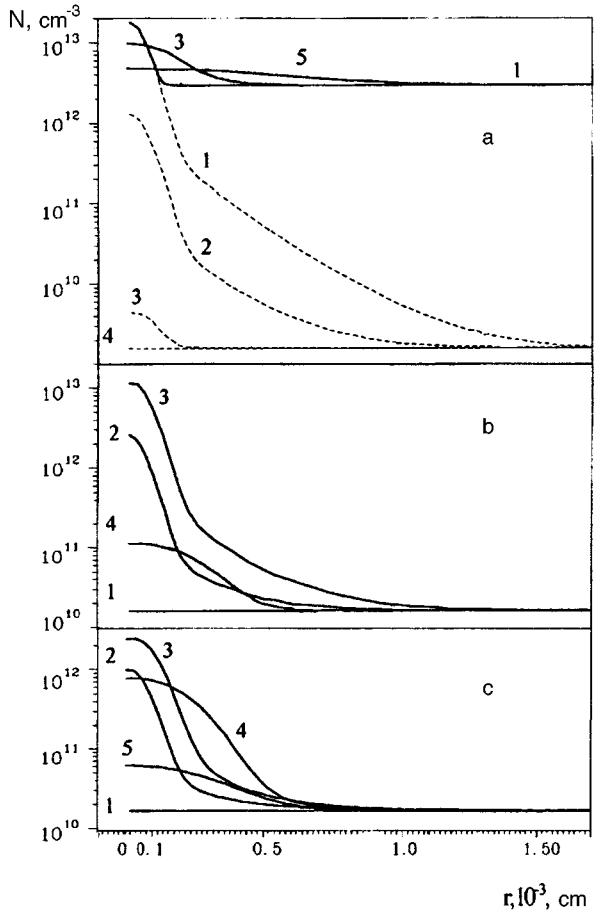


FIG. 1. Concentrations of various ions as a function of distance from the track axis of multiply charged ions in a helium–cadmium plasma at various times after transit of the multiply charged ions: *1* — 200 ps, *2* — 1.3 ns, *3* — 7.8 ns, *4* — 26 ns, and *5* — 57 ns. Ion charge $Z=15$, mass number $A=144$, and kinetic energy $E=80$ MeV. The concentration of helium atoms is $5.86\times10^{19}$ cm$^{-3}$ and the concentration of cadmium atoms is $1.1\times10^{17}$ cm$^{-3}$. The average pump power is 60 W/cm$^3$. *1*(a) — dashed curve — concentration of $He^+$ ions, continuous curve — total ion concentration; *1*(b) —concentration of $He_2^+$ ions; and *1*(c) — $Cd^+$ ions in upper laser level ($\lambda=441.6$ nm).

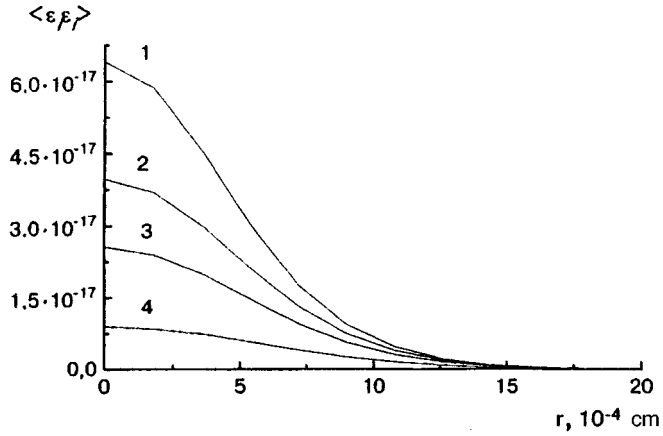


FIG. 2. Correlation function of the imaginary part of the permittivity for transverse pumping by a multiply charged ion beam as a function of the distance $r$ in the plane perpendicular to the direction of beam propagation, for various $t$ (*1* — $t=0$ ns, *2*—$t=40$ ns, *3* — $t=60$ ns, and *4* — $t=100$ ns) for a helium–cadmium medium. The parameters of the medium and the pumping are the same as in Fig. 1.

tions made earlier in Ref. 1. However, the main conclusion reached in Ref. 1, that the parameters of the medium may undergo strong fluctuations, still holds.

The results of the simulation were used to calculate the correlation functions of the complex permittivity (Fig. 2) of a helium-cadmium medium. The correlation functions of the imaginary part of the permittivity are greater than those of the imaginary and real parts, and also greater than those of the real part of the permittivity, and thus are not shown in the figure.

Using the data plotted in Fig. 2, for linear amplification of a plane electromagnetic wave in a statistically uniformly pumped helium–cadmium medium, we can obtain the following relations:

$$\sigma_s^2=\sigma_\chi^2=4.87\times10^{12}\ln M,\quad \langle\theta^2\rangle=1.72\times10^{-13}\ln M,$$

where $\sigma_s(\sigma_\chi)$ is the phase (level) variance of the wave, $\langle\theta^2\rangle$ is the mean square of the angle characterizing the divergence of the radiation;[9] $M$ is the amplification, $M=\exp(\langle g\rangle z)$; $z$ is the distance traveled by the radiation in the medium, and $\langle g\rangle$ is the average linear amplification of the radiation.

Thus, for moderate values of $M$ and a high Cd vapor concentration, the fluctuations of the radiation are small and the angular divergence caused by the track structures only exceeds the diffraction limit when the amplifier aperture is around 1 m. When the Cd vapor concentration is reduced, the influence of track effects on the radiation fluctuations can obviously increase considerably because of the increased lifetime of the cores. However, the overlap of the core tracks must be taken into account for an accurate estimate of this effect.

It has therefore been shown for the first time that the discrete nature of nuclear pumping imposes fundamental constraints on the quality of the radiation beam in lasers whose active media are excited directly by multiply charged ions (especially fission fragments of heavy nuclei).

The authors would like to thank the Russian Fund for Fundamental Research for supporting this work (Grant No. 96-02-17443a).

[1)] In radiation chemistry, the region near the axis of a heavy, charged particle track, in which the energy release density is much higher than that in the surrounding medium, is called the track core, and the track sheath is the region surrounding the core, where the energy release is fairly appreciable.[3] The fluctuations in concentration are highest in the core region.

[1] A. P. Budnik, A. S. Vakulovskiĭ, and I. V. Dobrovol'skaya, Pis'ma Zh. Tekh. Fiz. **20**(23), 67 (1994) [Tech. Phys. Lett. **20**, 964 (1994)].
[2] A. V. Gulevich, P. P. D'yachenko, A. V. Zrodnikov *et al.*, At. Energ. **80**(5), 361 (1996).
[3] A. K. Pikaev, *Modern Radiation Chemistry. Radiolysis of Liquids and Gases* Vol. 2 [in Russian], Moscow (1987).
[4] A. P. Budnik, Yu. V. Sokolov, and A. S. Vakulovskiy, Hyperfine Interact. **88**, 185 (1994).
[5] A. P. Budnik and A. S. Vakulovskiĭ, *Abstracts of Papers Presented at the Second International Conference on Physics of Nuclear-Excited Plasmas and Problems of Nuclear-Pumped Lasers* (LYaN-97), Arzamas-16, 1997, Vol. 1 [in Russian], pp. 75–89.

[6] Yu. B. Dorofeev, E. D. Potetaev, P. P. D'yachenko, and M. Z. Tarasko, Preprint No. FÉI-2311, Obninsk (1993), p. 48.
[7] F. G. Goryunov, V. I. Derzhiev, A. G. Zhidkov *et al.*, Kvantovaya Elektron. (Moscow) **16**, 2039 (1989) [Sov. J. Quantum Electron. **19**, 1312 (1989)].
[8] A. P. Budnik and I. V. Dobrovol'skaya, Preprint No. FÉI-2498, Obninsk (1996), p. 35.
[9] S. M. Rytov, Yu. A. Kravtsov, and V. I. Tatarskiĭ, *Introduction to Statistical Radiophysics, Part II, Random Fields* [in Russian], Moscow (1978).

Translated by R. M. Durham

# ''Bioceramic–titanium nickelide'' functional composites for medicine

V. I. Itin, N. A. Shevchenko, E. N. Korosteleva, A. A. Tukhfatullin, M. Z. Mirgazizov, and V. E. Gyunter

*V. D. Kuznetsov Siberian Physicotechnical Institute, Tomsk State University*
(Submitted December 15, 1996)
Pis'ma Zh. Tekh. Fiz. **23**, 1–6 (April 26, 1997)

''Bioceramic–titanium nickelide'' functional composites are proposed and investigated. It is shown that the incorporation of an alloy (titanium nickelide) possessing superelasticity and shape memory enhances the strength properties of the composite while the porosity through the material needed for the ingrowth of living tissue is maintained. These composites are biocompatible and exhibit a property similar to the superelasticity characteristic of living tissue.
 [S1063-7850(97)01704-7]

From the biomechanical point of view, functional materials for implantation in the body should have properties similar to those of living tissue, i.e., they should possess elasticity and have a stress–strain diagram similar to that of tissue, with its characteristic hysteresis on the loading–unloading diagram. Among existing materials, only alloys with shape memory exhibit similar properties under isothermal conditions.[1] The bioceramics used in medicine do not have these properties, although they do have the advantage of high mechanical strength, nontoxicity, and maximum biocompatibility compared with other materials. A serious disadvantages of bioceramics, particularly porous ones, is their brittleness.

In the present paper we propose a new class of ''bioceramic–titanium nickelide'' composites for medicine. One component (titanium nickelide) of these composites exhibits superelasticity and shape memory, while the other component provides the bioceramic properties.

Porcelain, which is a brittle material widely used in orthopedic stomatology, was selected as the ceramic component. Porcelain is highly brittle because of the contact stresses formed at various phase and grain boundaries, which are considerably greater than the average applied stresses. The contact stresses in the ceramic may undergo relaxation if energy is dissipated in this stress zone through a phase transformation in the titanium nickelide. A change in temperature, or the application of a load, induces a martenistic transformation in the titanium nickelide, which causes efficient relaxation of the stresses in the matrix when the composite is under load, so that the solid component can sustain the applied load.[2]

The samples were prepared using PN55T45 titanium nickelide powder and ''Gamma'' stomatological porcelain mass, which were dried, measured out, and mixed in the following ratios: porcelain + 25 wt.% (13 vol.%) TiNi and porcelain + 50 wt.% (30 vol.%) TiNi. Cylindrical samples 10 mm in diameter and 5–7 mm thick, with an initial porosity of 40–43%, were pressed from the mixture.

The samples were placed in the chamber of an SNVÉ 1.3.1/16ICh electric furnace and were sintered in a vacuum of $133\times10^{-4}$ Pa at various temperatures and times. After sintering, the loss of mass, final porosity, and the linear and bulk changes in the samples were measured, and these data were then used to select the optimum sintering regime.

The chemical compatibility between titanium nickelide and bioceramic was studied using a *Q*-1500 drift indicator (Hungary) and a DRON-1 x-ray diffractometer using cobalt radiation.

Static compression testing was carried out using an Instron 1185 testing device. The true flow stresses, yield strength, and the relative deformation before damage were determined.

In studies of the chemical compatibility between titanium nickelide and stomatological porcelain using thermography and drift indication, the curves reveal no thermal or mass effects up to temperatures of 1120–1130 °C. As a result of further heating, thermal effects do occur but they are small. These results agree with the x ray phase analysis data for the sintered samples, which reveal new, undecipherable lines in addition to those assigned to the components. The intensity of these lines increases with the sintering temperature. We postulate that the chemical interaction between the porcelain mass and oxides on the surface of the titanium nickelide particles results in the formation of new phases, possibly of the spinel type, and an oxide bond is created as well as the mechanical bond (particle coupling).

An investigation of the sintering behavior of mixtures of stomatological porcelain and titanium nickelide powders indicated that the following sintering regime was the optimum for the composite: sintering temperature $T=1150$ °C and sintering time $t=2$ h. This regime ensures fairly high porosity through the sample, combined with good strength properties.

The strength properties of porcelain and composites are presented in Table I. An increase in the density of the samples and the titanium nickelide content in the composite is accompanied by an increase in the true flow stresses, the yield strength, and the deformation before fracture.

Three types of load diagram are obtained for composites sintered under different conditions. As well as load diagrams with a normal smooth profile (Fig. 1, curve *1*), for composites having different compositions, porosities, or deformation rates, we observed irregular stress fluctuations on the stress–strain curves (Fig. 1, curve *2*) or elongated sections (steps) with very different rates of change in stress with increasing

TABLE I. Strength properties of sintered porcelain and porcelain–titanium nickelide composites.

| Material | Final porosity, % | Compressive, yield strength, MPa | Relative deformation before damage, % |
|---|---|---|---|
| Porcelain | 47 | 19 | 3.1 |
| Porcelain–25 wt.%TiNi | 45 | 39 | 3.0 |
| Porcelain–50 wt.%TiNi | 41 | 106 | 5.1 |
| Porcelain–25 wt.%TiNi* | 25 | 500 | 20.1 |

*The samples were prepared by a pressing–sintering–grinding–pressing–sintering process.

strain (Fig. 1, curve *3*). Moreover, the amplitude of these irregular fluctuations varied randomly.

These irregular stress fluctuations in highly porous materials are caused by processes, which, according to the classification put forward by V. I. Vladimirov,[3] develop on a structural level with a characteristic size of $20-200\mu$m and are determined by the distribution, size, and morphology of the pores, and by the chemical composition of the contact zone of the powder particles.[4] The main type of fracture mechanism involves the formation and evolution of microscopic cracks in regions containing pores and interparticle necks. Fracture is also promoted by microcracks in the ceramic component, which are formed during pressing and are inherited after sintering. Merging of microcracks to form a main crack under high stressing leads to fracture of the sample.

The step-profile load diagrams correspond to the level at which independent macroscopic cracks are formed,[3] causing fracture in various parts of the sample. After fracture has occurred at the weakest points, where the stresses have reached the yield strength, the stresses are redistributed. Regions which have not undergone fracture are additionally loaded, and the deformation continues to increase. Thus an increase in the deformation of the porous composite is caused by the sequential fracture of various parts of the material.

Figure 2 shows a typical loading–unloading diagram for a porous sample of porcelain–50 wt.% TiNi composite. The loading and subsequent unloading curves do not match, but form a loop. It has been established that the elastic recovery of the volume of porous compressed samples of superelastic titanium nickelide powder is caused by the breaking of interparticle contacts and is determined by the strength of the briquet, which depends on the porosity and on the contact coupling forces.[5] Weakening these forces by adding other components, such as finely disperse tungsten or silicon carbide, to the titanium nickelide powder appreciably enhances the elastic effect, since strong like-contacts between titanium and nickel are replaced by unlike ones.[5] Since the elastic effect decreases as the titanium nickelide content in the compact is reduced, the concentration dependence of the elastic recovery of the volume usually has an extremum.[5]

In a porcelain–titanium nickelide composite, the components interact weakly, and after sintering the contacts between the ceramic and metallic components are weakened. Under loading, these contacts are the main ones to break and the elastic recovery of the volume increases. As a result, the deformation is reversible and the composite exhibits properties similar to superelasticity.

The biocompatibility of this stomatological porcelain–titanium nickelide composite was studied by a histological method, by evaluating the reaction of rat tissue to samples of the composite (test group) and porcelain (control) implanted

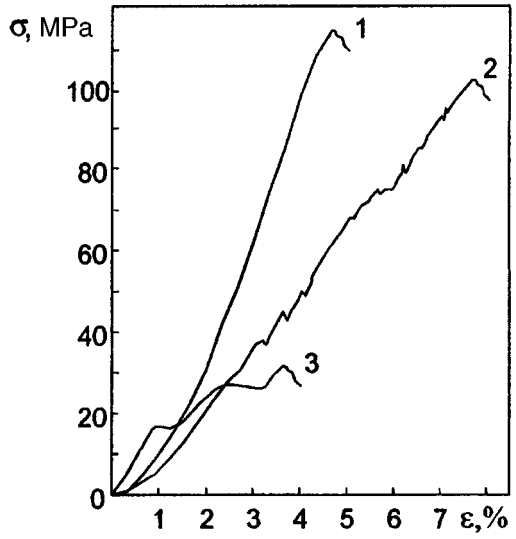


FIG. 1. Stress–strain diagram of porous composites: *1* — porcelain–50 wt.% TiNi, $\eta_{con}=35\%$, $V_{def}=0.5$ mm/min; *2* — porcelain–50 wt.% TiNi, $\eta_{con}=35\%$, $V_{def}=0.1$ mm/min; *3* — porcelain–25 wt.% TiNi, $\eta_{con}=30\%$, $V_{def}=0.5-0.6$ mm/min.

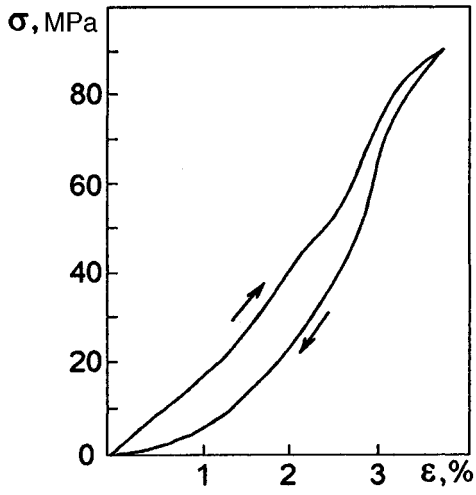


FIG. 2. Stress–strain diagram of porous composite porcelain–50 wt.% TiNi, $\eta_{con}=35\%$, $T_{sin}=1150$ °C, and $t=2$ h.

beneath the skin of the anterior abdominal wall. In both cases, the nature of the tissue reactions, their incidence, and the characteristics of the cellular changes were identical. Thus, bioceramic–titanium nickelide composites are biocompatible.

These investigations have demonstrated that bioceramic–titanium nickelide porous permeable composites are biologically compatible with living tissue, they possess properties similar to superelasticity, and may be used in medicine.

[1] V. É. Gyunter, V. I. Itin, L. A. Monasevich *et al.*, *Shape Memory Effects and Their Application in Medicine* [in Russian], Nauka, Novosibirsk (1992).
[2] S. N. Kul'kov, T. M. Poletika, A. Yu. Chukhlomin *et al.*, Porosh. Metall. No. 8, 88 (1984).
[3] V. I. Vladimirov, *The Physical Nature of Fracture of Metals* [in Russian] (Metallurgiya, Moscow, 1984).
[4] Yu. V. Mil'man, A. M. Leksovskiĭ, and R. K. Ivashchenko, Porosh. Metall. No. 1–2, 77 (1994).
[5] S. M. Solonin, I. F. Martynova, V. V. Skorokhod *et al.*, Porosh. Metall. No. 9, 14 (1986).

Translated by R. M. Durham

# Application of statistical methods to solve global reconstruction problems

A. N. Pavlov, N. B. Yanson, and V. S. Anishchenko

*N. G. Chernyshevskiĭ State University, Saratov*
(Submitted December 10, 1996)
Pis'ma Zh. Tekh. Fiz. **23**, 7–13 (April 26, 1997)

A solution of the problem of reconstructing a mathematical model using statistical methods to specify the evolution operator is optimized. It is shown that this procedure can be used for modeling with short time series, so that the metric and dynamic characteristics of an attractor can be determined with a knowledge of the reconstructed model equations. Direct methods of analyzing scalar time series are less effective in this situation. © *1997 American Institute of Physics.* [S1063-7850(97)01804-1]

One method of mathematical modeling is the global reconstruction of dynamic systems, i.e., the reconstruction of the evolution equations of a system using experimental time series. The concept of reconstruction is primarily linked with Packard[1] and Takens,[2] who demonstrated and verified mathematically the feasibility of reconstructing the phase portrait of an attractor in terms of the one-dimensional realization of some process $a(t)$, discretized with the step $\Delta t$, i.e., using the time series $a_i=a(i\Delta t)$. In 1986, Ref. 3 was published, in which the authors described an algorithm to establish correspondence between a real signal and a mathematical model in the form of a system of ordinary differential equations.

The concept of this algorithm is broadly as follows. Defining dynamic systems involves specifying a set of quantities, that uniquely determine the state, and specifying the evolution operator. Defining in this way presupposes the presence of two stages in the reconstruction of the mathematical model — reconstruction of the phase coordinates of the vector of state, and writing the specific form of the evolution equations.

The conventional approach to the reconstruction of a phase trajectory involves using the Packard–Takens delay method. However, when a mathematical model is to be obtained, most researchers prefer to use a method of successive differentiation, since this can yield a simpler model,[3–6] specifically:

$$\dot{x}_1=x_2, \quad \dot{x}_2=x_3, \ldots, \dot{x}_n=f(x_1,x_2,\ldots,x_n), \tag{1}$$

where $f$ is a nonlinear function, defined *a priori*, which, in the simplest case, may be represented by a polynomial of some degree $\nu$:

$$f(\mathbf{x})=\sum_{l_1,l_2,\ldots,l_n=0}^{\nu} C_{l_1,l_2,\ldots,l_n}\prod_{i=1}^{n} x_i^{l_i}, \quad \sum_{i=1}^{n} l_i \leqslant \nu. \tag{2}$$

In the global reconstruction algorithm, $K$ unknown coefficients of the polynomial $C_{l_1,l_2,\ldots,l_n}$ are approximated by the least squares method, i.e., a system of $N$ linear algebraic equations is solved with $K$ unknowns, where $N$ is the number of points of the initial time series, $K=(n+\nu)!/(n!\nu!)$. As a result, we obtain a model system of first-order ordinary differential equations. However, in practical applications of the algorithm, $C_{l_1,l_2,\ldots,l_n}$ will depend on the choice of parameters of the numerical system ($n,\nu,N$, and so forth), so that a more rigorous approach to the problem will involve studying the dependences of $C_{l_1,l_2,\ldots,l_n}$ on the parameters. In the present paper, we propose to consider $C_{l_1,l_2,\ldots,l_n}(N)$.

Thus the aim of the present paper is to study the feasibility of obtaining a rough mathematical model whose coefficients are selected by statistical methods. We also propose to show that this procedure can specify the evolution operator even when very short time series are used, so that the metric and dynamic characteristics of an attractor can be determined fairly accurately by using the reconstructed model equations. Direct methods of calculation using scalar time series are less effective under these conditions.

The global reconstruction algorithm has recently begun to be applied to realizations of processes of biological origin. Specifically, the reconstruction of a mathematical model for a single period of an electrocardiogram of a healthy person was analyzed in Ref. 7. An arbitrarily selected section, containing $P,Q,R,S$, and $T$ waves and a pause, was repeated many times to obtain a sufficiently long periodic time series (Fig. 1a). Integrals with variable upper limits taken from the initial time series were selected as the first two coordinates of the vector of state. A similar procedure for definition of the state vector may be implemented as follows. If $a(t)$ is the initial time series, we calculate

$$b(t)=\int_0^t a(\tau)d\tau, \quad c(t)=\int_0^t b(t)d\tau. \tag{3}$$

Then, $c(t)$ is used as the initial realization. The method of successive differentiation is then used to reconstruct the remaining coordinates of the state vector in phase space, which thus has the following form:

$$\mathbf{x}_i=\{c_i, dc_i/dt, \ldots, d^{n-1}c_i/dt^{n-1}\}=\{x_1,x_2,\ldots,x_n\}, \tag{4}$$

where $c_i=c(i\Delta t)$, $i$ is the number of the point, and $\Delta t$ is the sampling time. Clearly, $d^2c_i/dt^2$ is the initial signal $a(i\Delta t)$. Since the coordinates of the state vector are derivatives of the signal $c(t)$, the reconstructed mathematical model has the form (1).

We fix all the parameters of the global reconstruction algorithm apart from $N$, and we approximate the coefficients $C_{l_1,l_2,\ldots,l_n}$ of the function $f$ by varying $N$. We construct the

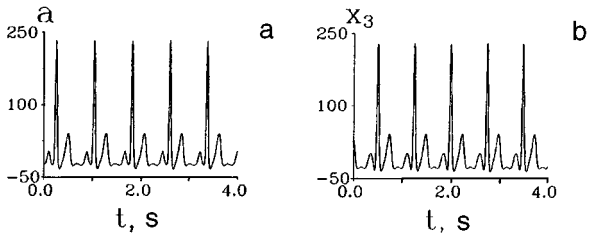


FIG. 1. a — Initial signal obtained by repetition of a single ECG period; b — solution of a model system of equations (the values $C_{l_1,l_2,l_3,l_4}$ corresponding to the maximum of the probability density distribution, calculated using the dependence of each coefficient on the parameter $N$, were used for the specific form of the evolution operator).

dependences $C_{l_i,l_2,\ldots,l_n}(N)$ and calculate the probability distribution density for each of these. For the specific form of the evolution operator, we select those values of $C_{l_i,l_2,\ldots,l_n}$ which correspond to the maximum probability density.

By integrating the model system thus obtained, we can confirm (Fig.1b) that the maximum of the probability density corresponds to an approximate solution which highly accurately reproduces the initial signal. It should also be noted that variation of $C_{l_1,l_2,\ldots,l_n}$ over a fairly wide range relative to the probability maximum does not impair the dynamic regime.

A characteristic feature of the global reconstruction algorithm where statistical methods are used to specify the evolution equations, is that the modeling can be performed over a fairly short realization. We shall illustrate this using specific examples.

If the global reconstruction algorithm is applied to the periodic signal obtained by integrating the equations for a Van der Pol oscillator ($n=2$, $\nu=3$), the curves $C_{l_1,l_2,\ldots,l_n}(N)$ for most coefficients have the form shown in Fig. 2a, i.e., they exhibit a clear tendency to converge with increasing $N$. If an accuracy of up to 1–2% is convenient when determining the coefficient,[1)] we can confine ourselves to a realization of the order of $M=10$ periods of the initial signal (or less depending on the sampling time $\Delta t$).[2)]

Similar results are also obtained for other periodic realizations, especially for the example of the process of biological origin described above ($n=4$, $\nu=3$), where $M\approx 20$ periods of the initial signal were required to achieve the same accuracy (1–2%).

We shall now analyze a chaotic signal obtained by integrating a system of Rössler equations:

$$\dot{x}=-(y+z), \quad \dot{y}=x+ay, \quad \dot{z}=b+z(x-c). \tag{5}$$

The realization of the coordinate $y$ for the values of the parameters $a=0.15$, $b=0.2$, and $c=10$ was used as the initial realization (Fig. 2c). For this example, one can only talk about an arbitrary oscillation period (corresponding to the base frequency of the spectrum). An average of $M\approx 22$ of these periods ($N\approx 2200$, $n=3$, $\nu=2$) is required to determine $C_{l_1,l_2,\ldots,l_n}$ with an accuracy of 1–2%.

Figure 2b shows a typical curve of $C_{l_1,l_2,\ldots,l_n}(N)$ for this example. It can be seen from Fig. 2d that a solution of

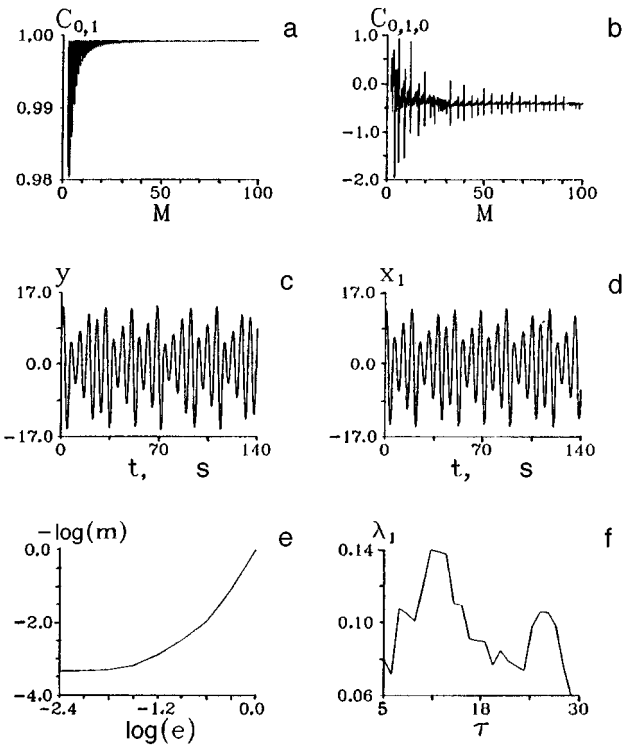


FIG. 2. a, b — Typical dependences of the approximation coefficients of the polynomials on the number of periods of the initial signal for a Van der Pol generator and a Rössler system in the chaotic regime, respectively (in the second case, an arbitrary oscillation period corresponding to the base frequency in the spectrum is considered); c, d — initial signal (curve of $y(t)$ obtained by integrating the system (5)) and solution of the reconstructed model system of equations, respectively; e — curve of $\log(m)$ versus $\log(e)$, which can be used to estimate the Hausdorff dimension ($e$ is the dimension of a dividing cell in the phase space and $m$ is the number of filled cells); f — oldest Lyapunov characteristic exponent, calculated by the method described in Ref. 9, versus the delay time $\tau$, measured in units of $\Delta t$ (the Packard–Takens method for reconstruction of the attractor phase portrait was used to calculate $\lambda_1$).

the mathematical model, reconstructed using 2200 points, sufficiently accurately reproduces the initial dynamic regime. Thus, by using the model, we can determine the metric and dynamic characteristics of the attractor, which is an extremely difficult task for such a short scalar time series.

In practice, calculations of the Hausdorff dimension[8] using the slope of the linear section of the graph (Fig. 2e) yield highly inaccurate estimates of the dimension.[3)] Calculations of the oldest Lyapunov characteristic exponent using a method described in Ref. 9 can yield a value close to the true value for this particular example, but these results must be treated with extreme caution because of the absence of any ''shelf'' on the curve (Fig. 2f).

If we have the reconstructed mathematical model at our disposal, we can calculate these characteristics with a high degree of accuracy. In particular, the spectrum of the characteristic exponent ($\lambda_1=0.07$, $\lambda_2=0$, $\lambda_3=-10.22$) calculated using the reconstructed dynamic system by the Benettin method,[10] has values close to the true ones ($\lambda_1=0.09$, $\lambda_2=0$, $\lambda_3=-10$), so that the information dimension of the attractor can also be estimated by using the Kaplan–Yorke formula[10] for the Lyapunov dimension $d_L$. Using the spec-

trum of the model system gave $D_L = 2.007$, whereas the accurate value of the dimension is $d_L = 2.01$ (Ref. 9).

To conclude, we have studied dependences of specific values of $C_{l_1,l_2,\ldots,l_n}$ on the choice of the parameter $N$. We have shown that when statistical methods are applied to the problem of global reconstruction, assuming that the general form of the evolution equations has been successfully selected *a priori*, it is possible to obtain an approximate model and to reconstruct the most probable evolution operator. This procedure allows the modeling to be confined to a fairly short scalar time series, whereas if the modeling is performed neglecting the statistics of the coefficients, the accuracy of the determination of $C_{l_1,l_2,\ldots,l_n}$ may be above our desired accuracy of 1–2%, even for realizations more than 100 periods in length (with the same sampling), for various values of the numerical parameters. Thus, although the application of statistical methods frequently requires fairly lengthy calculations, there is no doubt that this approach has an advantage.

[1)]In this case, the accuracy of determining the coefficient is understood to mean the ratio $|C_{l_1,l_2,\ldots,l_n}(N) - C^0_{l_1,l_2,\ldots,l_n}|/|C^0_{l_1,\ldots,l_n}|$, where $C_{l_1,l_2,\ldots,l_n}(N)$ is the instantaneous value of the coefficient and $C^0_{l_1,l_2,\ldots,l_n}$ is the corresponding maximum of the probability density.

[2)]For this particular example, we used a sample of approximately 100 points per period.

[3)]The same is also observed for other generalized dimensions, especially the correlation dimension.


[1] N. H. Packard, J. P. Crutchfield, J. D. Farmer, and R. S. Shaw, Phys. Rev. Lett. **45**, 712 (1980).
[2] F. Takens, *Dynamical Systems and Turbulence*, Springer Lecture Notes in Mathematics (Springer-Verlag, Berlin, 1981), pp. 366–381.
[3] J. Cremers and A. Hübler, Z. Naturforsch. A **42**, 797 (1986).
[4] G. Gouesbet and C. Letellier, Phys. Rev. E **49**, 4955 (1994).
[5] D. A. Gribkov, V. V. Gribkova, and Yu. A. Kravtsov, Radiotekh. Elektron. No. 2, 269 (1994).
[6] N. B. Janson and V. S. Anishchenko, in *Chaotic, Fractal and Nonlinear Signal Processing*, edited by R. A. Katz, Mystic, CT, 1995, pp. 688–708.
[7] N. B. Yanson, A. N. Pavlov, A. G. Balanov, and V. S. Anishchenko, Pis'ma Zh. Tekh. Fiz. **22**(16), 57 (1996) [Tech. Phys. Lett. **16**, 669 (1996)].
[8] P. Grassberger and I. Procaccia, Phys. Rev. Lett. **50**, 346 (1983).
[9] A. Wolf, J. B. Swift, H. L. Swinney, and J. A. Vastano, Physica D **16**, 285 (1985).
[10] G. Benettin, M. Galdani, A. Giorgilli, and J.-M. Strelcun, Meccanica **15**, 9 (1980).
[11] J. L. Kaplan and J. A. Yorke, Lecture Notes Math. **730**, 204 (1979).


Translated by R. M. Durham

# Mutual synchronization of switching processes in coupled Lorenz systems

V. S. Anishchenko, A. N. Sil'chenko, and I. A. Khovanov

*Saratov State University*
(Submitted December 23, 1996)
Pis'ma Zh. Tekh. Fiz. **23**, 14–19 (April 26, 1997)

A numerical analysis is made of the synchronization of the mean switching frequencies in two symmetrically coupled Lorenz systems functioning in a chaotic regime. The observed effect on the coupling–mismatch parameter plane corresponds to a region of synchronization of the switching processes, within which the mean switching frequencies coincide to a given accuracy. © *1997 American Institute of Physics.* [S1063-7850(97)01904-6]

One mechanism for the self-organization of nonlinear oscillatory systems is synchronization, as a result of which the interacting subsystems demonstrate a tendency to oscillate at equal (or rationally coupled) frequencies.[1] A ''frequency locking'' effect occurs in weak interactions, whereas one of the natural frequencies is suppressed in fairly strong interactions. It has been established in physical and numerical experiments that mutual and forced synchronization effects also occur in the interaction of chaotic and stochastic systems.

A stochastic synchronization effect via locking of the mean switching frequency by an external excitation signal was observed in studies of a bistable system driven by an external periodic force and white noise.[2] Stochastic synchronization of switching processes was observed in Ref. 3 in an analysis of two symmetrically coupled bistable systems driven by statistically independent noise sources.

In Refs. 5 and 6, the classical concept of the synchronization of dynamic systems was generalized to the case of systems having a saddle-focus chaotic attractor, whose spectrum contains a clearly discernible base frequency. Forced synchronization of switching processes induced by ''chaos–chaos'' intermittence in a Chua circuit was analyzed in Ref. 7.

With this in mind, it seems quite logical to analyze the synchronization process of two symmetrically coupled bistable systems, in which switching is not induced by the action of noise sources, as in Ref. 3, but by the internal dynamics of the subsystems themselves. We selected a Lorenz system[8] as a subsystem possessing these properties.

The dynamic system studied has the form

$$\begin{aligned}
\dot{x}_1&=\sigma(y_1-z_1)+\gamma(x_2-x_1),\\
\dot{y}_1&=r_1x_1-x_1z_1-y_1,\\
\dot{z}_1&=x_1y_1-z_1b,\\
\dot{x}_2&=\sigma(y_2-x_2)+\gamma(x_1-x_2),\\
\dot{y}_2&=r_2x_2-x_2z_2-y_2,\\
\dot{z}_2&=x_2y_2-z_2b.
\end{aligned}\tag{1}$$

It can be seen from Eq. (1) that the interacting subsystems are mismatched in terms of the parameter $r$. The parameters of the subsystems are such ($\sigma=10$, $r_1=28$, $r_2=28.8$, and $b=8/3$) that a Lorenz attractor exists in each of them. In accordance with the ''two states'' method,[9] introducing the quantities

$$x_1'=\begin{cases}+1, & x_1>0\\ -1, & x_1<0,\end{cases}\qquad x_2'=\begin{cases}+1, & x_2>0\\ -1, & x_2<0,\end{cases}$$

we shall analyze this model as a system of two symmetrically coupled chaotic bistable systems. The switching process in the subsystems may be characterized by the distribution density of the residence times $p(\tau)$ in one of the states, denoted by us as $+1$ and $-1$. By analogy with a stochastic bistable system, we can introduce the mean transition frequency $\langle f\rangle$, having determined the switching period as the first moment of a steady-state random process with the distribution density $p(\tau)$:

$$\langle T\rangle=\lim_{T\to\infty}1/T\int_0^\infty \tau p(\tau)d\tau,\quad \langle f\rangle=1/\langle T\rangle.$$

The results of calculations of the switching frequencies $\langle f_1\rangle$ and $\langle f_2\rangle$ as a function of the degree of coupling are plotted in Fig. 1a. For $\gamma=0$ the switching frequencies of the subsystems are nonidentical, because the values of the parameters $r_1$ and $r_2$ differ. At this point, it is appropriate to note that increasing the parameter $r$ of a subsystem causes a slow monotonic increase in its mean switching frequency. With increasing coupling, the mean switching frequencies $\langle f_1\rangle$ and $\langle f_2\rangle$ initially decrease, reaching a minimum for $\gamma\cong 2.8$. A further increase in coupling causes these frequencies to increase gradually and converge, and at $\gamma=6$ the switching frequencies coincide. It should be noted that the steady-state mean switching frequency in the synchronization regime ($\gamma>6$) differs from the initial values of $\langle f_1\rangle$ and $\langle f_2\rangle$ for $\gamma=0$.

By analogy with the classical theory of oscillations, this convergence of the switching frequencies in the subsystems with increasing coupling is logically described as the mutual synchronization of the mean switching frequencies of symmetrically coupled bistable systems.

The increase in the degree of correlation of the switching processes in the subsystems may be illustrated by means of the coherence function:

$$\Gamma^2(\omega)=\frac{|S_{x_1x_2}(\omega)|}{S_{x_1}(\omega)S_{x_2}(\omega)},$$

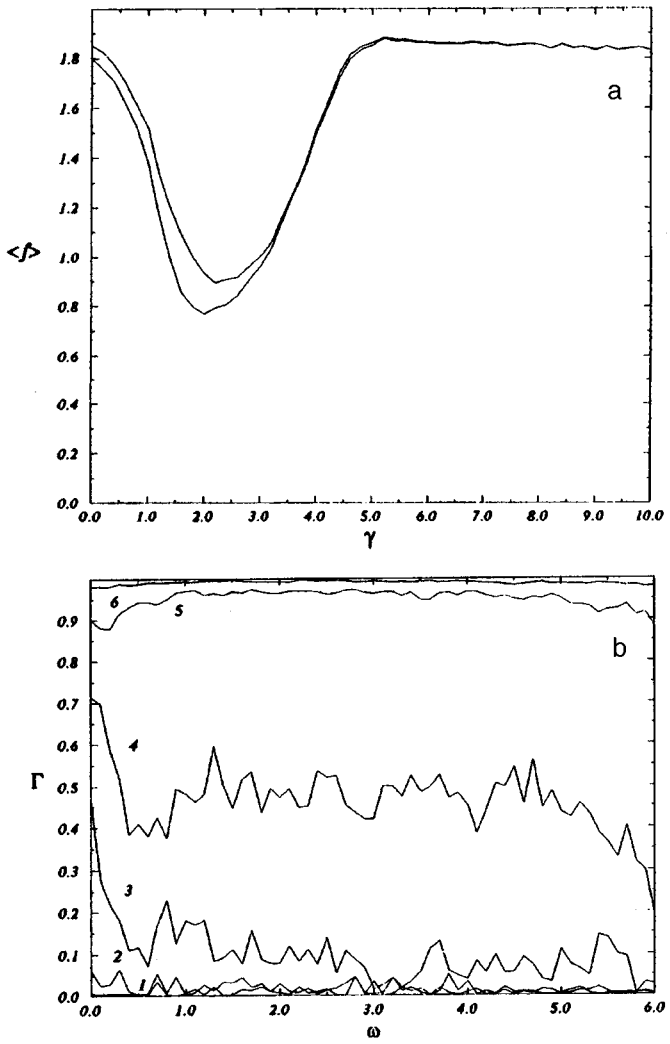


FIG. 1. a — Mean switching frequencies versus coupling; b — coherence function for various degrees of coupling.

where $S_{x_1x_2}(\omega)$ is the mutual power spectrum of the processes $x_1(t)$ and $x_2(t)$, and $S_{x_1}(\omega)$ and $S_{x_2}(\omega)$ are the spectra of the processes $x_1(t)$ and $x_2(t)$, respectively. It is easy to see that the coherence function varies between 0 and 1. The fact that $\Gamma$ tends to unity in a certain frequency range implies an increase in coherence. The results of the calculations are plotted in Fig. 1b. For zero coupling we find $\Gamma=0$ (see curve *1* in Fig. 1b). A gradual increase in the coupling increases the coherence function in the low-frequency range, which indicates an enhanced degree of correlation between the switching processes in the subsystems (curves *2, 3, 4, 5,* and *6* were calculated for $\gamma=0.5, 1.5, 3.0, 4.5,$ and 5.5, respectively).

The qualitative changes in the dynamics of the system are caused by bifurcations which take place as the coupling is increased, i.e., symmetry-loss bifurcations, as a result of which an attracting family of saddle cycles is formed in the neighborhood of a symmetric halfspace, as well as Hopf bifurcations of equilibrium states. A detailed analysis of the bifurcation mechanism of the effect is outside the scope of the present article.

It is known from the classical theory of oscillations that

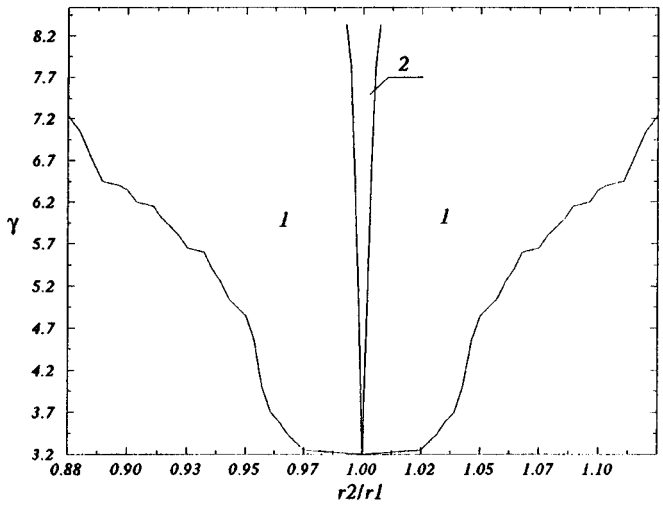


FIG. 2. Regions of switching synchronization — region *1* and total synchronization — region *2* on the mismatch–coupling parameter plane.

the principal characteristic feature of the synchronization effect is the existence of a region of coherent behavior of the subsystems on the coupling–mismatch parameter space. By analogy with the classical case, it seems quite logical to envisage the construction of a similar region for the case where the subsystem is a bistable system with switching processes induced by its complex internal dynamics. The parameter $r$ was selected as the parameter ''controlling'' the mean switching frequency in the subsystem. In this case, we take the mismatch of the systems to be $p=r_1/r_2$, where $r_1$ and $r_2$ are the parameters of the first and second subsystems, respectively.

Since the time scales characterizing the subsystems in this case are associated with random quantities (these being the mean switching frequencies), we cannot strictly talk of the construction of a clearly defined region on the mismatch–coupling parameter space. In our view, it is more reasonable to envisage the construction of a region within which the switching processes are more coherent (the mean frequencies $\langle f_1\rangle$ and $\langle f_2\rangle$ coincide to a given accuracy) than those outside this region. The results are plotted in Fig. 2. The mean switching frequencies $\langle f_1\rangle$ and $\langle f_2\rangle$ are synchronized within region *1*, differing by 0.5%. Region *2* is the region of total synchronization of the subsystems ($x_1=x_2$, $y_1=y_2$, $z_1=z_2$). It can be seen from the figure that region *2* lies within region *1*, i.e., synchronization of the switching processes in the subsystems with varying coupling precedes the total synchronization of the chaotic oscillations of the subsystems.

This work was partially financed by Russian Fund for Fundamental Natural Science (Grant 95-0-8.3-66).

[1] I. I. Blekhman, *Synchronization of Dynamical Systems* [in Russian], Nauka, Moscow (1971).
[2] B. Shulgin, A. Neiman, and V. Anishchenko, Phys. Rev. Lett. **75**, 4157 (1995).
[3] A. B. Neiman, Phys. Rev. E **49**, 3484 (1994).
[4] H. A. Kramers, Physica **7**, 28 (1940).
[5] V. S. Anishchenko, T. E. Vadivasova, D. É. Postnov, and M. A. Safonov, Radiotekh. Elektron. **36**, 338 (1991).

[6] V. S. Anishchenko, *Dynamical Chaos – Models and Experiments* (World Scientific, Singapore, 1995).
[7] I. A. Khovanov and V. S. Anishchenko, Radiotekh. Elektron. *in press* (1997).
[8] E. N. Lorenz, J. Atmos. Sci. **20**, 130 (1963).
[9] V. S. Anishchenko, M. A. Safonova and L. O. Chua, J. Circuits Systems Computers **3**, 553 (1993).

Translated by R. M. Durham

# Time modulation of the input signal during recording of holograms on hydrogenated amorphous silicon–liquid crystal structures

A. N. Chaĭka, N. L. Ivanova, and A. P. Onokhov

*S. I. Vavilov State Optical Institute, All-Russian Scientific Center, St. Petersburg*
(Submitted December 18, 1996)
Pis'ma Zh. Tekh. Fiz. **23**, 20–25 (April 26, 1997)

It is shown that the resolution and diffraction efficiency of $p-i-na-$Si:H−liquid crystal structures can be improved without causing any deterioration in the other parameters, by introducing amplitude modulation of the recording light beam synchronous with the supply voltage. © *1997 American Institute of Physics.* [S1063-7850(97)02004-1]

A prerequisite for the development of various architectures of optical neuron networks is the rapid recording of holograms, with the capacity for erasure and subsequent rerecording within short time intervals.[1,2] The feasibility of developing a holographic recording element with a nonlinear transfer characteristic is also an interesting proposition. With the success achieved in the development of optically addressed light modulators based on hydrogenated amorphous silicon ($a$-Si:H) with a modulating liquid-crystal layer, one can now obtain a good combination of the principal parameters — resolution, speed, and sensitivity — required for reversible recording of holograms in real time. By incorporating a photoconducting layer in the form of a $p$-$i$-$n$ diode made of $a$-Si:H, the speed of the modulator can be improved without causing any deterioration in its other parameters.[3] The aim of the present paper is to further improve the combination of parameters of optically addressed light modulators by increasing the spatial resolution and the diffraction efficiency. This has been accomplished by amplitude modulation of the recording light beam.

To study hologram recording process on liquid-crystal structures, the interference pattern between two plane waves of equal intensity ($I_1-I_2$) was formed in the plane of the photoconductor–liquid crystal interface using He–Ne laser radiation ($\lambda_W=0.633$ $\mu$m). In this case, the spatial frequency of the pattern is determined by the angle of convergence of the interfering beams. The recorded holograms were read out using cw radiation from a semiconductor injection laser ($\lambda_R=0.845$ $\mu$m) and the first diffraction order was recorded with a photomultiplier. When a time-constant interference pattern reaches the $p$-$i$-$n$ $a$-Si:H−nematic liquid crystal structure, the leading edge of the positive supply pulse erases the previously recorded information and the incoming trailing edge triggers the visualization of the latent image formed by the photogenerated carriers during exposure of the structure (Fig. 1a). Under these conditions, an important part is played by the carrier diffusion along the boundary of the $n$-layer and the liquid crystal, which leads to erosion of the potential relief and consequently reduces the percent modulation of the pattern formed in the liquid-crystal layer. This is observed as a deterioration in the resolution and the diffraction efficiency of the holographic recording element. Amplitude time-modulation of the recording light beam was introduced with the aim of utilizing more fully the capabilities offered by the $p$-$i$-$n$ $a$-Si:H–liquid crystal structure. For this purpose we developed a liquid-crystal switch utilizing a ferroelectric liquid crystal, which operated on the basis of the Clark–Lagervoll effect, giving an on/off time of less than 30 $\mu$s. The switch, together with a polarizing element, incorpo-

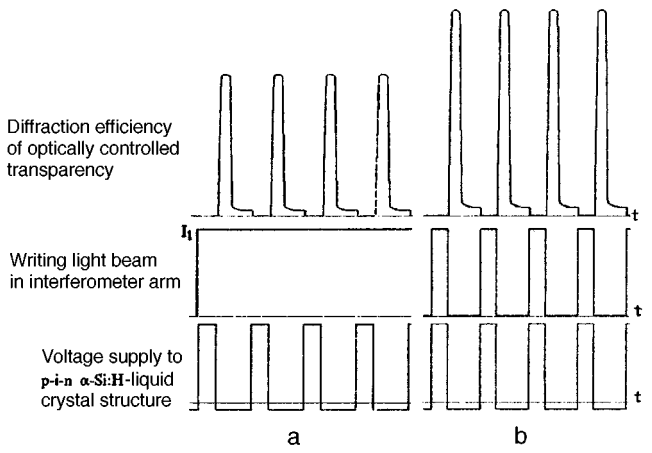


FIG. 1. Response of a $p$-$i$-$n$ $a$-Si:H−liquid crystal structure with a time-constant input signal (a) and with amplitude modulation (b).

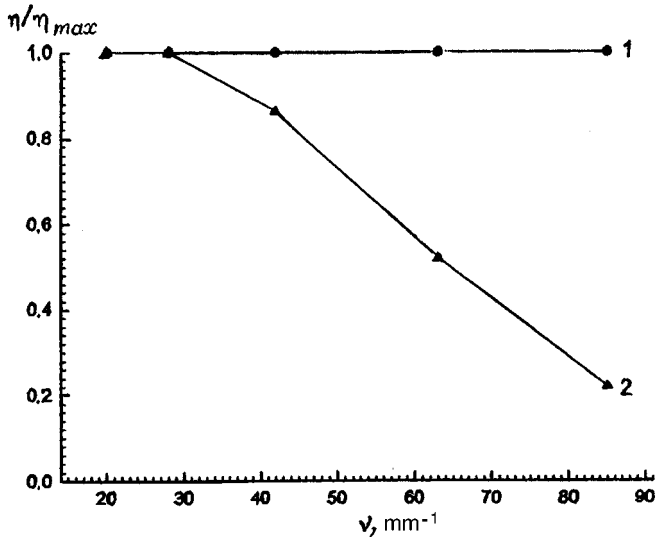


FIG. 2. Diffraction efficiency versus spatial frequency of recorded holograms: *1* — with a time-constant input signal and *2* — with amplitude modulation of the input signal.

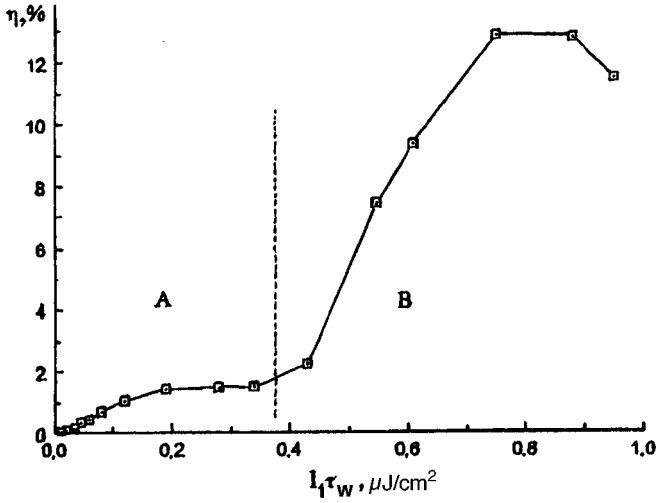


FIG. 3. Diffraction efficiency of holograms versus exposure to recording pulse $I_1\tau_W$ (the spatial recording frequency is $\nu_0=85$ mm$^{-1}$).

rated in the circuit to achieve amplitude modulation, was placed directly ahead of the He–Ne laser. In the experiment, the ratio of the recording pulse duration $\tau_W$ to the repetition period $t_W$ was maintained at 1/3 and the amplitude of the supply voltage pulse was kept at 45 V. The pulsed supply to the *p-i-n a*-Si:H–liquid crystal structure and the liquid crystal switched were synchronized by ensuring that the supply to the optically addressed modulator was in phase with the pulsations of the interference pattern reaching the photoconductor–liquid crystal interface, and the electrooptic response was formed with a phase delay relative to the input signal (Fig. 1b). Figure 2 shows the behavior of the maximum diffraction efficiency of the response formed by the *p-i-n a*-Si:H–liquid crystal structure to a time-constant test interference pattern (curve *1*) and when amplitude modulation was introduced in both interferometer arms (curve *2*). It can be seen that modulation substantially improved the resolution of the structure. The fact that the response does not depend on the spatial frequency in the operating frequency range ensures that the correlators of the combined transformation, and optical neuron networks based on these, are invariant to shift when *p-i-n a*-Si:H–liquid crystal structures are used to record Fourier holograms in real time, since any displacement relative to the etalon of the image being processed in the entry window always alters the spatial frequency of the Fourier hologram.[4]

When modulation was introduced, the maximum diffraction efficiency increased to more than 12% and was achieved for an exposing pulse of $7.5\times10^{-7}$ J/cm$^2$, i.e., without any loss in the sensitivity of the structure. Figure 3 gives the diffraction efficiency of the response formed by a *p-i-n a*-Si:H–liquid crystal structure, plotted as a function of the exposure to the recording pulse $I_1\tau_W$, where $I_1$ is the intensity of one of the two beams forming the interference pattern. The threshold sensitivity of the optically addressed modulators is at least $10^{-8}$ J/cm$^2$. Particular attention is drawn to the nonlinear behavior of the transfer characteristic, which consists of two regions (*A* and *B* in Fig. 3) with different slopes. This behavior not only avoids cutoff of the upper information frequencies of the joint Fourier transformation hologram,[4] but also ensures that they increase nonlinearly. This characteristic, like the previous one, was obtained for $t_W=40$ ms and $\tau_W/t_W=1/3$.

TABLE I.

| | Diffraction efficiency, % | |
|---|---|---|
| Speed, Hz | without modulation (Ref. 1) | with modulation |
| 8.3 | 5.5 | 12.8 |
| 11.9 | 4.6 | 12.2 |
| 27.8 | 2.3 | 7.0 |

When the repetition frequency of the recording pulses was increased, the drop in the diffraction efficiency was not so great as for the holograms recorded without modulation. Table I gives comparative data on the speed of a *p-i-n a*-Si:H–liquid crystal structure in the write–erase mode.

To conclude, by incorporating amplitude modulation of the recording beam synchronized to the supply, we can obtain high values of the parameters of rewritable optically addressed modulators, which are required to construct optical neuron networks and for various applications of real-time holographic recording.

The authors would like to thank E. I. Shubnikov for discussions of this work.

This work was supported by the Russian Fund for Fundamental Research (Grant No. 95–02–05892-a).

[1] A. V. Pavlov and E. I. Shubnikov, Opt. Memory Neural Net. **2**, No. 4, 245 (1993).
[2] E. I. Shubnikov, Opt. Zh. No. 4, 19 (1995).
[3] A. N. Chaĭka, N. L. Ivanova, A. P. Onokhov, and É. A. Nefed'eva, Pis'ma Zh. Tekh. Fiz. **21**(19), 83 (1995) [Tech. Phys. Lett. **21**, 808 (1995)].
[4] G. I. Vasilenko and L. M. Tsibul'kin, *Holographic Discriminating Devices* [in Russian], Radio i Svyaz', Moscow (1985).

Translated by R. M. Durham

# Room-temperature lasing in structures with CdSe quantum islands in a ZnMgSSe matrix without external optical confinement

A. V. Sakharov, S. V. Ivanov, S. V. Sorokin, I. L. Krestnikov, B. V. Volovik, N. N. Ledentsov, and P. S. Kop'ev

*A. F. Ioffe Physicotechnical Institute, Russian Academy of Sciences, St. Petersburg*
(Submitted January 17, 1997)
Pis'ma Zh. Tekh. Fiz. **23**, 26–30 (April 26, 1997)

It has been shown that lasing may be achieved in structures with submonolayer CdSe inclusions in a ZnMgSSe matrix at above-room temperatures without additional optical confinement of the active region by thick layers of lower refractive index. The temperature dependence of the excitation density at the lasing threshold is typical of structures with three-dimensional carrier localization. © *1997 American Institute of Physics.* [S1063-7850(97)02104-6]

Structures based on II–VI compounds and group-three nitrides have recently been studied intensively in connection with the development of light-emitting diodes and lasers operating in the blue–green part of the spectrum. The laser structures are usually grown in a standard geometry developed for III–V lasers (the active region is confined by wider-gap layers of lower refractive index). In many cases, however, it is difficult to obtain thick wide-gap layers because of the lack of a suitable heteropair or because of the difficulties involved in doping a wide-gap compound (for instance, for *p*-ZnMgSSe layers). In our previous studies,[1,2] we showed that there is no strict need for additional optical confinement to obtain lasing in structures with CdSe quantum islands in a ZnSe matrix because a waveguiding effect may be produced by an increase in the refractive index in the exciton resonance range, and the lasing is achieved via the localized-exciton ground state. Lasing occurs even if the average CdSe content in the quantum island regions is only 3–4%.

In the present paper we investigate a structure whose active region has no additional optical confinement by thick layers of lower refractive index. A short-period superlattice, of twenty periods, consisting of submonolayer CdSe inclusions with an average thickness of 0.4 monolayer, separated by 28 Å ZnMgSSe barriers, was grown on a GaAs(100) substrate by molecular-beam epitaxy.[3] The superlattice was separated from the substrate and the surface by 1 $\mu$m and 500 Å thick ZnMgSSe layers, respectively, having lattice parameters matched with the GaAs. Superlattices of ZnS/MgSe, 100 Å thick, were used for electronic confinement of the carriers in the superlattice region.

It was shown in Ref. 1 that lasing via exciton states is feasible because of the lifting of the momentum selection rules, caused by the spatial localization of the exciton and lowering of the symmetry of the system. In our case, the distance between the lasing energy and the photoluminescence energy of the submonolayer superlattice is 28 meV at room temperature, whereas in ZnCdSe/ZnSe quantum-well structures, the lasing energy is usually shifted by 30–60 meV in the long-wavelength direction. This shift is caused by an electron–phonon amplification mechanism in free-exciton structures,[4] since a ''hot'' exciton with a large waveguide vector cannot recombine radiatively.[5]

It was demonstrated in Ref. 2 that lasing may be achieved in a structure formed by CdSe submonolayers in a ZnSe matrix. In this case, however, the lasing was only obtained at fairly low temperatures ($T<120$ K). A sharp rise in

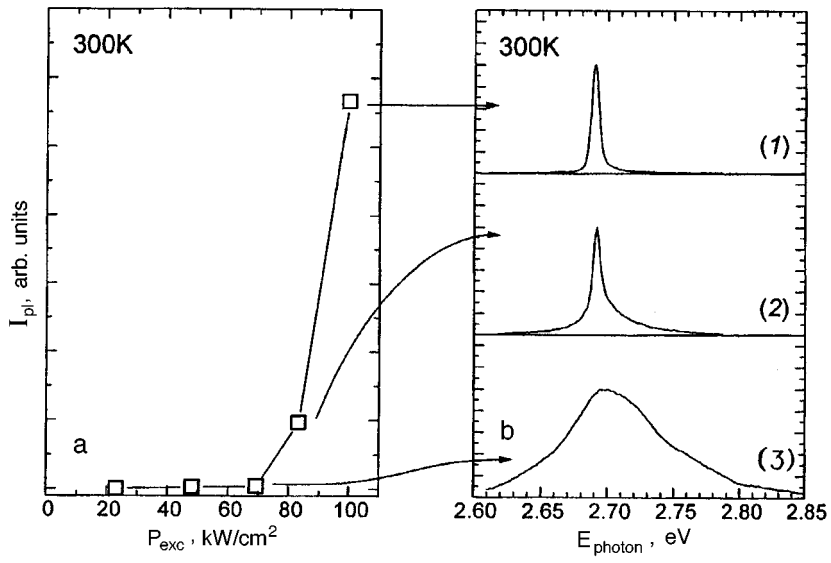


FIG. 1. a — Intensity of photoluminescence from the end as a function of excitation density; b — Spectra of luminescence from the end at various excitation densities (100 kW/cm$^2$ — *1*, 83 kW/cm$^2$ — *2*, and 69 kW/cm$^2$ — *3*).

 1063-7850/97/040305-02$10.00  

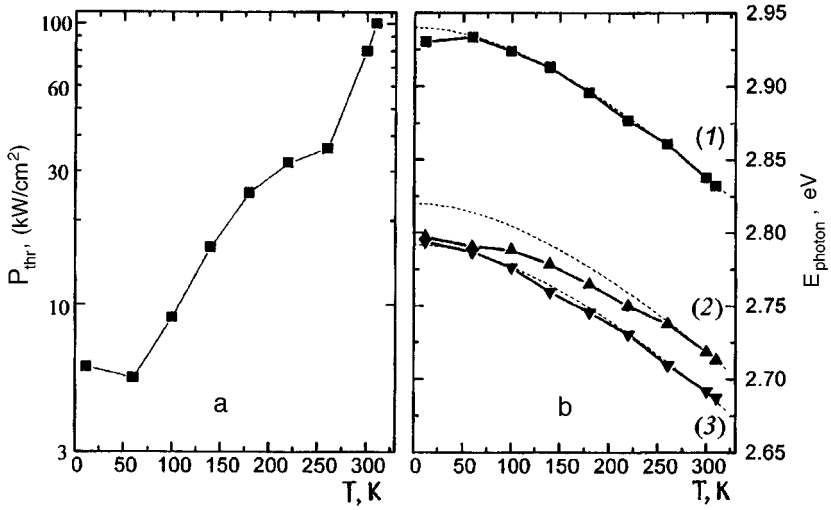


FIG. 2. a — Temperature dependence of the threshold excitation density; b — temperature dependence of the surface photoluminescence energy for the matrix (*1*) and the submonolayer superlattice (*2*) (excitation density 1 W/cm$^2$), and temperature dependence of the lasing energy (*3*).

the threshold excitation density was observed with increasing temperature, which may be caused by thermal ejection of carriers into the matrix or by an increase in the width and decrease in the amplitude of the exciton modulation of the refractive index. In the present study, we placed the CdSe submonolayers in a wider-gap ZnMgSSe matrix, which appreciably increased the localization energy and suppressed the thermal ejection.

Figure 1 gives the photoluminescence intensity of a doubly cleave sample as a function of the excitation density, as well as the lasing spectra for various excitation densities (recorded at 300 K). It can be seen that at excitation densities of the order of 80 kW/cm$^2$, the half-width of the photoluminescence line falls sharply to 6 meV, which suggests a transition to lasing.

Figure 2a gives the threshold excitation density versus temperature. At low temperatures we observe a section with a negative temperature dependence, typical of structures with three-dimensional carrier localization.[6] As the temperature increases, the threshold excitation density increases slowly but at temperatures above 260 °C, it begins to rise sharply as a result of thermal ejection of carriers into the matrix.

Figure 2b shows temperature dependences of the energy position of the edge photoluminescence lines for a ZnMgSSe matrix, and the photoluminescence from the CdSe submonolayer superlattice, recorded from the surface of the sample. Also plotted is the temperature dependence of the lasing energy. It can be seen that the edge photoluminescence energy agrees with the temperature dependence of the ZnMgSSe band gap. The small difference observed at low temperatures can be attributed to the localization of excitons at fluctuations in the composition of the quaternary solid-solution. The lasing energy follows the temperature dependence of the band gap, which indicates that the lasing mechanism remains unchanged. However, the temperature dependence of the photoluminescence from the submonolayer superlattice reveals three sections which match the sections on the temperature curve of the threshold excitation density. At low temperatures, the main contribution to the photoluminescence is made by large islands with a high localization energy. Then, as the temperature increases, the carriers become redistributed between the islands and the higher-energy states become populated, and at temperatures above 260 °C, the photoluminescence peak follows the temperature curve of the band gap.

To sum up, we have demonstrated that phonon-free lasing may be achieved at above-room temperatures (40 °C) in structures with CdSe quantum islands without additional optical confinement. We attribute the retention of high gain to an increase in the carrier localization energy when the islands are incorporated in the matrix of a wider-gap material. It has also been shown that the exciton-induced modulation of the refractive index is sufficient to produce a waveguiding effect and sustain it up to above-room temperatures.

This work was supported by grant INTAS-94-481 and by a grant from the Russian Fund for Fundamental Research No. 95-02-04056.

[1] N. N. Ledentsov, I. L. Krestnikov, M. V. Maximov, S. V. Ivanov, S. V. Sorokin, P. S. Kop'ev, Zh. I. Alferov, D. Bimberg, and C. M. Sotomayor Torres, Appl. Phys. Lett. **69**, 1343 (1996).
[2] I. L. Krestnikov, N. N. Ledentsov, M. V. Maximov, A. V. Sakharov, S. V. Ivanov, S. V. Sorokin, L. N. Tenishev, P. S. Kop'ev, and Zh. I. Alferov, Pis'ma Zh. Tekh. Fiz. **23**(1), 33 (1997) [Tech. Phys. Lett. **23**, 23(1997)].
[3] S. V. Ivanov, S. V. Sorokin, P. S. Kop'ev, J. R. Kim, H. D. Jung, and H. S. Park, J. Cryst. Growth. **159**, 16 (1996).
[4] Y. Kawakami, I. Hauksson, H. Stewart, J. Simpson, I. Galbraith, K. A. Prior, and B. C. Cavenett, Phys. Rev. B **48**, 11994 (1993).
[5] S. A. Permogorov, Phys. Status Solidi B **68**, 9 (1975).
[6] A. E. Zhukov, A. Yu. Egorov, A. R. Kovsh, V. M. Ustinov, N. N. Ledentsov, M. V. Maksimov, A. F. Tsatsul'nikov, S. V. Zaĭtsev, N. Yu. Gordeev, P. S. Kop'ev, D. Bimberg, and Zh. I. Alferov, Fiz. Tekh. Poluprovodn. [in press (1997)].

Translated by R. M. Durham

# Influence of multilevel crystallization on the intensity oscillations of diffracted high-energy electrons during growth of aluminum arsenide by molecular beam epitaxy

A. N. Alekseev, S. Yu. Karpov, M. A. Maĭorov, and V. V. Korablev

*Advanced Technology and Development Center, St. Petersburg; St. Petersburg State Technical University*
(Submitted January 17, 1997)
Pis'ma Zh. Tekh. Fiz. **23**, 31–36 (April 26, 1997)

Theoretical and experimental investigations are made of the influence of multilevel crystallization on oscillation of the specular reflection intensity of diffracted high-energy electrons during growth of aluminum arsenide by molecular beam epitaxy. The kinematic approximation is used to construct a model to analyze the profile of the oscillation curve and its dependence on the filling of the excess layers. The theoretical predictions are compared with the experimental data. © *1997 American Institute of Physics.* [S1063-7850(97)02204-0]

Since the eighties, recording of oscillations of the high-energy electron diffraction intensity has been widely used to study the mechanisms of growth of semiconductor crystals using molecular beam epitaxy.[1,2] The interpretation of the profile of the oscillation curves has been discussed most comprehensively for GaAs. In particular, it was shown in Refs. 2 and 3 that a two-level surface model, which only allows for the formation and growth of two-dimensional one-monolayer-high islands, yields good agreement with the experimental observations. According to Ref. 3, the decrease in the specular reflection intensity $\Delta I$ in this case is proportional to $\theta(1-\theta)$, where $\theta$ is the degree of filling of the upper, growing monolayer. However, the behavior of the oscillation curves obtained during growth of AlAs and InGaAs on GaAs (Ref. 4) differs appreciably from that predicted by the two-level model. This difference may be explained by multilevel crystallization effects, whereby nucleation and growth of nuclei take place in several upper layers simultaneously.

The aim of the present study is to identify, theoretically and experimentally, the main aspects of the influence of multilevel crystallization on the profile and behavior of the specular reflection oscillation curves of diffracted high-energy electrons.

The analysis was performed using a kinematic model of diffraction which allows for scattering of an electron beam by surface atoms distributed in different layers of the growing crystal. In the kinematic approximation, the intensity of the diffracted high-energy electrons scattered by surface atoms is given by

$$I=\left|\sum_n f_n\cdot\exp(i\mathbf{K}\cdot\mathbf{r_n})\right|^2, \tag{1}$$

where the vector $\mathbf{r_n}$ describes the position of the $n$th atom on the rough surface of the growing crystal, $\mathbf{K}=\mathbf{k}-\mathbf{k_0}$ is the scattering vector ($\mathbf{k_0}$ and $\mathbf{k}$ are the wave vectors of an incident and scattered wave, respectively), and $f_n$ is the scattering amplitude of a single atom. The vector $\mathbf{r_n}$ may be expressed in the form $\mathbf{r_n}=\mathbf{r_n}^0+a\nu_n\cdot\mathbf{e_z}$, where $\mathbf{r_n}^0$ is a vector lying in the plane of the uppermost completely filled crystal layer, $a\nu_n$ describes the local height of the surface roughness ($a$ is the monolayer thickness and $\nu_n$ is the number of layers at the point corresponding to the vector $\mathbf{r_n}^0$, measured from the last filled layer with $\nu_n=0$), and $\mathbf{e_z}$ is the unit vector perpendicular to the crystal growth plane.

We shall assume that layers with $\nu>0$ are only partially filled, and then each layer may be characterized by its degree of filling or by the coverage of the given layer $\theta_\nu=N_\nu/N$, where $N_\nu$ is the number of atoms in the $\nu$th layer and $N$ is the total number of atoms on the plane sections of the surface. Provided that there are no structures where the next layer ''overhangs'' the previous one, the number of atoms of the $\nu$th layer contributing to the scattering of an electron wave will obviously be $N(\theta_\nu-\theta_{\nu-1})$. Then, assuming that the scattering amplitude $f_n$ does not depend on the layer number or the position of the atom (on the plane section of the surface or near a step), expression (1) may be transformed to give

$$I=I_0\left|\sum_{\nu=0}[\theta_{\nu+1}-\theta_\nu]\exp(i2\phi\nu)\right|^2, \tag{2}$$

where $2\phi=(\mathbf{K}\cdot\mathbf{e_z})a$, and $I_0$ is the electron diffraction intensity at an atomically smooth surface.

For purposes of clarity, we introduce various simplifying assumptions relating to the filling of the layers on a multilevel surface. We shall assume that the coverages of adjacent monolayers satisfy the universal relation $\theta_{\nu+1}=\gamma\theta_\nu$, where $\gamma$ is a parameter which does not depend on the layer number $\nu$, and the coverage of the first layer $\theta_1=\theta$ varies arbitrarily and is unrelated to the filling of the preceding layers. The case $\gamma=0$ clearly corresponds to the two-level system analyzed in Ref. 3. As $\gamma$ increases, the surface becomes multilevel and the case $\gamma\sim1$ ($\theta<1$) in fact describes a system of three-dimensional isolated islands distributed over the crystal surface.

Under these assumption, the coverage of the $\nu$th layer may be expressed as $\theta_\nu=\theta\cdot\gamma^{\nu-1}$, and after summation in Eq. (2), the diffraction intensity has the form

$$I=I_0\left\{1-\frac{4\sin^2\phi}{(1+\gamma)^2-4\gamma\cdot\cos^2\phi}[\theta\cdot(1-\theta)+\gamma\theta]\right\}. \tag{3}$$

It can be seen from Eq. (4) that the intensity at the maxima and minima of the oscillation curve are respectively given by

 1063-7850/97/040307-02$10.00  

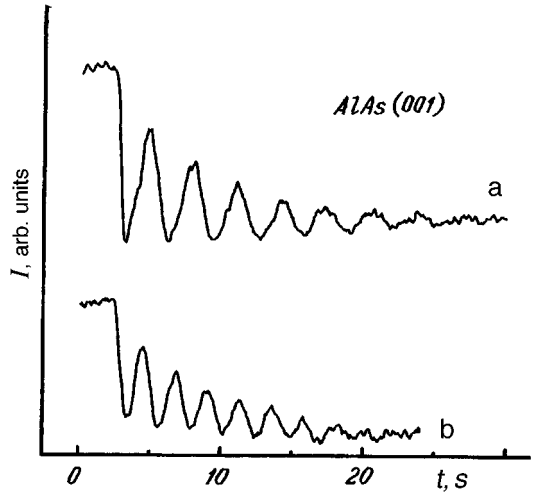


FIG. 1. Oscillations of the specular reflection intensity after the onset of AlAs growth: a — for an anti-Bragg diffraction geometry; b — with deviation from anti-Bragg diffraction conditions.

$$I_{\max}=I_0\frac{(1-\gamma)^2}{(1+\gamma)^2-4\gamma\cdot\cos^2\phi}, \tag{4a}$$

$$I_{\min}=I_0\frac{(1-\gamma)^2\cdot\cos^2\phi}{(1+\gamma)^2-4\gamma\cos^2\phi}. \tag{4b}$$

Let us examine various consequences of the proposed model. Let us assume that $\gamma=0$ before the onset of growth and that $\gamma$ increases slowly with time during the growth process, characterizing the evolution of a multilevel surface. Then, if the anti-Bragg conditions are exactly satisfied, the intensity of the minima is zero, and the maxima of the oscillation curve decay with increasing $\gamma$ as

$$I_{\max}=I_0\left(\frac{1-\gamma}{1+\gamma}\right)^2. \tag{5}$$

If the anti-Bragg conditions are not exactly satisfied, then, according to Eq. (4), the intensity of the maxima and the minima of the oscillation curve will decay at the same rate.

Another consequence of the model is a sharp fall in the intensity of the diffracted electrons at the first period of the oscillations, accompanying the formation of three-dimensional islands on the surface ($\gamma\sim1$, $\theta<1$). This behavior of the oscillation curves is typical of the growth of strained InGaAs structures on GaAs.[4]

For the experimental investigations we selected AlAs, a material exhibiting a tendency toward multilevel crystallization when grown by molecular-beam epitaxy. The experiments were carried out on GaAs(001) substrates after a $0.5\mu$m thick buffer layer of gallium arsenide had been grown on them. The $As_4$ flux was kept constant ($\sim2$ ML/s) throughout the experiment. The specular reflection intensity of the diffracted high-energy electrons was measured in the (110) azimuthal direction at an electron beam energy of 10 keV.

Figure 1a and 1b shows oscillation curves obtained for AlAs, which demonstrate multilevel crystallization effects. Figure 1a corresponds to anti-Bragg scattering geometry.

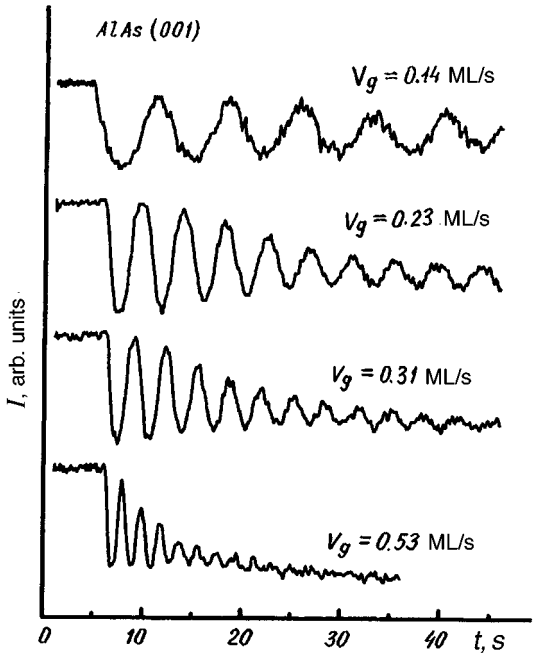


FIG. 2. Oscillations of the specular reflection intensity obtained at various AlAs growth rates.

The model predicts that the intensity of the diffracted electrons at the minima of the oscillation curve will remain almost constant while the maxima decay as a result of the gradual evolution of a multilevel surface during the growth process. Figure 1b is plotted for a small deviation from anti-Bragg geometry. It can be seen that, the intensity of both the maxima and the minima decay.

Figure 2 shows oscillation curves obtained at 525 °C and various growth rates under conditions close to anti-Bragg geometry. It can be seen that at a low growth rate ($V_g=0.14$ ML/s), the maxima show little decay; i.e., the degree of filling of the layers formed above the main growing surface ($\nu=1$) is negligible. Conversely, at a high growth rate ($V_g=0.53$ ML/s) the surface becomes essentially multilevel in the first three oscillations. Estimates made using expression (5) show that for a few periods after initiation of the aluminum flux, $\gamma$ increases linearly as a function of the number of deposited monolayers. At a growth rate of 0.14 ML/s the rate of increase in $\gamma$ is 0.025 ML/s, whereas at 0.53 ML/s the rate of increase is three times higher. Thus, the rate of evolution of multilevel crystallization is determined to a considerable extent by the rate of crystal growth.

This work was supported by the International Science Foundation (Grant R16300).

[1] P. J. Dobson, B. A. Joyce, J. H. Neave, and J. Zhang, J. Cryst. Growth **81**, 1 (1987).
[2] J. M. Van Hove, C. S. Lent, P. R. Pukite, and P. I. Cohen, J. Vac. Sci. Technol. B **1**, 741 (1983).
[3] C. S. Lent and P. I. Cohen, Surf. Sci. **139**, 121 (1984).
[4] N. Grandjean and J. Massies, J. Cryst. Growth **134**, 51 (1993).

Translated by R. M. Durham

# Laser-chemical gas-phase synthesis of highly disperse titanium carbide ceramic powders

G. I. Kozlov

*Institute of Problems in Mechanics, Russian Academy of Sciences, Moscow*
(Submitted November 21, 1996)
Pis'ma Zh. Tekh. Fiz. **23**, 37–41 (April 26, 1997)

Gas-phase synthesis of titanium carbide powders is described. A thermodynamic analysis is made to optimize the process parameters. Preliminary experiments were carried out using a system incorporating a cw gas-discharge multibeam $CO_2$ laser and these demonstrated the advantages of the laser-chemical process over other methods. © *1997 American Institute of Physics.* [S1063-7850(97)02304-5]

The aim of the present study is to develop a new efficient technological process for the continuous laser-chemical gas-phase synthesis of highly disperse titanium carbide ceramic powders, possessing good hardness and wear resistance.

It is known that the carbon–titanium system has only one carbide phase, TiC, which is high-melting ($T_{mp}=3420$ K) and possesses good microhardness ($H_\mu=3200$ kgf/mm$^2$). These characteristics have promoted the widespread use of titanium carbide in industry to fabricate various fire-resistant components and metal-ceramic instruments. However, the existing technological processes for obtaining silicon carbide in a discharge plasma[1] do not meet contemporary requirements for a high-purity product with specific properties.

The process of laser-chemical gas-phase synthesis of highly dispersed titanium carbide powders, as developed by us, is based on the laser pyrolysis of suitable reagents in a high-power $CO_2$ laser radiation field. For the implementation of such a process, it is important to know what are the optimum conditions required to synthesize titanium carbide. Thermodynamic calculations indicate that titanium carbide is formed only in the condensed phase, over a wide range of temperatures, roughly between 1200 and 3000 K. However, the optimum temperature range for the production of pure titanium carbide is considerably narrower. In fact, at temperatures up to approximately 2200 K, a considerable amount of carbon is formed in the condensed phase as well as the titanium carbide. In practice, a sufficiently pure product can only be obtained at temperatures above 2300 K. A high-temperature limit is also imposed, since at temperatures above 2500 K significant quantities of hydrocarbons (such as $C_2H_2$, and so on) are formed in the system. A thermodynamic analysis therefore indicates that the optimum temperature range for the production of titanium carbide at atmospheric pressure is approximately 2300–2500 K. Preliminary experiments have shown that these conditions may be achieved with a fairly high-power $CO_2$ laser, capable of delivering a high intensity (higher than $10^4$ W/cm$^2$) in a reaction zone of the order of a few millimeters.

A prerequisite for the laser-chemical gas-phase synthesis of titanium carbide powder is that at least one of the reagents should fairly strongly absorb the laser radiation. In our experiments to synthesize titanium carbide, this reagent was propane containing a small quantity of butane. The second reagent was titanium tetrachloride.

Experiments to synthesize ceramic powders were carried out using an apparatus incorporating a 6 kW, diffusion-cooled, cw gas-discharge multibeam $CO_2$ laser. The laser radiation, with a divergence of $3\times10^{-3}$ rad, was focused by a potassium chloride lens of 110 cm focal length onto the edge of a special burner. The diameter of the focusing spot, i.e., the characteristic size of the zone of interaction between the laser beam and the reagent flux from the burner, was approximately 6.5 mm. The burner had a rectangular cross section, 30 mm long in the direction of the laser beam and 10 mm in width and incorporated a special container filled with liquid titanium tetrachloride. Propane supplied to the burner bubbled through the $TiCl_4$, becoming saturated with vapor, and the resultant vapor–gas reagent mixture was fed to the exit cross section of the burner. The laser beam crossed the reagent jet at the edge of the burner, thereby fixing the reaction zone in space. Since in this case, the reaction zone has quite specific dimensions, which are determined by the diameter of the focusing region of the laser beam, the growth of the forming titanium carbide particles can be reliably controlled by varying the residence time of the reagents in the reaction zone. The reagent flux leaving the burner was isolated from the atmospheric air by a coaxial shield of helium gas.

The temperature in the reaction zone was measured by an optical pyrometer, which recorded the brightness temperature of the reagent flux.

Finally, the titanium carbide particles formed in the gas-phase synthesis reaction were collected on a cold metal surface by briefly inserting special metallic ''mushrooms'' in the stream of reaction products directly above the reaction zone. These mushrooms could be mounted on the stage of an electron microscope.

At the first stage of the process development, we investigated the action of the high-power laser radiation on the propane jet alone, in order to determine the intensities at which the propane dissociated to form the active atoms and radicals needed to synthesize the titanium carbide. In the course of these experiments, it was observed that at intensities of approximately $2\times10^4$ W/cm$^2$, a brightly luminous jet of laser pyrolysis products of propane is produced, accompanied by the profuse formation of carbon particles. Mea-

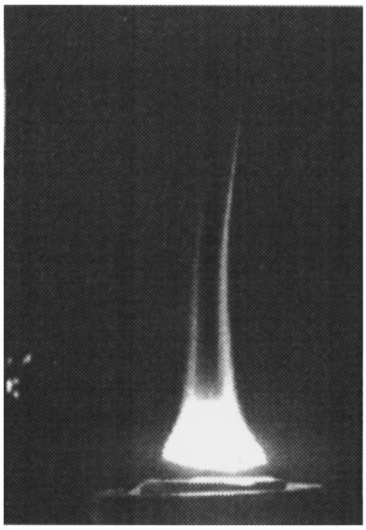

FIG. 1. Photograph showing the region of interaction between the laser beam and the stream of gas–vapor mixture leaving the burner.

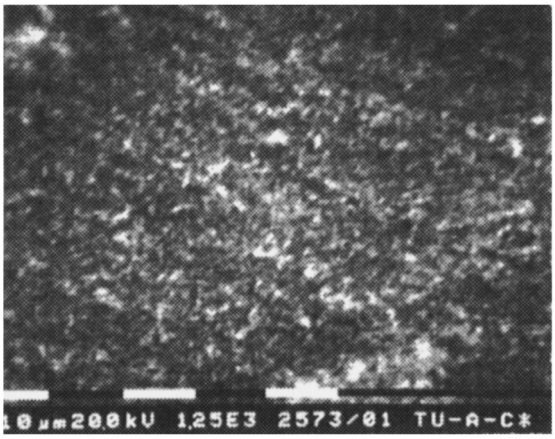


FIG. 2. Electron micrograph of laser-synthesized powder, 10 $\mu$m per division.

surements indicated that the temperature of the jet burning in the laser beam was 2800 K, which creates favorable conditions for the gas-phase pyrolysis of titanium carbide particles, as is deduced from the analysis of the results of the thermodynamic calculations presented above.

After these measurements, $TiCl_4$ was poured into the burner and the propane jet became saturated with this reagent. At the exit from the burner, the stream of vapor–gas mixture crossed the region of the laser beam, where the reagents were pyrolyzed and titanium carbide particles were synthesized. The reaction zone in the laser beam glowed with a dazzling brightness, and can be identified, together with the trail of forming particles, in the photograph shown in Fig. 1. The particles were collected on a metal surface directly beyond the reaction zone, where the glow and therefore the temperature of the reaction products were already reduced. This is one of the main advantages of the laser-chemical process over other methods: the laser beam can form a strictly defined, fairly narrow reaction zone in space, which is difficult to accomplish as efficiently by other methods.

The titanium carbide powder synthesized in the laser beam was analyzed under an electron microscope. Figure 2 shows a photograph of the powder, which shows that the average size of the particles synthesized by laser pyrolysis is less than a micron and the particles are nearly spherical. Further experiments will allow us to determine the conditions for producing nanosize powder, as well as the degree of purity, which is extremely important for applications.

To conclude, the author would like to thank V. A. Lakutin for assistance with this work.

[1] R. L. Stephens, J. S. Me Featers, and B. L. Welch, *Abstracts of Papers Presented at the 11th International Symposium on Plasma Chemistry*, Loughborough University, 1993, pp. 65–70.

Translated by R. M. Durham

# Numerical simulation of the extraction of ions from a magnetized plasma

N. S. Demidova and V. A. Mishin

*Institute of General Physics, Russian Academy of Sciences, Moscow*
(Submitted October 22, 1996)
Pis'ma Zh. Tekh. Fiz. **23**, 42–46 (April 26, 1997)

The extraction of ions from a magnetized plasma in laser isotope separation systems is analyzed using one-dimensional, time-dependent equations of two-fluid magnetohydrodynamics. It is suggested that electron emission from the cathode may be used to compensate for the ion space charge which limits the rate of extraction. It is shown that at an accelerating voltage of 25 V and an emission current of 2.5 mA/cm$^2$, a plasma with a density of $10^{11}$ cm$^{-3}$ is accelerated to a velocity of $1.5\times10^5$ cm/s in 3 $\mu$s. In this case, the maximum temperature of the plasma electron component does not exceed 1.5 eV. © *1997 American Institute of Physics.* [S1063-7850(97)02404-X]

A method of isotope separation based on the isotopically selective photoionization of atoms (AVLIS method) has recently been developed intensively. The method is based on the idea of photoionization of a particular isotope by laser radiation during free-molecular flow of vapor of the material being separated through the irradiation zone, followed by extraction of the resultant plasma ions. The basic problem in the extraction process is that the laser-produced ions rapidly exchange charge with neutral atoms of other isotopes, which lowers the enrichment factor. Thus the development of an efficient method of ion extraction is one of the basic problems for the practical implementation of the process.

The ions may be extracted by a method based on the electric-field-induced acceleration of the ions in a magnetic field perpendicular to the electric field (Hall plasma accelerator). If the electron drift current is closed, the charges cannot be separated in the $E$ direction within times of the order of the period of the plasma frequency and the electric field penetrates into the plasma. The acceleration process is only slowed when an ion space charge is formed. To compensate for this, we propose that electrons should be emitted from the cathode.

We give some typical plasma parameters in the extractor. The neutral atom density is $10^{13}-10^{14}$ cm$^{-3}$ and the initial plasma density is $10^{11}$ cm$^{-3}$. The plasma is neutral and the initial temperature of the electron and ion components, $T_e$ and $T_i$, is 0.1 eV. The interelectrode gap is 2 cm. It is assumed that the plasma is generated by laser radiation in an external magnetic field $B_{0z}$. The magnetic field is assumed to be 33 G, which satisfies the conditions for magnetization of the electrons without magnetization of the ions. We neglect the magnetic self-field of the plasma currents. The potential difference is assumed to be 25 V. For the selected magnetic field, the Hall parameter $\omega_e\tau$ is 10, where $\tau$ is the total frequency of electron collisions and is given by $1/\tau=\upsilon_{ei}+\upsilon_{ea}$.

For the numerical simulation we used a system of one-dimensional, transient equations of two-fluid magnetohydrodynamics. The plasma electron component is heated by passing a current through the discharge gap and is cooled by inelastic interaction with neutral atoms. The numerical simulation was performed for ytterbium vapor (the system and method of isotopically selective photoionization were extensively developed in Ref. 1). For ytterbium, the main contribution to the heat losses is made by inelastic collisions, which excite atoms from the $6^1S_0$ ground state to the $6^1P_1$ and $7^1P_1$ states, with energies $\Delta E=3.1$ and 5.02 eV, respectively. The rate constant $\langle\upsilon\sigma\rangle$ for excitation of a transition with the energy $\Delta E$ was estimated according to a formula proposed in Ref. 2. It was assumed that the neutral atom density is so high that they form an infinite energy reservoir.

The system of equations has the form:

$$\frac{\partial n_i}{\partial t}+\frac{\partial}{\partial x}(n_i\upsilon_{ix})=0, \tag{1}$$

$$Mn_i\left(\frac{\partial}{\partial t}\upsilon_{ix}+\upsilon_{ix}\frac{\partial}{\partial x}\upsilon_{ix}\right)=-kT_{i0}\frac{\partial n_i}{\partial x}+en_iE_x, \tag{2}$$

$$\frac{\partial n_e}{\partial t}+\frac{\partial}{\partial x}(n_e\upsilon_{ex})=0, \tag{3}$$

$$en_e\frac{\partial\varphi}{\partial x}-k\frac{\partial n_eT_e}{\partial x}-\frac{e}{c}\omega_e\tau\upsilon_{ex}n_eB_{0z}-\frac{\upsilon_{ex}}{\tau}mn_e=0, \tag{4}$$

$$\frac{\partial^2\varphi}{\partial x^2}=-4\pi e(n_i-n_e), \tag{5}$$

$$\frac{3}{2}kn_e\left(\frac{\partial T_e}{\partial t}+\upsilon_{ex}\frac{\partial T_e}{\partial x}\right)=-\frac{\partial\chi_\perp}{\partial x}\frac{\partial T_e}{\partial x}+\frac{j_x^2}{\sigma_\perp}-kn_eT_e\frac{\partial\upsilon_{ex}}{\partial x}-\langle\upsilon_{et}\sigma\rangle N_a\Delta En_e. \tag{6}$$

Here $\chi_\perp$ and $\sigma_\perp$ are the transverse electron thermal conductivity and the transverse conductivity, respectively. As the initial conditions we have: $n_i=n_e=10^{11}$ cm$^{-3}$ and $\upsilon_i=\upsilon_e=0$. As the boundary conditions we have: $n(0)=n(L)=0$ (for the electrons and ions), $\varphi(0)=\varphi_0$, $\varphi(L)=0$, and $T_e(0)=T_e(L)=0.1$ eV. The emission current from the cathode was given by: $j_e=n_e\upsilon_t/(\omega_e\tau)$. The emission process is self-consistent with the solution of the Poisson equation (5) and electrons are only emitted in the presence of an electric field at the cathode. The system (1)–(6) was solved by a method of conservative difference schemes in Lagrangian coordinates.

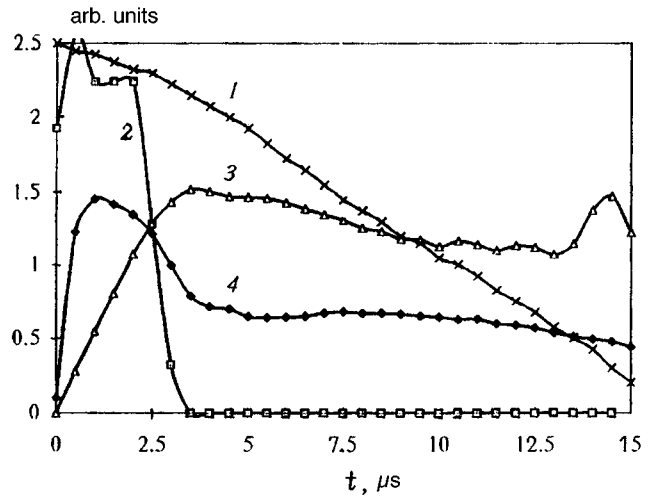


FIG. 1. Extraction dynamics allowing for heating and cooling of the plasma: *1* — dynamics of ion extraction, arb. units; *2* — dynamics of emission current, mA; *3* — mass-averaged ion velocity, $\times 10^5$ cm/s; *4* — mass-averaged electron temperature, eV. The extractor parameters are: anode–cathode gap 2 cm, accelerating voltage 25 V, initial plasma density $10^{11}$ $cm^{-3}$, and neutral atom density $10^{14}$ $cm^{-3}$.

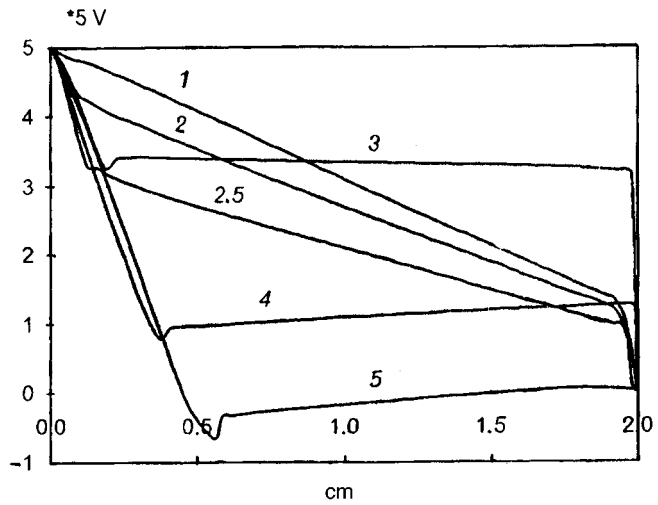


FIG. 2. Potential distribution at various times. The numbers on the curves give the time in microseconds. The extractor parameters are: anode–cathode gap 2 cm, accelerating voltage 25 V, initial plasma density $10^{11}$ $cm^{-3}$, and neutral atom density $10^{14}$ $cm^{-3}$.

The dynamics of the extraction process is shown in Fig. 1. It can be seen that at the initial stage of the process, the plasma is accelerated for $3\mu$s and the ions acquire a velocity of $1.5\times 10^5$ cm/s. During this time an electron emission current, having a density of 2.5 mA/$cm^2$, flows in through the plasma, heating it to 1.5 eV. Figure 2 shows the distribution of the potential in the plasma gap at various times between 0.5 and 4 $\mu$s. It can be seen that the electric field in the plasma disappears $3\mu$s after the beginning of acceleration. A weak electric field induced by the magnetization of the electrons and decelerating the plasma can be identified during the period of free plasma motion. This field plays a positive role, since it slows the ions formed by secondary ionization. Resonant charge transfer and secondary ionization by electrons can obviously only influence the separation factor during the period of ion acceleration ($3\mu$s). The secondary ions formed after this period cannot reach the collector because there is no electric field inside the plasma layer and no momentum is transferred by secondary ionization and charge transfer.

The authors would like to thank Professor A. A. Rukhadze for discussions of the results, the staff of the Atomic Spectroscopy Laboratory at the Institute of General Physics of the Russian Academy of Sciences for their participation, and the ''ALTEK'' AO for financial assistance with this work.

[1] S. K. Borisov, M. A. Kuz'mina, and V. A. Mishin, Prikl. Fiz. No. 1, 65 (1995).
[2] H. van Regemorter, Astrophys. J. **136**, 906 (1962); see also: L. A. Vaĭnshteĭn, I. I. Sobel'man, and E. A. Yukov, *Cross Sections for Electron Excitation of Atoms and Ions* [in Russian], Nauka, Moscow, 1973).

Translated by R. M. Durham

# Synchronization of self-excited stochastic systems by a pulsed signal

V. V. Rozhdestvenskiĭ and Yu. V. Rozhdestvenskiĭ

*Moscow Physicotechnical Institute, Dolgoprudnyĭ Branch*
(Submitted February 16, 1997)
Pis'ma Zh. Tekh. Fiz. **23**, 47–52 (April 26, 1997)

It is shown by means of a natural experiment that the synchronization of smooth fluxes is caused by the presence of stable fragments on their trajectories. © *1997 American Institute of Physics.* [S1063-7850(97)02504-4]

The phenomenon of synchronization as a transition from chaotic oscillations to periodic oscillations coherent with a periodic external signal has been analyzed by many authors (a review of studies on this topic is presented in Ref. 1). However, the cause and mechanism of this phenomenon are still unclear. In our previous studies[2,3] we demonstrated theoretically and numerically that the synchronization of smooth maps is caused by the presence of stable fragments on their trajectories and we advanced the hypothesis that smooth maps possess such fragments. In the present paper we propose to show by means of a natural experiment that a similar synchronization mechanism is also feasible for smooth fluxes.

The system studied was a radiophysical self-excited stochastic oscillator,[4] shown schematically in Fig. 1a, where *1* is a phase inverter, *2* is a nonlinear delayless element, *3* is a buffer stage, *4* is a low-frequency filter, *5* is the external signal input, *6* is the output, $C=1000$ pF, $R_1=825\ \Omega$, $R_2=500\ \Omega$, $R_3=18\ \Omega$, and $R_4=160\ \Omega$. Stage *2* is a two-cycle stage, consisting of two KP103M field-effect transistors, and its characteristic is shown in Fig. 1b. The low-frequency filter is a six-element $LC$ filter with $\Pi$-shaped elements, a characteristic resistance of 1330 Ω, and a cutoff frequency of 85 kHz.

As well as the usual set of equipment, the experimental setup also included a personal computer with an L-1230 12-

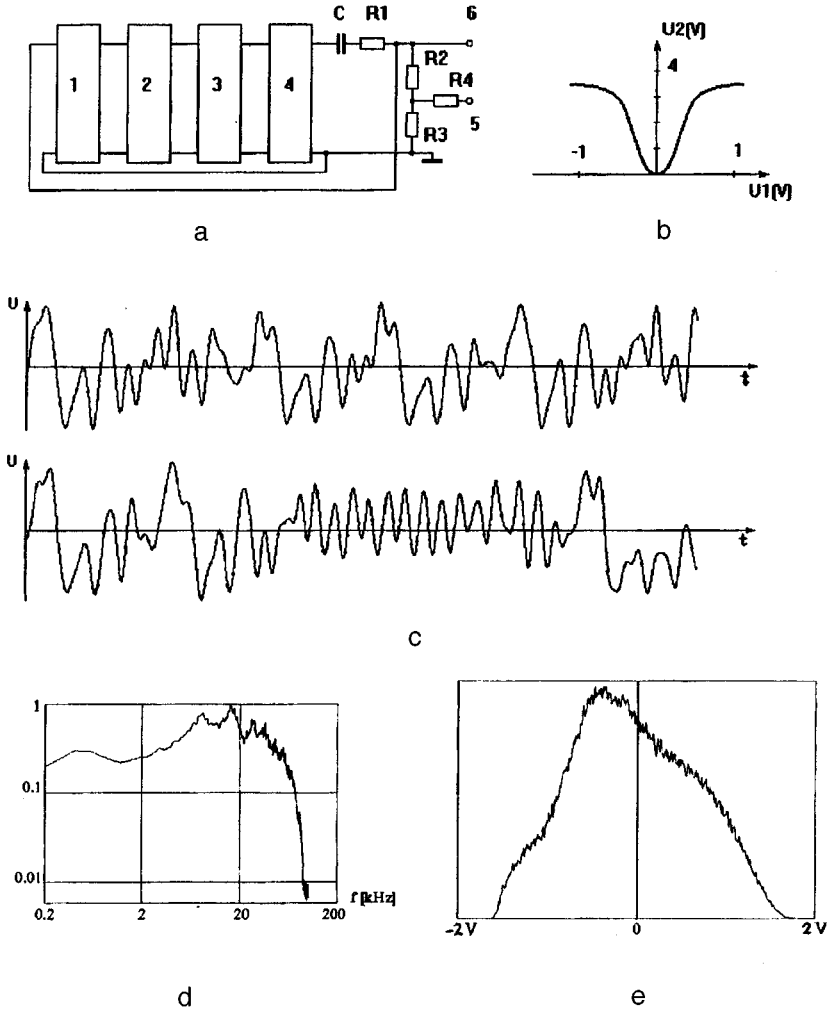


FIG. 1. Diagram of self-excited oscillator and oscillation characteristics in autonomous mode.

 1063-7850/97/040313-03$10.00  

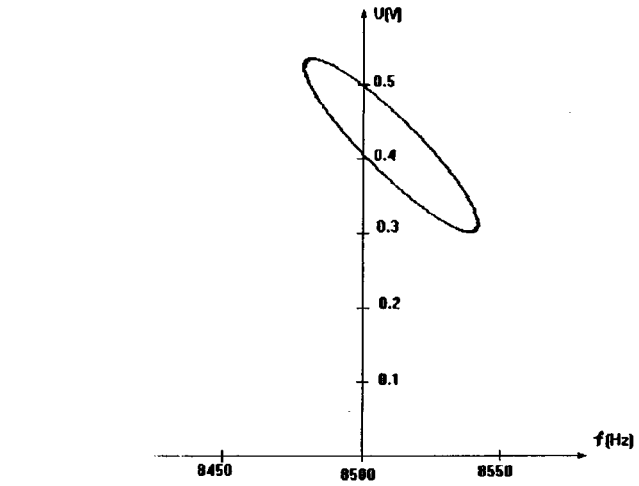


a

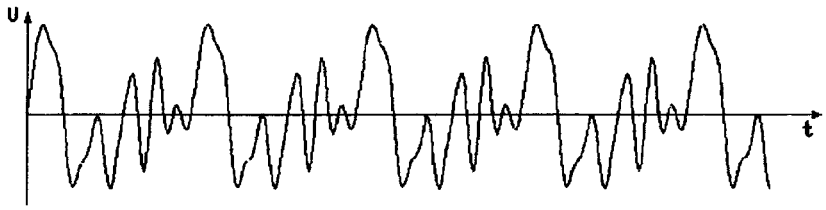


b

FIG. 2. Region of synchronization of four-cycle cycle and oscilloscope trace of synchronized oscillations.

bit, 250 kHz analog–digital card. Our application program package allowed the computer to operate as a digital oscilloscope to measure the statistical characteristics of the signal, and to determine the point dimension of the attractor. Figures 1c–1e show trajectory fragments, as well as the spectrum and distribution function of the oscillations of a self-excited oscillator in the autonomous regime. The attractor dimension in this regime was $D_p=4.2$.

Unlike previous investigations, where synchronization by a harmonic signal was studied, we analyzed synchronization by a pulsed signal. The action of a short pulse (in the $\delta$-pulse limit) on the dynamic system induces an instantaneous shift of the mapping point in the phase space by a displacement vector which is determined by the parameters of the pulsed signal and the its point of application to the system. In other respects, the system moves autonomously. Thus, synchronization by a pulsed signal, i.e., the formation of stable periodic motion, can be achieved provided that two conditions are satisfied: 1) orbit-stable fragments exist on the trajectories of the autonomous system and 2) the action of the pulse shifts the final point of the stable fragment to the initial point.

First, using a procedure described in Ref. 3, we performed a numerical simulation of pulsed synchronization using a simplified mathematical model of an oscillator — a two-dimensional smooth map:[4,5]

$$x(t+1)=(1-c)F(px(t))-ay(t)+\varphi(t),$$

$$y(t+1)=cF(px(t))+ay(t), \quad F(z)=z^2/(1+z^2). \quad (1)$$

In these formulas $x$ is proportional to the voltage at the output *6*, $y$ is proportional to the voltage across the capacitance $C$, and $\varphi(t)$ is proportional to the voltage across the resistor $R_3$ (Fig. 1a). This map relates the values of the variable at time $t$ with their values at time $t+\tau$, where $\tau$ is the delay time in the feedback loop. The values of the parameters $p$, $a$, and $c$ corresponded to the oscillator operating regimes and were 9, 0.6, and 0.4. It was found that for the type of signal studied, having only an $x$-component, and for numbers of cycles $T<10$, synchronization of any number of cycles can be achieved but the minimum amplitude of the synchronizing signal is obtained for $T=4$ and accounts for approximately 1/15 of the $x$-diameter of the attractor. The polarity of the optimum signal is negative.

For an experimental study of synchronization, we fed a pulsed synchronizing signal to the input *5* (Fig. 1a). The pulse may be considered to be short if its length is less than $1/f_c$, where $f_c$ is the cutoff frequency of the low-frequency filter. The delay time $\tau$ depends on the profile of the oscillations in the self-excited oscillator on account of the dispersion properties of the low-frequency filter.[6] The lower limit of $\tau$ is given by $\tau_1=\tau_0/\pi$, where $\tau_0=N/f_c$ ($N$ is the number of elements of the low-frequency filter). As a rule, exag-

gerated estimates of $\tau$ yield an average group delay $\tau_2 = \tau_0/2$. Thus, in our case, the pulse repetition frequency for synchronization of four-cycle stable fragments should lie in the range between 7 and 11 kHz.

The experiments in fact revealed synchronization at a pulse repetition frequency around 8.5 kHz and an amplitude around 0.3 V, which accounts for approximately 1/10 of the $x$-diameter of the attractor. Figure 2 shows the synchronization region on the frequency–amplitude plane of the synchronizing signal (a) and a trace of the synchronized oscillations (b). The pulse length is 10 $\mu$s and the polarity is negative. A small increase in the pulse length negligibly influences the synchronization process. The synchronization pattern is also conserved for decreasing pulse length, provided that the amplitude increases proportionately. A comparison between Fig. 1c and Fig. 2b indicates that fragments very similar to the trajectory of the synchronized oscillator do in fact exist on the trajectories of the autonomous oscillator.

The pulsed synchronization experiments also demonstrated that other regions of this type of synchronization also exist, but they have a higher synchronization threshold. There are also much broader regions of synchronization, where the pulses are not short but their amplitude is large. We treat this type of synchronization as strong-signal synchronization, for which the natural self-oscillating behavior of the system is suppressed and the periodic output process is simply the response of a stable nonlinear system to a periodic pulsed signal.

The synchronization by a weak, short, pulsed signal, as studied above, exhibits all the features characteristic of the synchronization of smooth maps:[2,3] upper and lower amplitude thresholds exist, transient chaos is observed at the onset of synchronization, and the synchronization is destroyed, via period doubling when the amplitude of the pulse signal increases, and abruptly when the amplitude increases. This type of synchronization only exists in a very narrow range of pulse repetition frequencies.

Finally, we note that if the signal shape is made more complex, i.e., if several short pulses of different polarity and amplitude are supplied within the repetition period rather than a single short pulse, the synchronization threshold may be reduced substantially. For instance, by selecting the polarity and amplitude of the partial signal pulses, we succeeded in reducing the synchronization threshold more than threefold in the particular case studied. The profile and amplitude of the synchronized oscillations remained the same, the dimensions of the synchronization region decreased proportionately, and the transient chaos time increased substantially.

This work was supported financially by the Russian Fund for Fundamental Research, Project No. 95-02-03633a.

[1] Yu. I. Neĭmark and P. S. Landa, *Stochastic and Chaotic Oscillations* [in Russian], Nauka, Moscow (1987).
[2] V. V. Rozhdestvenskiĭ, V. A. Potapov, and I. A. Shershnev, Radiotekh. Elektron. **39**, 814 (1994).
[3] V. V. Rozhdestvenskiĭ, Radiotekh. Elektron. **42**, No. 3 (1997).
[4] V. V. Rozhdestvenskiĭ and I. N. Struchkov, Zh. Tekh. Fiz. **62**(10), 100 (1992) [Sov. Phys. Tech. Phys. **37**, 1020 (1992)].
[5] V. V. Rozhdestvenskiĭ and I. N. Struchkov, Izv. Vyssh. Uchebn. Zaved. Prikl. Nelin. Dynam. **1**(1–2), 83 (1993).
[6] L. A. Vaĭnshteĭn, Usp. Fiz. Nauk **118**, 339 (1976) [Sov. Phys. Usp. **19**, 189 (1976)].

Translated by R. M. Durham

# Production of wavelength-selective, time-resolved, x-ray images of a neon plasma in the SPEED 2 plasma focus

S. V. Bobashev, D. M. Simanovskiĭ, G. Decker, W. Kies, P. Röwekamp, Kh. Zol', and U. Berntin

*A. F. Ioffe Physicotechnical Institute, Russian Academy of Sciences, St. Petersburg; Heinrich-Heine-University, Düsseldorf, Germany*
(Submitted December 27, 1996)
Pis'ma Zh. Tekh. Fiz. **23**, 53–59 (April 26, 1997)

The dynamics of pinching of a neon plasma in the SPEED 2 facility has been investigated by recording wavelength-selective, x-ray images of the plasma with good space and time resolution. A series of images of the plasma focus was obtained on the $\lambda = 1.21$ nm and $\lambda = 1.35$ nm emission lines of hydrogen- and helium-like ions at various stages of plasma compression. The stable nature of the discharge in a neon plasma was confirmed. It was established that at the final stage of pinching, the charge of the neon ions increases rapidly from $+9$ to $+10$, and when the pinch diameter is less than 1 mm, the plasma is completely ionized.
 [S1063-7850(97)02604-9]

The ion composition of a neon plasma in the SPEED 2 facility has been investigated by recording time-resolved x-ray images of the plasma on emission lines of hydrogen- and helium-like neon lines.

The SPEED 2 facility is a powerful electric driver designed to generate and compress a plasma having a ''plasma focus'' configuration. The facility has a current rise time (quarter period) $\tau = 400$ ns and a maximum discharge current of 2 MA with an initial voltage up to 300 kV (Ref. 1). SPEED 2 was initially designed for fusion research and was intended to operate with a deuterium plasma. It has recently been demonstrated that this facility may be used to generate x-rays by injecting rare gases into the anode region of a deuterium discharge. As a result of dynamic compression of the injected gas by a compressive deuterium sheath, a highly ionized dense plasma, which is an intense source of soft x-rays, is formed at the final stage of the discharge.[2]

Discharges doped with argon and neon have been investigated in SPEED 2. It was observed that the pinching dynamics and the spatial structure of the resultant dense plasma differ substantially for Ar and Ne discharges.

In argon-doped discharges established at typical voltages of 180 kV and a maximum current of 1.5 MA, strong Rayleigh–Taylor instability ($m = 0$) was observed to develop at the final stage of dynamic compression, resulting in the formation of so-called micropinches caused by radiative collapse.[3,4] It was also established in Ref. 2, that a considerable fraction of the x-rays emitted by the plasma (some tens of joules) is accounted for by these micropinches.

A different pattern was observed in neon-doped discharges, for which a stable homogeneous pinch without any signs of radiative collapse was typically formed. This behavior may be explained by the fact that at the final compression stage, the neon becomes completely ionized (to bare nuclei), which reduces the rate of radiative losses and thereby prevents the evolution of radiative collapse and micropinch formation.

To check out this hypothesis and to determine the spatial distribution of the Ne ions in the plasma at the final compression stage, we recorded images of the plasma in emission lines of hydrogen- and helium-like neon ions, corresponding to the $1s-2p$ ($\lambda = 1.21$ nm) transition in the $Ne^{10+}$ ion and the $1s^2-1s2p$ ($\lambda = 1.35$ nm) transition in $Ne^{9+}$. A time-gated image detector was used to obtain images corresponding to different phases of plasma compression.

An x-ray system consisting of a parallel configuration of cylindrical multilayer x-ray mirrors was used to construct the plasma images.[5] The optical system of the apparatus connected to the experimental facility is shown in Fig. 1. The principal optical element is a rotating multilayer mirror assembly, which is used to focus and monochromatize the radiation. The focusing properties of this system, in which radiation is successively reflected by two closely spaced mirrors that are curved cylindrically along the radii $R1$ and $R2$ in mutually perpendicular planes, are almost equivalent to the focusing properties of a single spherical mirror. The first cylindrical mirror focuses the radiation in the meridional plane while the second focuses it in the saggital plane. The main advantage of this configuration of optical elements is that the working wavelength can be varied smoothly by rotating the focusing element about its axis.

The distance between the cylindrical mirrors, 1.6 cm, was much shorter than the focal length of the system $-F = 50$ cm. This relationship allowed us to use simplified formulas from Ref. 6 to determine the radii of curvature of the mirrors:

$$R1 = 2F/\sin\vartheta, \tag{1}$$

$$R2 = 2F\sin\vartheta, \tag{2}$$

where $F$ is the focal length of the system and $\vartheta$ is the angle of incidence of the radiation on the mirror. Multilayer W–Sc x-ray mirrors with a structure period $d = 1.18$ nm, deposited on $0.5\times 20\times 50$ mm silicon substrates, were developed at the Institute of Microstructure Physics of the Russian Academy of Sciences, for the $1.21-1.35$ nm wavelength range. The reflection coefficient of a single mirror at these wavelengths

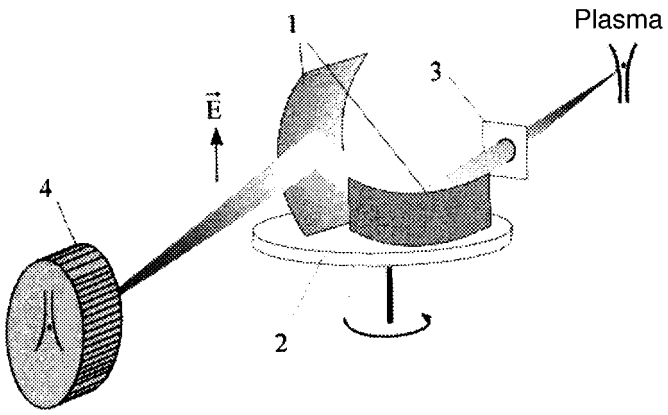


FIG. 1. Optical system of imaging apparatus connected to experimental facility: *1* — cylindrical multilayer x-ray mirrors, *2* — rotating mirror assembly, *3* — filter, and *4* — image detector.

was 0.7%. The spectral resolution after two reflections was $\lambda/\Delta\lambda \approx 150$, so that the spectral lines of hydrogen- and helium-like neon ions could be reliably separated. The working range of angles of incidence of the radiation on the multilayer x-ray mirrors was $31-35°$. For these angles of incidence, the radii of curvature of the mirrors determined according to formulas (1) and (2), were $R1 \approx 1.8$ m and $R2 \approx 0.5$ m, respectively.

The distance between the focusing mirrors *1* and the plasma was 1.2 m (Fig. 1). Such a large distance was needed to protect the vacuum-tight filter *3*, separating the imaging system and the discharge chamber, from the action of the shock wave and the radiation. The filter was made of 1.5 $\mu$m thick polyethylene terephthalate film (Makrofol KD) coated with 0.15 $\mu$m thick layers of aluminum foil on both sides. The filter was needed to protect the detector from the soft vacuum ultraviolet discharge radiation, which could be reflected nonselectively by the multilayer x-ray mirror. The filter was also required to separate the high-vacuum chamber of the imaging system ($10^{-5}$ Torr) from the discharge chamber, filled with deuterium to a pressure of $3-4$ Torr.

Images of the plasma were recorded using a time-gated microchannel plate detector *4*. A voltage pulse of 5 kV amplitude and 3 ns duration was applied to the microchannel detector to obtain an image at a specific time. The voltage was divided between the chevron assembly of the microchannel plates (1.5 kV) and an accelerating gap in front of a phosphor screen (3.5 kV) deposited on a fiber-optic plate. The image, converted into visible light, was recorded on high-sensitivity Fuji Neopan 1600 film clamped directly to the surface of the fiber-optic plate.

The spatial resolution achieved by the imaging system was primarily determined by the aberrations of the focusing optics and the resolution of the detector. The experimentally determined resolution was 80 $\mu$m. In many cases, where plasma images were recorded using weak emission lines, the actual resolution was lower and was determined by the statistical nature of the images.

The main difficulty encountered in the measurements was that the time spread of the pinching time, around 50 ns, was several times greater than the time window of the detector (3 ns) and the lifetime of the dense plasma ($\sim$15 ns). In a series of experiments using this imaging system, involving more than 100 discharges, we obtained around twenty successful photographs of a neon plasma at various stages of compression on the 1.21 and 1.35 nm lines. For all the discharges the initial driver voltage was 180 kV and the stored energy was 70 kJ.

A series of plasma images obtained at 1.35 nm ($1s^2-1s2p$, $Ne^{9+}$) was used to study the dynamics of the pinching, which was initiated near the anode surface and then evolved along the $Z$ axis. A typical photograph of the plasma at the instant of maximum luminosity near the anode is given in Fig. 2a. The results indicate that the pinching process propagates along the $Z$ axis from the surface of the anode at a velocity of $\sim 10^8$ cm/s and the plasma radiation at

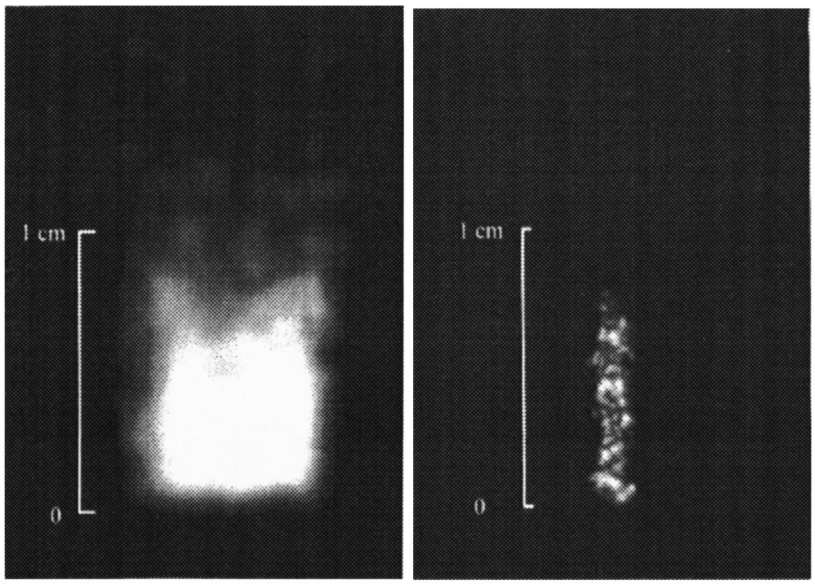


FIG. 2. Image of a neon plasma at the wavelengths: a — 1.35 nm and b — 1.21 nm.

the given wavelength is reliably recorded at distances up to 3 cm from the anode surface. Moreover, the length of the emitting region of the pinch did not exceed 1 cm at any time and its diameter was at least 4 mm. An emitting zone of such large diameter indicates that the plasma attains a degree of ionization characterized by a fairly high concentration of helium-like ions at a fairly early stage of pinching. As the plasma undergoes further compression and heating, the concentration of helium-like ions drops, as is evidenced by the absence of their radiation from a plasma of less than 3 mm diameter.

The plasma images at 1.21 nm ($1s-2p$, $Ne^{10+}$) reveal that the diameter of the plasma pinch with a high concentration of hydrogen-like ions is around 1 mm. This indicates that as the plasma is compressed from 4 to 1 mm, the average charge of the plasma ions increases from $Ne^{9+}$ to $Ne^{10+}$, and as a result of further compression, the plasma becomes completely ionized, containing $Ne^{11+}$ nuclei and free electrons.

These results support the hypothesis that the rate of radiative losses of a neon plasma decreases under severe compression because the plasma becomes completely ionized. The proposed method of obtaining plasma images will be used for further studies of the mechanism of stable pinching, resulting in the formation of a spatially homogeneous dense plasma.

The authors would like to thank N. N. Salashchenko for supplying these unique x-ray mirrors. The work was made possible by NATO Grant CRJ950937.

[1] G. Decker, W. Kies, M. Malzig, C. van Calker, and G. Ziethen, Nucl. Instrum. Methods Phys. Res. A **249**, 477 (1986).
[2] Yu. Ya. Platonov, N. N. Salashchenko, D. M. Simanovskii, P. Roewekamp, G. Decker, and W. Kies, *Short Living Plasma and Its Diagnostics* (Prague, 1995), pp. 122–127.
[3] G. Decker, W. Kies, R. Nadolny, P. Röwekamp, F. Schmitz, G. Ziethen, K. N. Koshelev, Yu. V. Sidelnikov, and Yu. V. Sopkin, Plasma Sources Sci. Technol. **5**(1), 112 (1996).
[4] K. N. Koshelev and N. R. Pereira, J. Appl. Phys. **69**, R21 (1996).
[5] S. V. Bobashev, D. M. Simanovskii, Yu. Ya. Platonov, P. Röwekamp, G. Decker, and W. Kies, Plasma Sources Sci. Technol. **5**(3), 578 (1996).
[6] T. Chen, V. A. Bushuev, and R. N. Kuz'min, Zh. Tekh. Fiz. **60**(10), 60 (1990) [Sov. Phys. Tech. Phys. **35**, 1148 (1990)].

Translated by R. M. Durham

# Ion charge-state distribution in a high-power pulsed electron cyclotron resonance discharge sustained by millimeter-wavelength radiation

S. V. Golubev, V. G. Zorin, and S. V. Razin

*Institute of Applied Physics, Russian Academy of Sciences, Nizhniĭ Novgorod*
(Submitted October 28, 1996)
Pis'ma Zh. Tekh. Fiz. **23**, 60–64 (April 26, 1997)

Measurements have been made of the ion charge-state distribution in a high-power, pulsed, electron-cyclotron discharge in argon sustained by millimeter radiation. It has been observed that the maximum of the distribution is shifted toward higher charge states compared with the distributions in conventional cw sources of multiply charged ions pumped by centimeter radiation. This shift of the distribution maximum evidently occurs because a so-called quasigasdynamic plasma confinement regime can be established in a magnetic trap when higher-power, shorter-wavelength gyrotron radiation is used, and in this regime, an increase in plasma density is accompanied by an increase in the confinement parameter $N_\tau$, which determines the ion charge distribution. © *1997 American Institute of Physics.* [S1063-7850(97)02704-3]

The most promising sources of multiply charged ions at the present time are those utilizing a microwave discharge plasma sustained in an open magnetic trap under electron cyclotron resonance conditions. These sources are primarily designed for injection of ions in cyclotron accelerators, whose operating efficiency is, in many respects, determined by the operating efficiency of the ion source (Ref. 1).[1)]

For its part, the operating efficiency of these sources can be substantially enhanced, i.e., the charge state and intensity of the ions beams can be increased, by increasing the microwave pump frequency. This line of research was pursued following the publication of a series of experimental studies (see, for example, Ref. 5), in which a substantial increase in the yield of multiply charged ions was demonstrated when the pump frequency was increased from 10 to 18 GHz — the ion current with the charge averaged over the distribution increased proportionately as the square of the pump frequency ($f^2$). However, the ion charge distribution remained almost the same (Fig. 1). In terms of elementary concepts, this behavior may be explained as follows. As the microwave pump frequency is increased, the plasma density $N$ increases while the plasma losses caused by Coulomb collisions increase proportionately as $N$ (the plasma lifetime in the trap is $\tau \sim 1/N$). In this case, at the optimum electron energy, the ion charge distribution determined by the confinement parameter $N\tau$ remains unchanged, but if $N \sim f$, the multiply charged ion current, determined by the parameter $N/\tau$, will be proportional to $f^2$. This reasoning stimulated increased interest in studies of an electron cyclotron resonance discharge sustained by high-frequency radiation, since the multiply charged ion current should increase accordingly. In addition, the millimeter radiation of modern gyrotrons may well produce an increase in the plasma density, which will change the nature of the plasma confinement in the trap — a so-called quasigasdynamic plasma confinement regime will be established,[6] where the plasma lifetime depends weakly on its density.[2)] The establishment of this regime will not only increase the intensity of the multiply charged ion beams but, more importantly, will increase the parameter $N\tau$, which should substantially shift the ion charge distribution toward higher degrees of ionization. In the present paper, we report the first experimental data on the ion charge-state distribution in a high-power pulsed electron cyclotron resonance discharge sustained by short-wavelength gyrotron radiation. The apparatus is shown schematically in Fig. 2. Microwave radiation from a pulsed gyrotron *1*, having a frequency of 37.5 GHz, a pulse length of 1 ms, and a power of 130 kW, was focused by a dielectric lens *2* into a discharge vacuum chamber *3*. The beam is linearly polarized. The discharge chamber, having a 70 mm diameter entrance window, was inserted in a straight magnetic trap created by two solenoids (the length of the magnetic field pulse was $\approx$13 ms). The length of the trap was 25 cm and the mirror ratio was 3.2. The maximum magnetic field strength in the mirror was 2.3 T. To estimate the plasma density in the discharge, we measured the coefficient of transmission of diagnostic microwave radiation by the plasma (*4* and *5*). The diagnostic microwave radiation at a frequency of 35.52 GHz, whose polarization corresponded to the ordinary wave, was injected into the center of the trap perpendicular to the magnetic field. Ions escaping the plasma parallel to the magnetic field were analyzed using a two-stage (magnetic and electrostatic) ion analyzer *6*, capable of making independent measurements of the ion energy and their charge-to-mass ratio with a resolution $(q/m)[\Delta(q/m)]^{-1}=3$. The analyzer (the analyzing magnet current) was calibrated using hydrogen ions. The analyzer was connected to the discharge chamber via a connecting section *7*. The working gas (argon) pressure was set by means of a pulsed flow regulator and was varied between $10^{-3}$ and $10^{-5}$ Torr, with gas being admitted into the discharge chamber (Fig. 2), while a low pressure of $\sim 10^{-6}$ Torr was maintained in the analyzer and in the connecting section. A distinguishing feature of these experiments was that the multiply charged ion generation efficiency was investigated at fairly high plasma densities, an order of magnitude higher than those in conventional electron cyclotron resonance sources of multiply charged ions. In the experiments we observed total screening of the diagnostic and high-power microwave radiation by the discharge, which suggests that a plasma having a density higher than

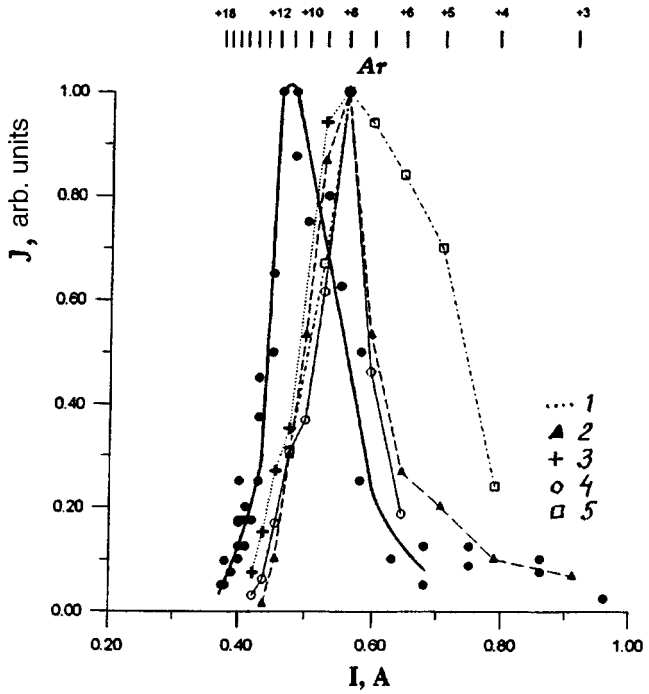


FIG. 1. Signal from ion analyzer versus analyzer magnet current. The graduation lines in the upper part of the figure show the magnet currents corresponding to argon ions of different charge (*1* — our experimental results, *2* — data from Ref. 5, *3* — Ref. 8, *4* — Ref. 9, and *5* — Ref. 10.)

$4\times10^{13}$ cm$^{-3}$ is formed under our conditions.

The efficiency of generation of the multiply charged ions and their energy depended strongly on the gas pressure and the microwave radiation power. At an optimum gas pressure ($\sim10^{-4}$ Torr), the energy of the argon ions escaping the plasma was between 100 eV and 10 keV. The charge distribution of the ions depended weakly on their energy. Figure 1 shows the signal from the ion analyzer as a function of the analyzing magnet current, which describes the ion charge distribution for 900 eV ions. Also plotted for comparison are the ion charge distributions obtained in conventional cw electron cyclotron resonance sources of multiply charged ions pumped by centimeter radiation (between 6 and 18 GHz) (Refs. 5 and 8–10). It can be seen that the distribution obtained in our experiments is shifted toward higher degrees of ionization (the maximum is obtained for an ion charge of 11–12, as compared to 8 in conventional sources).

It is therefore postulated that the use of higher-power, shorter-wavelength gyrotron radiation resulted in the establishment of a quasigasdynamic plasma confinement regime, where the parameter $N\tau$ was increased and the ion charge distribution was shifted toward higher degrees of ionization.

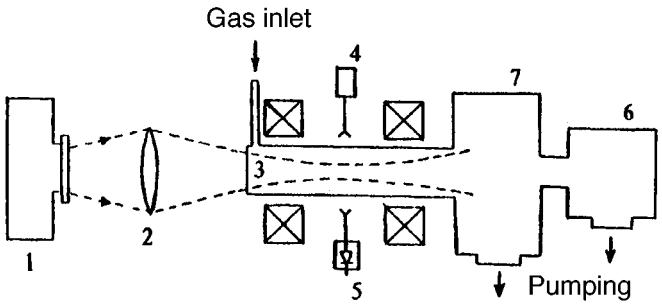


FIG. 2. Schematic diagram of experiment.

[1)] In addition, an electron cyclotron resonance discharge is also considered to be a possible source of soft incoherent x-rays.[2–4]

[2)] In the quasigasdynamic confinement regime of a dense plasma with magnetized collisionless electrons and cold ions, where the main electron loss channel is loss-cone scattering during interaction with the resonant microwave pump radiation, the plasma lifetime is given, according to Ref. 7, by $\tau\sim LK/V$, where $L$ is the characteristic dimension of the trap, $V$ is the ion sound velocity, and $K$ is a coefficient which depends weakly on the plasma density.

[1] R. Geller, J. Phys. (Paris) **50**, Colloq. C1, 887 (1989).
[2] J. H. Booske, F. A. Aldabe, R. F. Ellis, and W. D. Getty, J. Appl. Phys. **64**, 1055 (1988).
[3] Y. Arata, S. Miyake, H. Kishimoto, N. Abe, and Y. Kawai, Jpn. J. Appl. Phys. **27**, 1281 (1988).
[4] S. V. Golubev, V. G. Zorin, Yu. Ya. Platonov, and S. V. Razin, Pis'ma Zh. Tekh. Fiz. **20**(4), 7 (1994) [Tech. Phys. Lett. **20**, 135 (1994)].
[5] R. Geller, B. Jacquot, and P. Sortais, Nucl. Instrum Methods Phys. Res. A **243**, 244 (1986).
[6] S. V. Goludev, V. G. Zorin, T. N. Zorina, and S. V. Razin, Proc. Intern. Workshop on Strong Microwaves in Plasmas, Nizhniĭ Novgorod, 1991, Vol. 1, pp. 485–489.
[7] S. V. Golubev, V. E. Semenov, E. V. Suvorov, and M. D. Tokman, Proc. Intern. Workshop on Strong Microwaves in Plasmas, Nizhniĭ Novgorod, 1991, Vol. 1, pp. 347–375.
[8] H. Beuscher, Rev. Sci. Instrum. **61**, 262 (1990).
[9] T. A. Antaya and S. Gammino, *Proceedings of the International Workshop on Strong Microwaves in Plasmas, Nizhniĭ Novgorod*, 1991, Vol. 1, pp. 399–413.
[10] G. G. Gul'bekyan, I. V. Kolesov, V. V. Bekhterev *et al.*, Kratk. Soobshch. OIYaI, No. 4(72)-95, 63 (1995).

Translated by R. M. Durham

# Laser multipass probing in Thomson plasma diagnostics

M. Yu. Kantor and D. V. Kuprienko

*A. F. Ioffe Physicotechnical Institute, Russian Academy of Sciences, St. Petersburg*
(Submitted December 27, 1996)
Pis'ma Zh. Tekh. Fiz. **23**, 65–72 (April 26, 1997)

A new approach to a system of laser probing for Thomson diagnostics of a high-temperature plasma is proposed. The approach is based on the principles of multipass intracavity laser probing, which can improve the sensitivity of the method by between one and two orders of magnitude and allows the electron temperature to be measured at frequencies higher than 10 kHz. Results of testing a probing system developed for the FT-2 tokamak are presented.
 [S1063-7850(97)02804-8]

## 1. INTRODUCTION

The Thomson diagnostic technique is widely used to measure the local electron temperature of a hot plasma. At plasma densities higher than $10^{13}$ cm$^{-3}$, this technique offers extensive scope, including measurements of the evolution of the spatial temperature profiles. At lower densities, this diagnostic technique encounters appreciable difficulties because of the low scattered radiation energy. Nevertheless, there is no viable alternative under these conditions, since other methods do not provide reliable data on account of the distortions of the electron distribution function. Measurements of the temperature evolution of a low-density plasma pose additional problems. Lasers with a pulse repetition frequency of some tens of kilohertz are required because of the fast nature of the transient processes under these conditions. Even in dense plasmas, a high sensitivity is needed to measure the electron distribution function or the plasma current density[1], as well as the electron temperature profiles, by means of a single spectral device.

In the present paper we propose a new approach to Thomson diagnostics, based on the principles of multipass intracavity probing, whereby the sensitivity of the method can be improved by more than an order of magnitude, and electron temperature measurements can be made at frequencies around 10 kHz. In multipass probing, the laser beam repeatedly passes through the volume under study, which enhances the sensitivity of the diagnostics because of the increase in the scattered radiation energy. After passing through the plasma volume, the beam is returned to the laser active elements. Thus, the plasma volume is contained within the laser cavity, which substantially reduces the radiation losses in the system. This effect cannot be used to achieve any significant increase in the pulse radiation energy (this is usually close to the maximum permissible value). However, the effect can extend the capabilities of the laser, particularly under multipulse lasing. We present results of an experimental study of a new probing system developed on these principles for Thomson diagnostics of the FT-2 tokamak plasma.

## 2. OPTICAL SYSTEM FOR MULTIPASS INTRACAVITY LASER PROBING

The laser optical system used for Thomson diagnostics must be revised for intracavity probing. The usual multistage system (oscillator and amplifier) is less effective here because the returned beam is forced to pass through the laser oscillator, which is not only unable to sustain the beam energy but also cannot maintain its high intensity. In this case we need to dispense with a multistage system and use a single active element to generate the radiation. The stored inversion can be efficiently converted into laser radiation with low radiation losses in an extended laser cavity. A similar system was used for the first time in the FT-1 tokamak.[2] An optical system for multipass, intracavity laser probing is shown in Fig. 1.

A cavity formed by a nontransmitting mirror *1* and the mirrors *6* and *7* of the multipass system is Q-switched by a phototropic filter *4*. Possessing a high initial absorption, this filter can sustain a fairly high inversion in the active medium. The avalanche-like bleaching of the filter under the action of the spontaneous radiation generates a high-power laser pulse, which can be repeated many times during a single discharge of the flashlamps.

The multipass system is the key factor in the new approach. A system designed to pass a beam many times through a plasma, whereby the beam is focused on the observation axis and then returned to the laser, was proposed in Ref. 3 and used on the FT-1 tokamak.[4] The system consists of two spherical mirrors *6* and *7*, between which is located a plasma volume *8*, and a lens *5* to focus the radiation on the observation axis. The mirrors are separated by a distance equal to the sum of their radii of curvature. The maximum number of passes of the beam $N \equiv 8D/b$ in the system is achieved by moving the centers of curvature of the mirrors relative to each other by $b^2/16D$ along the observation axis. Here, $b$ is the diameter of the input beam and $D$ is the mirror diameter along the observation axis. The divergence of the beam should not exceed $b/2NF$, where $F$ is the focal length of the lens, otherwise an increase in the transverse dimensions of the beam will result in losses of radiation from the system. Stringent constraints on the divergence of the radiation may seriously limit the application of multipass probing in plasma experiments.

These constraints may be eased by specially aligning the multipass system and introducing measures to reduce the beam divergence. This alignment essentially involves optimizing the position of the mirrors and the lens. A small relative shift of the mirrors converts the multipass system

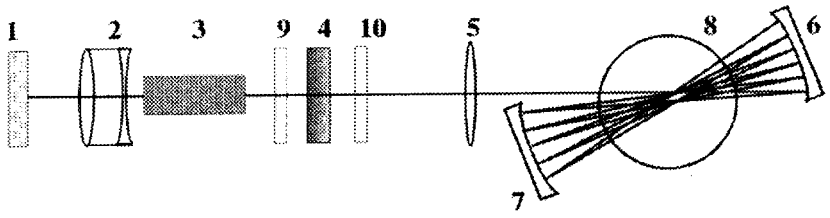


FIG. 1. Optical system for multipass, intracavity laser probing: *1* — 100% cavity mirror, *2* — objective, *3* — laser active element, *4* — phototropic filter, *5* — focusing lens, *6, 7* — mirrors of multipass system, and *8* — plasma volume.

into a set of stable optical cavities capable of confining diverging beams. The magnitude of the shift is dictated by the need to confine the beams in the system and prevent them from being focused near the surface of the mirrors. In this case, the divergence of the laser beam plays a decisive role. The methods usually used to reduce divergence are not suited to intracavity probing. To solve this problem, we inserted an objective *2* into the cavity to correct the optical inhomogeneity of the active element *3*, which substantially reduced the divergence. These aspects will be examined in a separate study.

In cases of low radiation losses, these elements are sufficient for lasing. For additional control of the laser, it may be useful to have an auxiliary cavity formed by placing one or two semitransmitting mirrors *9* and *10* with low reflection coefficients near the active element and the phototropic filter. In cases of high radiation losses, this cavity is needed to shape the initial pulse.

### 3. EXPERIMENTAL RESULTS

A ruby rod 240 mm long and 21 mm in diameter, having a $Cr_2O_3$ impurity concentration of 0.012 %, was used in the probing system. The crystal aperture was limited by a 16 mm diaphragm. The phototropic filter consisted of KC-19 tinted glass with CdSe impurities. The multipass system was formed by two mirrors, having 1000 mm radii of curvature and diameters of 120 mm, and a lens of 1250 mm focal length, positioned 3 m from the crystal. Apart from the ends of the ruby, the surfaces of all the optical elements had antireflection coatings.

An objective, consisting of positive ($F=1250$ mm) and negative ($F=-1500$ mm) lenses, was mounted between the active element and the nontransmitting mirror *1*. By selecting the focal length of the objective, the beam divergence was reduced from 6 to 1 mrad and the threshold laser pump energy was almost halved. Up to 36 passes of the beam through the system could be achieved by shifting the mirrors by 10 mm relative to each other. The constriction of the fan of rays on the observation axis measured $2\times12$ mm and the output beam was matched with the aperture of the active element.

The system was studied with two IKT-1M and IKT-1N radiation energy meters and an FÉK-1 coaxial photocell, which measured the lasing power. One of the meters determined the energy of the forward beam leaving the active element and the other measured the energy of the return beam, returning from the multipass system to the laser. These measurements were then used to determine the probing energy. The signal from the FÉK-1 photocell was digitized by six seven-digit analog-to-digital converters operating at 10–40 MHz.

After 28–30 passes of the beam, up to 80% of the radiation was returned from the multipass system to the crystal, which corresponds to an increase in the probing energy by a factor of 25–27. In this case, the effective length of the laser cavity is around 70 m. Two phototropic filters with initial transmissions of 55% and 70% were used to control the system. With the first filter, most of the stored inversion is used to generate the pulse, which increases the radiation energy and power in the pulse. This is accompanied by a reduction in the pulse repetition frequency and in the number of pulses. Trains of probe pulses obtained with the 70% and 55% filters are shown in Fig. 2. In both cases, the total probing energy exceeds 1500 J. The average radiation energy in the pulses is 50 and 115 MW, respectively. The pulse energy and power, as well as the number of pulses can be varied by means of the pumping and the filters (Fig. 3). The pulse repetition frequency is mainly determined by the filter transmission, and decreases slightly with decreasing pumping. It can be seen from the figures that with the 70% filter, the laser delivers a train of twenty lasing pulses at a repetition frequency up to 15 kHz.

On account of the great cavity length, the length of the laser pulses is $1-2$ $\mu$s, which is unusual for Thomson diagnostics. Nevertheless, the probing power is quite sufficient for the scattering signal to exceed the background plasma

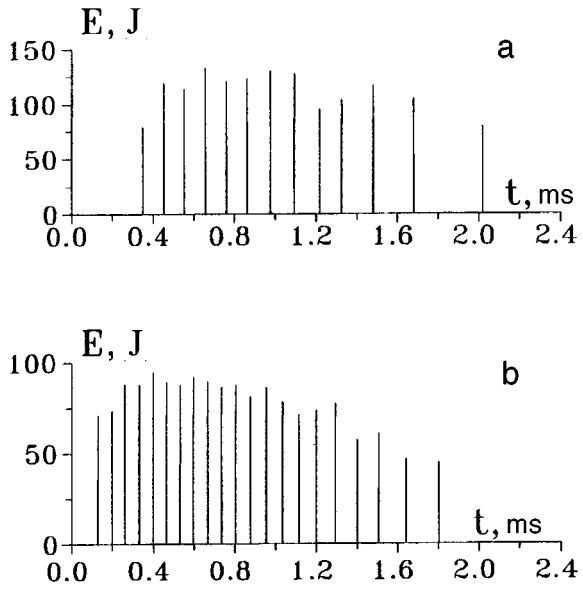


FIG. 2. Multipulse lasing: a — 55% filter, b — 70% filter.

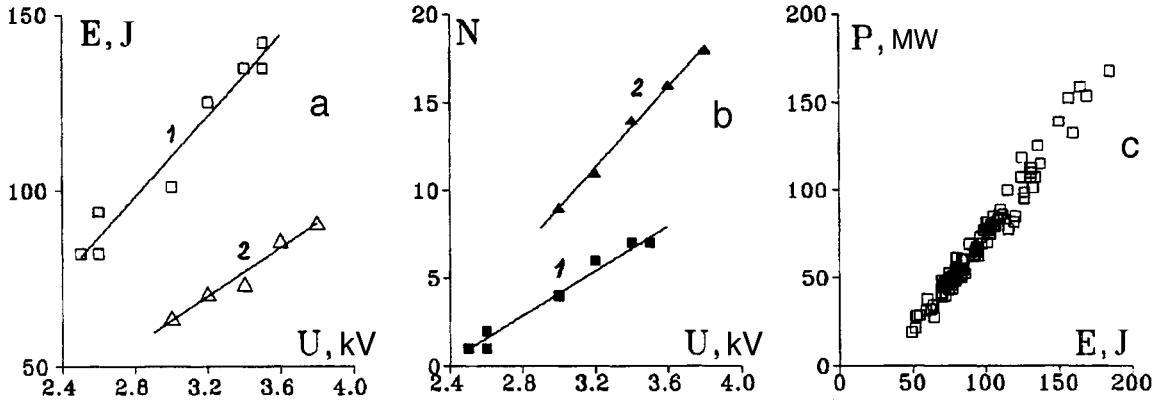


FIG. 3. a — Laser pulse energy versus pumping: *1* — 55% filter, *2* — 70% filter; b — number of lasing pulses versus pumping, *1* — 55% filter, *2* — 70% filter; c — power versus energy of probe laser pulse.

radiation. Measurements of the plasma luminescence showed that this is correctly subtracted in Thomson measurements at these signal durations.

In these experiments, the probing energy and power were limited by the fact that the pulse energy density at the active element should not exceed 5 J/cm$^2$ per pulse. Even with this constraint however, the new system gives an approximately twentyfold increase in the probing energy in each pulse as compared with the conventional system. It can also be used for repeated measurements at frequencies up to 15 kHz. The accumulation of signals from all the pulses in the lasing train can enhance the sensitivity of the Thomson diagnostics approximately 300 times. By using an element with a higher maximum permissible energy density, the probe pulse may be additionally amplified by means of the pumping and by installing a denser phototropic filter.

This work was supported by the Russian Fund for Fundamental Research, Grant No. 95-02-04072.

[1] A. C. A. P. van Lammeren, C. J. Barth, Q. C. van Est *et al.*, Nucl. Fusion **32**, 655 (1992).
[2] M. Yu. Kantor and G. T. Razdobarin, Proc. Sixth Intern. Symposium on Laser Aided Plasma Diagnostics, Bar Harbor, 1993, p. 267.
[3] V. K. Gusev, M. Yu. Kantor, and G. T. Razdobarin, Author's Certificate No. 1421072, Otkr. Izobret. No. 8, 286 (1990).
[4] T. Yu. Akatova, D. G. Bulyginskiĭ, V. M. Zavadskiĭ *et al.*, Fiz. Plazmy **18**, 166 (1992) [Sov. J. Plasma Phys. **18**, 89 (1992)].

Translated by R. M. Durham

# Influence of charge flow along a semiconductor surface on the nature of the multiplication coefficient in a silicon–wide-gap layer structure

Z. Ya. Sadygov and T. V. Jejer

*Joint Institute of Nuclear Research, Dubna*
(Submitted December 11, 1996)
Pis'ma Zh. Tekh. Fiz. **23**, 72–76 (April 26, 1997)

It has been shown that the flow of mobile minority carriers along the semiconductor–wide-gap layer interface substantially influences the uniformity of the multiplication coefficient in an avalanche photodetector. Around inhomogeneities in the semiconductor substrate, a ''dead zone'' of fairly large area is formed, where the multiplication coefficient is several orders of magnitude lower than that on the remaining area of the device. Specific methods are proposed to improve the uniformity of the avalanche process in a semiconductor–wide-gap layer structure.
 [S1063-7850(97)02904-2]

The feasibility of developing a new type of avalanche photodetector utilizing silicon heterostructures has recently been discussed quite extensively. Layers of $SiO_2$ (Refs. 1–3), SiC (Refs. 4 and 5), and other materials whose band gap is greater than that of silicon, are usually used as the wide-gap layer. In silicon heterostructures a local increase in the avalanche current increases the mobile charge accumulated at the semiconductor–wide-gap layer interface, which screens the electric field in the semiconductor region with reduced breakdown potential. Thus, negative feedback is established between the multiplication coefficient of the avalanche process and the voltage drop in the semiconductor.

However, a nonuniform distribution of the surface mobile charge density leads to the appearance of longitudinal electric fields which cause these mobile charges to spread out by flowing along the semiconductor–wide-gap layer interface. In the present paper we investigate the influence of this charge flow on the multiplication coefficient in silicon heterostructures, for various resistances of the wide-gap layer.

We consider a silicon heterostructure in which avalanche charge multiplication takes place under the action of an applied voltage. By generation we understand the avalanche multiplication of charge carriers, and by recombination we understand the drift of these carriers into contacts via the wide-gap layer. Under certain conditions, the rate of carrier generation in the semiconductor exceeds their recombination, resulting in a buildup of minority carriers at the semiconductor–wide-gap layer interface, which screens the electric field in the avalanche region of the semiconductor.

The charge flow equation can be obtained from the well-known equation of continuity for the total current in the depleted layer of a semiconductor.[6] After integrating this equation of continuity over the thickness of the inversion layer, assuming that there is no current diffusion component, we derive the following charge flow equation:

$$I_a - I_0 - \nabla_s I_s = \frac{\partial \sigma}{\partial t},$$

$$I_s = -\mu \sigma \nabla_s \psi_s, \tag{1}$$

where $\sigma = \int_0^\delta \rho(x,y,z)dz$ is the surface charge density, $I_s = \int_0^\delta J(x,y,z)dz$ is the current component along the surface, $I_a$ is the avalanche current in the semiconductor, $I_0$ is the leakage current of the wide-gap layer, and $\nabla_s$ is the gradient operator along the surface. The avalanche current $I_a$ in the photodetector is determined by the well-known Miller formula[7] linking the carrier multiplication coefficient $M$ with the surface potential of the semiconductor, and the leakage current $I_0$ may be determined by assuming for simplicity that the conductivity of the wide-gap layer is purely ohmic. Thus, we have:

$$I_a = i_a M = \frac{i_a}{1-(\psi_s/\psi_0)^m},$$

$$I_0 = \frac{V_0}{R_0}, \tag{2}$$

where $i_a$ is the avalanche-inducing current, $\psi_0$ is the breakdown potential of the semiconductor surface, $m$ is an empirical parameter having values between 1 and 5, and $R_0$ is the resistance of a wide-gap layer of unit area.

Using the well-known solution of the Poisson equation, we can derive the following relation between the surface potential and the surface mobile charge density for a semiconductor–wide-gap layer structure:[7]

$$\psi_s = u_0 + \left(V - \frac{\sigma}{C}\right) - \sqrt{u_0\left[2\left(V - \frac{\sigma}{C}\right) + U_0\right]}, \tag{3}$$

where

$$u_0 = \frac{\varepsilon q N}{C^2},$$

$q$ is the electron charge, $N$ is the impurity concentration in the semiconductor, and $C$ is the specific capacitance of the wide-gap layer.

We now assume that on the surface of the photodetector substrate there is a single region of radius $r_0$, within which the breakdown potential is lower than that of the rest of the device. We position our origin at the center of a circle of radius $r_0$, where $\psi_0 = \psi_{01}$ for $r \leqslant r_0$, and $\psi_0 = \psi_{02} > \psi_{01}$ for $r > r_0$. Taking into account the symmetry of the problem, we shall use polar coordinates. Then, under steady-state conditions, Eqs. (1), (2), and (3) yield the following equations for the surface potential:

 1063-7850/97/040324-02$10.00  

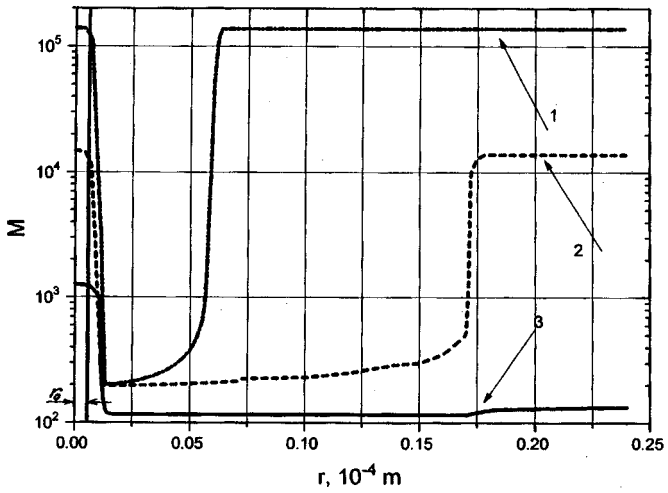


FIG. 1. Multiplication coefficient as a function of the coordinate on the surface of a silicon–wide-gap layer avalanche structure with $V=53.8$ V, $r_0=10$ $\mu$m, $N=1.5\times10^{16}$ cm$^{-3}$, $d=0.1$ $\mu$m, $m=2$, $i_a=10^{-3}$ A/m$^2$, $\mu=0.05$ m$^2$/s·V$^2$, $\Psi_{01}=39.9$ V, $\Psi_{02}=40.0$ V. *1* — $R_0=0.1$ $\Omega\cdot$m; *2* — $R_0=1$ $\Omega\cdot$m, and *3* — $R_0=50$ $\Omega\cdot$m.

$$\frac{I}{r}\frac{\partial}{\partial r}(rI_s)=\frac{i_a}{1-(\psi_s/\psi_0)^m}-\frac{V-\psi_s}{R_0},$$

$$I_s=-\mu C(V-\psi_s-\sqrt{2u_0\psi_s})\frac{\partial\psi_s}{\partial r}. \qquad (4)$$

By solving Eq. (4) with allowance for expression (2), we can study the behavior of the multiplication coefficient along the surface of the avalanche photodetector. Results of calculations of the avalanche multiplication coefficient as a function of the coordinate on the plane of the avalanche photodetector are plotted in Fig. 1. It can be seen that the avalanche multiplication coefficients inside the circle of radius $r_0$ and at some distance from this circle, have almost the same values, despite the different breakdown coefficients in these regions. This is accomplished by the buildup of mobile charge within the region of radius $r_0$, which screens the electric field in this region of the semiconductor. However, flow of this charge outside this region of radius $r_0$ ''suppresses'' the avalanche process in this region. The influence of the mobile charge extends as far as the distance from which mobile charges can completely drift into contacts via the wide-gap layer. It can be seen from the figure that the size of the region where the multiplication coefficient is reduced appreciably as a result of charge flow, depends on the resistance of the wide-gap layer. For example, when the resistance of the wide-gap layer is $R_0=50\ \Omega\cdot$m$^2$, which corresponds to a resistivity $5\times10^{10}$ $\Omega\cdot$cm for $d=0.1$ $\mu$m, the radius of the photoconductor region with reduced multiplication coefficient exceeds $500\mu$m.

Thus, in order to obtain a uniform multiplication coefficient over the entire sensitive area of the device, measures must be taken to prevent charge flow along the semiconductor–wide-gap layer interface. One method of preventing this flow is to form separate $p$–$n$-junctions, having dimensions of 2–3 $\mu$m and separated by intervals of 5 $\mu$m, on the semiconductor surface. The results of experiments presented in Ref. 8 indicate that the spread of the signal multiplication coefficient in this type of photodetector does not exceed 10% with an average of $M=5\times10^3$.

[1] A. Goetzberger and E. H. Nicollian, Appl. Phys. Lett. **9**, 444 (1966).
[2] A. B. Kravchenko, A. F. Plotnikov, Yu. M. Popov, and V. É. Shubin, Kvantovaya Elektron. (Moscow) **8**, 785 (1981) [Sov. J. Quantum Electron. **11**, 473 (1981)].
[3] A. Ya. Vul', A. T. Dideikin, A. V. Sachenko, and A. I. Shkrebtii, Pis'ma Zh. Tekh. Fiz. **14**, 1729 (1988) [Sov. Tech. Phys. Lett. **14**, 751 (1988)].
[4] A. G. Gasanov, V. M. Golovin, Z. Ya. Sadygov, and N. Yu. Yusipov, Pis'ma Zh. Tekh. Fiz. **14**, 706 (1988) [Sov. Tech. Phys. Lett. **14**, 313 (1988)].
[5] Z. Y. Sadygov, I. M. Zheleznykh, and T. A. Kirillova, Appl. Surf. Sci. **92**, 575 (1995).
[6] V. V. Pospelov *et al.*, Mikroelektronika **3**, 475 (1974).
[7] S. M. Sze, *Physics of Semiconductor Devices* (Wiley, New York, 1969) [Russ. transl., Énergiya, Moscow, 1973].
[8] Z. Y. Sadygov, I. M. Zheleznykh, N. A. Malakhov *et al.*, IEEE Trans. Nucl. Sci. **43**, 1009 (1996).

Translated by R. M. Durham

# Physical model of the influence of oversize impurities on the radiation hardening of iron $\alpha$-alloys

V. V. Rybin and Yu. V. Trushin

*A. F. Ioffe Physicotechnical Institute, Russian Academy of Sciences, St. Petersburg*
(Submitted February 5, 1997)
Pis'ma Zh. Tekh. Fiz. **23**, 77–83 (April 26, 1997)

A physical model is proposed for the influence of oversize impurities on the characteristics of radiation-defect formation in neutron-irradiated iron alloys at low and high irradiation temperatures. A comparison is made between the theoretical expressions obtained for radiation hardening at different temperatures and the existing experimental data. For low temperatures, the agreement was satisfactory, so we can estimate one of the microscopic parameters of impurity atoms — the relative size of the region of influence of the impurity atoms. For high irradiation temperatures, the behavior of the radiation hardening of an alloy with oversize impurities is predicted as a function of impurity size. © *1997 American Institute of Physics.* [S1063-7850(97)03004-8]

Experimental studies of the influence of oversize impurities, W, Ti, Ta, Nb, and others, on the radiation hardening ($\Delta\sigma$) of iron $\alpha$-alloys have revealed[1,2] that at high irradiation temperatures ($\sim$300 °C), the value of $\Delta\sigma$ is lower than that at low temperatures ($\sim$50 °C). In the present paper, we propose a physical model to explain this decrease, based on the kinetics of radiation point defects at various temperatures in the presence of large-radius impurities.

Mutual recombination of vacancies and interstitial atoms reduces the total number of radiation defects and therefore reduces the radiation hardening $\Delta\sigma$, which depends on the concentration of residual radiation defects, slowing down the dislocations.[3–5] By creating fields of compressive stresses around themselves, under irradiation these oversize impurities, in the same way as coherent pre-precipitates,[6–9], promote additional migration of interstitial atoms from their regions of influence (A) to a region I between the impurities. This creates conditions for enhanced recombination of vacancies with interstitial atoms in region I. In addition, oversize impurities ($j$) may trap vacancies ($v$) to form vacancy–impurity ($vj$) complexes. Thus, some of the vacancies may combine in fixed complexes which act as ''stoppers'' for the motion of dislocations. At elevated temperatures however, these complexes may dissociate with the release of vacancies. The recombination in regions I should then be even more vigorous but the impurities (on average) remain free from vacancies and their contribution to the slowing of the dislocations will be typical of the initial unirradiated material.

We consider the case of a neutron-irradiated alloy at low temperatures ($T_1=323$K). We then assume that: 1) the vacancies ($v$) are fixed and trapped by impurities to form vacancy–impurity ($vj$) complexes, 2) mobile interstitial atoms ($i$) recombine with vacancies, 3) interstitial atoms migrate from the compressed regions A around impurities into region I, and 4) the $vj$ complexes are sinks for interstitial atoms.

By virtue of assumption 3), the rates of generation $g_k^{\mathrm{I}}$ (in region I) of interstitial atoms ($k=i$) and vacancies ($k=v$) can be written as (see Refs. 9–11)

$$g_i^{\mathrm{I}}=g+\delta_i, \quad g_v^{\mathrm{I}}=g, \tag{1}$$

where $g$ is the rate of generation of Frenkel pairs in the undeformed material, $\delta_i$ describes the additional migration of interstitial atoms from regions A to region I:

$$\delta_i=\vartheta_j\delta_{vj}^{\mathrm{A}}; \quad \delta_{vj}^{\mathrm{A}}=g\cdot(r_{\mathrm{Fe}}/R_{vj})^{\beta},$$

$$\vartheta_{vj}=\int V(R_{\mathrm{A}}')f(R_{\mathrm{A}}')dR_{\mathrm{A}}'$$

$$=V(R_{\mathrm{A}})\rho_n C_j$$

$$=(4\pi/3)(R_{vj}^3-r_{\mathrm{Fe}}^3)\rho_n C_j \tag{2}$$

is the volume fraction of regions A, $V(R_{\mathrm{A}})$ is the volume and $f(R_{\mathrm{A}})$ is the size distribution function of regions A with the radius

$$R_{vj}=r_{\mathrm{Fe}}+\Delta r_j+r_{vj}^c=r_{\mathrm{Fe}}[1+(\Delta r_j+r_{vj}^c)/r_{\mathrm{Fe}}] \tag{3}$$

for vacancy-impurity complexes, $r_{\mathrm{Fe}}$ is the radius of an iron atom, $\Delta r_j=r_j-r_{\mathrm{Fe}}$, $r_j$ is the radius of an impurity of species $j$, $r_{vj}^c$ is the size of the region of influence of a vacancy–$j$-impurity complex, $C_j$ is the relative concentration of impurities of species $j$, $\rho_n$ is the nuclear density of the matrix, and $\beta$ is an exponent. The quantity $\delta_i$ may be expressed as

$$\delta_i=g\varphi_{vj},$$

$$\varphi_{vj}=(\pi/2)C_j\frac{\Delta r_j+r_{vj}^c}{r_{\mathrm{Fe}}}[1+(\Delta r_j+r_{vj}^c)/r_{\mathrm{Fe}}]^{1-\beta}. \tag{4}$$

Since the radiation hardening $\Delta\sigma(\Phi)$ reaches steady-state values for irradiation doses of the order $\Phi\approx10^{21}n\cdot\mathrm{cm}^{-2}\mathrm{s}^{-1}$ (i.e., for irradiation times of $\approx10^8$ s), it may be postulated that the defect concentrations $C_k$ are also steady-state.

Solving a system of steady-state balance equations (see, for example, Refs. 9–11) for the concentrations of vacancies ($C_v^{\mathrm{I}}$), interstitial atoms ($C_i^{\mathrm{I}}$), impurities ($C_j^{\mathrm{I}}$), and vacancy–

impurity complexes ($C_{vj}^{\mathrm{I}}$), it can be shown that almost all the oversize impurities form complexes with vacancies, i.e.,

$$C_{vj}^{\mathrm{I}} \approx \rho_n C_j . \tag{5}$$

Thus, at the temperature $T_1$ the defects formed by irradiation, at which dislocations will undergo further slowing, should be considered to be: vacancy–impurity complexes ($k=vj$), vacancies ($k=v$), and interstitial atoms ($k=i$). The total concentration of radiation-induced defects will therefore be

$$\sum_k C_k^{\mathrm{I}} = C_{vj}^{\mathrm{I}} + C_v^{\mathrm{I}} + C_i^{\mathrm{I}} . \tag{6}$$

At high temperatures $T_2 = 573$ K, we assume that: 1) the vacancies are fixed, 2) vacancies do not form stable complexes with oversize impurities because of dissociation at high temperature;[1)] 3) vacancies and interstitial atoms recombine on impact, and 4) interstitial atoms migrate from compressed regions A (as at $T_1$) to region I.

Assuming steady-state conditions, as at low temperatures, we derive the following relations for the concentrations

$$C_i(T_2) = \frac{D_v(T_2)k_v^2}{D_i(T_2)k_i^2} C_v(T_2) + \frac{g\varphi_j}{D_i(T_2)k_i^2}, \tag{7}$$

$$C_v(T_2) = \frac{k_i^2}{2\mu}(1-\varphi_j\alpha_2)\left[\sqrt{1+\frac{4\alpha_2(1+\varphi_j)}{(1-\varphi_j\alpha_2)^2}}-1\right] - \frac{g\varphi_j}{D_v(T_2)k_v^2}, \tag{8}$$

where $D_k$ is the diffusion coefficient of defects of species $k$ ($k=i,v$), $k_k^2$ is the sum of the sink forces for defects of type $k$, $\mu = 4\pi r_R$, $r_R$ is the radius of spontaneous recombination of vacancies and interstitial atoms,

$$\alpha_2 = \mu g / D_v(T_2) k_v^2 k_i^2 ,$$

$$\varphi_j = (\pi/2) C_j \frac{\Delta r_j + r_j^c}{r_{\mathrm{Fe}}} [1 + (\Delta r_j + r_j^c)/r_{\mathrm{Fe}}]^{1-\beta} \quad (\text{see Eq. (4)}). \tag{9}$$

Thus, the total maximum concentration of radiation-induced defects at high temperatures $T_2$ is

$$\sum_k C_k = C_v + C_i . \tag{10}$$

Compared with the low temperature case [see Eq. (6)], the total concentration (10) is considerably lower on account of the increased recombination between vacancies ''released'' from impurities and additional interstitial atoms migrating from the regions A of influence of oversize impurities.

Analytic dependences $\Delta\sigma \propto (C_k)^n$ with the exponent $n<1$, were obtained for the radiation hardening $\Delta\sigma$ as a function of the absolute concentration $C_k$ of stoppers of type $k$. In some studies[12–15] this exponent is $n=1/2$ and in others (for example, Refs. 16–20), it is $n=1/3$.

We use the following expression for the total stress which must be overcome by the dislocations as they migrate through a field of stoppers of various types $k$

$$\sigma = Gb \sum_k \alpha_k (C_k R_k)^n , \tag{11}$$

where $\alpha_k$ is a coefficient allowing for the power of stoppers of type $k$, $R_k$ is the size (or radius) of the region occupied by a stopper of type $k$, $G$ is the shear modulus of the material, and $b$ is the Burgers vector.

For an alloy with oversize impurities $j$ at temperature $T_1$, using Eq. (6) we have

$$\Delta\sigma_j(T_1) = \sigma_j(T_1) - \sigma_j^0(T_1), \tag{12}$$

where

$$\sigma_j^0(T_1) = \sigma_{\mathrm{Fe}}^0(T_1) + \alpha_j Gb(\rho_n C_j R_j)^n ,$$

$$\sigma_j(T_1) = \sigma_{\mathrm{Fe}}^0(T_1) + \alpha_{vj} Gb(C_{vj}^{\mathrm{I}} R_{vj})^n + Gb\sum \alpha_k (C_k^{\mathrm{I}} R_k)^n , \quad k = v,i. \tag{13}$$

Then from Eq. (11), allowing for Eqs. (5) and (6), we write

$$\Delta\sigma_j(T_1) = \alpha_{vj} GbB_1 C_j^n [1 + (\Delta r_j + r_j^c)/r_{\mathrm{Fe}}]^n + Gb\sum_k \alpha_k (C_k' R_k)^n (C_k^{\mathrm{I}}/C_k')^n , \tag{14}$$

where

$$B_1 = (r_{\mathrm{Fe}}\,\rho_n)[(1 + \Delta r_{vj}^c / R_j)^n - \alpha_j/\alpha_{vj}]. \tag{15}$$

Obtaining from Eq. (14) the expression for the radiation hardening $\Delta\sigma_{\mathrm{Fe}}(T_1)$ of iron at temperature $T_1$ under the same assumptions as for the alloy, we write

$$\Delta\sigma_j(T_1) \approx \Delta\sigma_{\mathrm{Fe}}(T_1) + \alpha_{vj} GbB_1 C_j^n \times [1 + (\Delta r_j + r_j^c)/r_{\mathrm{Fe}}]^n . \tag{16}$$

Performing similar transformations for the high-temperature case, we have

$$\Delta\sigma_j(T_2) \approx \Delta\sigma_{\mathrm{Fe}}(T_2) - \alpha_v GbB_2 C_v^{\prime n} \frac{\Delta r_j + r_j^c}{r_{\mathrm{Fe}}} \times [1 + (\Delta r_j + r_j^c)/r_{\mathrm{Fe}}]^{1-\beta}, \tag{17}$$

where $C_v'$ is the concentration of vacancies in pure iron exposed to high-temperature irradiation,

$$B_2 = (\pi/2) n \sqrt{\alpha_2 r_{\mathrm{Fe}}^n C_j}.$$

By comparing the numerical values of the radiation hardening of the alloy at low temperatures as given by Eq. (16) (for $n=1/2$) and the experimental data[1,2] it is possible to

TABLE I. Relative changes in the size of the regions of influence $r_{vj}^c/a$ of vacancy–impurity complexes.

| $j$ | W | Ti | Ta | Nb |
|---|---|---|---|---|
| $\Delta r_j/a$ | 0.423 | 0.426 | 0.436 | 0.440 |

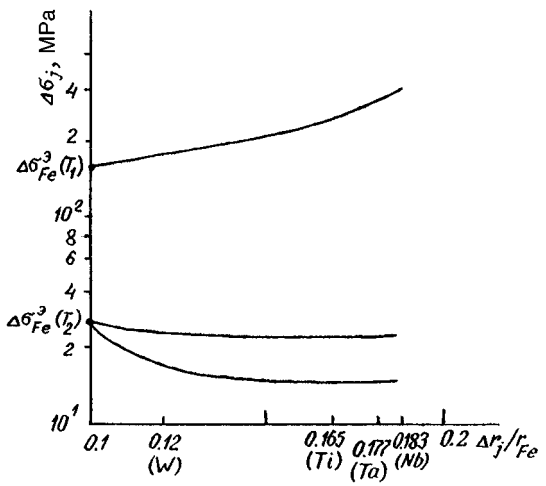


FIG. 1. Radiation hardening $\Delta\sigma_j$ of alloy versus $\Delta r_j/r_{\mathrm{Fe}}$ (the relative difference between the radii of impurity and iron atoms) for low ($T_1=323$ K) and high ($T_2=573$ K) temperatures for alloys with oversize impurities $j=$ W, Ti, Ta, and Nb ($\Delta\sigma_{\mathrm{Fe}}^{\mathrm{exp}}(T_1)$ and $\Delta\sigma_{\mathrm{Fe}}^{\mathrm{exp}}(T_2)$ are the experimental values of the radiation hardening of pure iron at temperatures $T_1$ and $T_2$).

estimate $r_{vj}^c$ [see Eq. (3)], by averaging over the concentrations $C_j$. The values of $r_{vj}^c/a$ are given in Table I ($a=2r_{\mathrm{Fe}}$ is the diameter of an Fe atom).

An example of the dependence of $\Delta\sigma_j$ on $\Delta r_j=r_j-r_{\mathrm{Fe}}$ [see Eq. (3)] is plotted in Fig. 1 for $T_1$ according to Eq. (16) and $T_2$ according to Eq. (17) for $C_j=0.6\times10^{-2}$.

It can be seen from Fig. 1 and formulas (16) and (17) that at low temperatures the radiation hardening $\Delta\sigma_j(T_1)$ of the alloy increases with increasing size of the impurity atoms because, as these atoms increase in size, they increasingly trap vacancies in compression regions. This results in the formation of stoppers for dislocations in the form of vacancy–impurity complexes, as is predicted by our model.

At high temperatures these complexes do not form, because of their high degree of dissociation. However, the larger the size of the impurity, the stronger the compressive elastic field it creates around itself (region A). This means that the impurity more forcefully ''expels'' interstitial atoms from its neighborhood and these atoms additionally migrate into region I between the impurity atoms. This serves to intensify the recombination between interstitial atoms and free vacancies, which at high temperatures are not bound in complexes with impurities. On account of this anomalous recombination, the concentrations of radiation-induced defects decrease and the radiation hardening is reduced, the effect being greater, the larger the impurity atoms. Figure 1 shows radiation hardening curves $\Delta\sigma_j(T_2)$ for two values of the exponent $\beta$ [see Eq. (9)]: $\beta=1$ and $\beta=2$. The exponent $\beta$ is responsible for the type of decay with distance exhibited by the elastic field of an oversize impurity. It can be seen that as the decay of the compressive field of the impurity becomes slower, the radiation hardening of the alloy decreases more rapidly.

To sum up, a physical model has been proposed for the influence of oversize impurities on the formation characteristics of radiation-induced defects in neutron-irradiated iron alloys for low ($T_1$) and high ($T_2$) irradiation temperatures. The theoretical expressions obtained for the radiation hardening at different temperatures were compared with the experimental data. Satisfactory agreement was obtained for low temperatures, which enabled us to estimate one of the microscopic parameters of impurity atoms — the relative value $r_{vj}^c/a$ of the sizes of the regions of influence of the impurity atoms. For high temperatures the behavior of the radiation hardening of an alloy with oversize impurities was predicted as a function of impurity size.

[1)]Then, the radius of region A will be $R_j=r_{\mathrm{Fe}}+\Delta r_j+r_j^c$, where $r_j^c$ is the size of the region of influence of an impurity atom of species $j$.


[1] V. A. Nikolaev and V. V. Rybin, Vopr. Mater. No. 1, 40 (1995).
[2] V. A. Nikolaev and V. V. Rybin, Proc. First Intern. Symposium on Effects of Radiation on Materials, edited by D. S. Gelles, P. K. Nanstad, A. S. Kumar, and E. A. Little (ASTM, USA, 1196), pp. 3–24.
[3] A. Seeger, in *Radiation Damage in Solids* (IAEA, Vienna, 1962), p. 531.
[4] R. L. Fleischer, J. Appl. Phys. **33**, 3504 (1962).
[5] T. J. Koppenaal and R. I. Arsenault, Metall. Rev. **16**, No. 157, 175 (1971).
[6] A. M. Parshin and Yu. V. Trushin, Pis'ma Zh. Tekh. Fiz. **9**, 561 (1983) [Sov. Tech. Phys. Lett. **9**, 243 (1983)].
[7] A. N. Orlov, A. M. Parshin, and Yu. V. Trushin, Zh. Tekh. Fiz. **53**, 2367 (1983) [Sov. Phys. Tech. Phys. **28**, 1455 (1983)].
[8] A. N. Orlov, G. G. Samsonidze, and Yu. V. Trushin, Zh. Tekh. Fiz. **56**, 1311 (1986) [Sov. Phys. Tech. Phys. **31**, (1986)].
[9] Yu. V. Trushin, Zh. Tekh. Fiz. **57**, 226 (1987) [Sov. Phys. Tech. Phys. **32**, 136 (1987)].
[10] Yu. V. Trushin, Zh. Tekh. Fiz. **62**(4), 1 (1992) [Sov. Phys. Tech. Phys. **37**, 353 (1992)].
[11] Yu. V. Trushin, *Theory of Radiation Processes in Metal Solid Solutions* (Nova Science Publishers, New York, 1996).
[12] J. C. Wilson, Proc. Intern. Conf. on Peaceful Uses of Atomic Energy, New York, 1958, Vol. 5, p. 43.
[13] J. Diehl, in *Radiation Damage in Solids*, Vol. 1 (IAEA, Vienna, 1963), p. 129.
[14] T. H. Blewitt, C. A. Arenberg, A. C. Klank, and T. Scott, Proc. Intern. Conf. on Vacancies and Interstitials in Metals, Julich, 1968, Vol. 2, p. 547.
[15] E. A. Little, Ind. Metall. Rev. **21**(3), 25 (1976).
[16] T. H. Blewitt, R. R. Coltmann, R. E. Jamison, and J. K. Redman, J. Nucl. Mater. **2**, 277 (1960).
[17] D. K. Holmes, in *The Interaction of Radiation with Solids* (Amsterdam, 1964), p. 147.
[18] I. E. W. Young and F. A. Sherrill, Can. J. Phys. **45**, 757 (1967).
[19] D. O. Thompson, Proc. Symposium on The Interaction Between Dislocations and Point Defects, AERE-R-5944 (UKAEA, 1968), Part. IV, p. 152.
[20] A. N. Orlov and Yu. V. Trushin, Fiz. Met. Metalloved. **41**, 925 (1976).


Translated by R. M. Durham

# Thermocapillary mechanism of pore evaporation during sintering and crystallization of $YBa_2Cu_3O_{7-\delta}$

S. A. Churin

*Institute of Microstructure Physics, Russian Academy of Sciences, Nizhniĭ Novgorod*
(Submitted December 16, 1996)
Pis'ma Zh. Tekh. Fiz. **23**, 85–89 (April 26, 1997)

The thermocapillary effect is used to explain the phenomenon of shrinkage observed during the annealing of $YBa_2Cu_3O_{7-\delta}$ components. The proposed model can be used to estimate the characteristic time taken for pores to reach the surface of ceramic samples. © *1997 American Institute of Physics.* [S1063-7850(97)03104-2]

One method of crystallizing $YBa_2Cu_3O_{7-\delta}$ involves partial melting followed by slow cooling of the samples in furnaces with a temperature gradient.[1,2] The samples are prepared by pressing stoichiometric powder into suitable shapes. Immediately after pressing, the sample is placed in a muffle furnace where it is sintered at temperatures of $900-960°C$ for several hours. During the sintering process the density of the sample increases from 3–3.5 $g\cdot cm^{-3}$ to 4–5 $g\cdot cm^{-3}$. A further increase in density is then achieved in crystallization furnaces. Observations reveal that the rate of shrinkage is highest at the start of annealing or crystallization. At a temperature gradient of 5 $°C\cdot min^{-1}$ in the range $800-940°C$, the sintering process is mainly completed within 30 min. The shrinkage time during the crystallization process is 0.5–1.5 h at $\sim 1000°C$. Annealing of the samples followed by crystallization is accompanied by various phenomena. First, as has been noted above, the density of the sample increases because of a reduction in the volume occupied by the pores. Second, when cylindrical samples are annealed, changes in the geometry occur on account of the external diameter. Third, a deviation from stoichiometry is observed — a green deposit appears on the outer surface of the cylinder (the $Y_2BaCuO_5$ phase is formed). Fourth, the onset of shrinkage and the formation of the $BaCuO_2$ and CuO phases is observed at the same temperature.

This combination of phenomena may be explained by means of the thermocapillary effect. The thermocapillary drift of air bubbles in water was studied in Ref. 3, and droplets of a viscous liquid in another liquid filling the entire space were considered in Ref. 4. In the present case, we propose a model to determine the drift velocity of a pore in a partially molten sample, where the dependence of the surface tension, not only on temperature but also on the concentration of the liquid phase, must be taken into account.

We consider an isolated pore in a $YBa_2Cu_3O_{7-\delta}$ ceramic, situated in a field with a temperature gradient (see Fig. 1). At this point, it should be noted that during external heating, a temperature gradient will always exist in the cross section of the sample because of its finite thermal conductivity. For simplicity, we assume that the pore is a cylinder of length $l$ and radius $R_0$ and we assume that the temperature $T_2$ exceeds the incongruent melting temperature of the $YBa_2Cu_3O_{7-\delta}$ ceramic. We also postulate that the $BaCuO_2$ and CuO phases are formed as a result of incongruent melting.

In this case, the surface of the pore begins to be coated with a layer of liquid phase and since $d\alpha/dT \leqslant 0$ ($\alpha$ is the surface tension), a shearing stress begins to act on the incipient surface of the liquid phase, inducing a flow of the liquid phase along the surface of the pore into the lower-temperature zone. To determine the velocity of the liquid phase, the following hydrodynamic equation can be written in cylindrical coordinates:

$$\eta \frac{1}{r}\frac{d}{dr}\left(r\frac{\partial v_z}{\partial r}\right)=0 \tag{1}$$

with the boundary conditions

$$v_z|_{r\to\infty}=0, \tag{2}$$

$$\eta \frac{\partial v_z}{\partial r}|_{r=R_0}=-\frac{d\alpha}{dz}, \tag{3}$$

where $\eta$ is the viscosity of the liquid and $v_z(r)$ is the velocity of the liquid phase. Here we neglect any change in the density and viscosity of the liquid over the volume. The solution of Eq. (1) with the boundary conditions (2) and (3) is given by the function:

$$v_z(r)=-\frac{R_0}{\eta}\frac{d\alpha}{dz}\ln r + C_2. \tag{4}$$

From the first boundary condition we obtain an expression for $C_2$:

$$C_2=\frac{R_0}{\eta}\frac{d\alpha}{dz}\ln(nR_0). \tag{5}$$

Here, $n \geqslant 1$ characterizes the region involved in forming the flow of liquid phase. It is assumed that the liquid phase flows over the surface of the pore and thus no divergence occurs at the point $r=0$. The inclusion of points $r=0$ within the limits of integration would also imply that there is no pore at the given point. Finally, we obtain the following expression for $v_z(r)$:

$$v_z(r)=-\frac{R_0}{\eta}\frac{d\alpha}{dz}\ln\frac{nR_0}{r}. \tag{6}$$

We define the flow rate of the liquid phase per unit time per unit pore length as:

 1063-7850/97/040329-02$10.00  

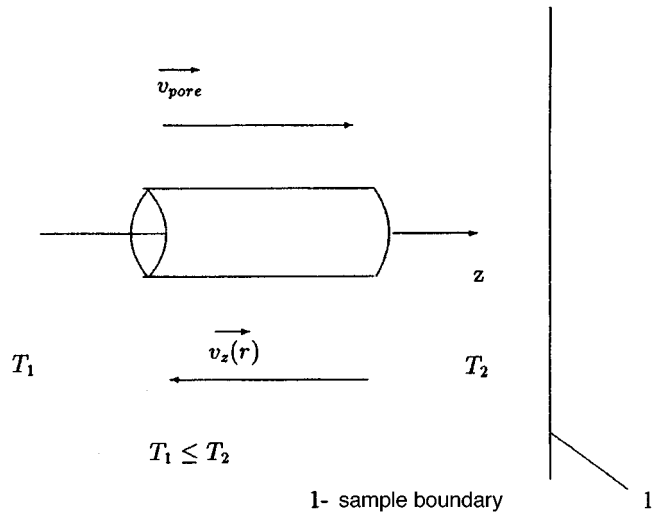


FIG. 1.

$$\Delta Q = \int_{R_0}^{nR_0} v_z(r)\,dr. \tag{7}$$

The lower limit of integration coincides with the pore radius (we neglect the thickness of the film on the pore surface) while the upper limit is defined as half the distance from a neighboring pore. After integrating, we obtain

$$\Delta Q = \pi\rho R_0^3 \frac{1}{\eta}\frac{d\alpha}{dz}\left(\frac{1}{2}(n^2-1)-\ln n\right), \tag{8}$$

where $\rho$ is the density of the liquid phase. From Eq. (8) we obtain the pore velocity

$$v_{\text{pore}} = \frac{R_0}{\eta}\frac{d\alpha}{dz}\left(\frac{1}{2}(n^2-1)-\ln n\right). \tag{9}$$

In expression (9) we have

$$\frac{d\alpha}{dz} = \frac{\partial\alpha}{\partial T}\frac{dT}{dz} + \frac{\partial\alpha}{\partial C_l}\frac{dC_l}{dz}, \tag{10}$$

where $C_l$ is the concentration of the liquid phase. Expression (9) can be used for a numerical check of the proposed model of pore evaporation during the sintering and crystallization of samples of the high-temperature superconductor $YBa_2Cu_3O_{7-\delta}$. We find the velocity of a pore of radius $R_0 = 10^{-5}$ m in a field with the temperature gradient $20°\text{C}\cdot\text{cm}^{-1}$ for the case where $\eta = 100\ \text{Ncm}^{-2}$ (Ref. 5) and $\partial\alpha/\partial T = -1\ \text{g}\cdot\text{s}^{-2}\text{K}^{-1}$, neglecting $\partial\alpha/\partial C_l$ and setting $n = 2$. We find that $v_{\text{pore}} \simeq 2\times 10^{-7}\ \text{m}\cdot\text{s}^{-1}$. We assume that the characteristic distance which must be covered by a pore before it reaches the surface is 2 mm. We then find that the annealing time is $10^4$ s, which is of the same order of magnitude as the observed value. The severalfold difference may be explained by the fact that we neglected $\partial\alpha/\partial C_l$ and we disregarded the pore size distribution in the bulk of the sample. It should be borne in mind that as the pores move, they increase in size by merging with smaller pores. Thus, the pore velocity increases and the time taken for the pore to leave the sample decreases. The proposed model may be used to assess the loss of stoichiometry by $YBa_2Cu_3O_{7-\delta}$ targets in the course of their fabrication and utilization.

This work was carried out under Project 95032 in the ''Superconductivity'' category of the program ''Topical Problems in the Physics of Condensed Media.''

[1] P. J. McGinn, M. A. Black, and A. Valenzuela, Phys. C **156**, 57 (1988).
[2] S. Jin, T. H. Tiefel, R. S. Sherwood *et al.*, Appl. Phys. Lett. **52**, 2074 (1988).
[3] Yu. K. Bratukhin, O. A. Ovdokimova, and A. F. Pshenichnikov, Izv. Akad. Nauk SSSR Mekh. Zhid. Gaz. No. 5, 55 (1979).
[4] Yu. K. Bratukhin, Izv. Akad. Nauk SSSR Mekh. Zhid. Gaz. No. 5, 156 (1975).
[5] A. V. Belyĭ, N. G. Makarova, T. M. Dmitruk *et al.*, Sverkhprovodimost' (KIAE) **8**, 790 (1995) [Superconductivity **8**, (1995)].

Translated by R. M. Durham

# AlGaAs/GaAs-heterostructure cw laser diodes with a working output optical power of 3 W ($\lambda = 0.81 \mu$m) and an operating life of 2000 hours

D. M. Demidov, N. I. Katsavets, R. V. Leus, A. L. Ter-Martirosyan, and V. P. Chalyĭ

*ZAO ''Semiconductor Devices,'' St. Petersburg*
(Submitted February 5, 1997)
Pis'ma Zh. Tekh. Fiz. **23**, 90–94 (April 26, 1997)

Quantum-well AlGaAs/GaAs heterostructures with separate confinement have been used to fabricate laser diodes emitting at 0.81 $\mu$m, with a cw output optical power of 4 W and an operating life of more than 2000 h at a power of 3 W and a temperature of +20 °C. © *1997 American Institute of Physics.* [S1063-7850(97)03204-7]

High-power laser diodes are being increasingly widely used in various fields of medicine (ophthalmology, surgery, and oncology), quantum electronics (as pump sources for solid-state lasers), robotics, geology, spectroscopy, and other areas, because of their small size and weight, their high efficiency, low energy consumption, and the feasibility of directly modulating the radiation intensity. The problems of increasing the output optical power and the operating life of these laser diodes are therefore top-priority. The present paper is a continuation of a series of studies[1–3] and deals with the development of high-power cw laser diodes having an operating life of several thousand hours.

The laser diodes were fabricated using quantum-well AlGaAs/GaAs heterostructures with separate confinement, grown by molecular-beam epitaxy. A detailed description of these heterostructures and their growth conditions can be found in Ref. 1.

The laser diodes consisted of three stripe emitters, integrated on a single substrate but not optically coupled. Each emitter comprised a phased laser array, constructed on the ''shallow mesa with additional insulation'' principle, with an interstripe optical coupling coefficient regulated by varying the etching depth of the mesa.[2] Profiled heterostructures were produced by ion etching via a photoresistive mask, using a partially neutralized, collimated beam of up to 1000 eV argon ions. The total width of the emitting area of the laser diode was 550 $\mu$m. A reflecting coating (reflection coefficient higher than 95%) was deposited on the rear face of the laser diode, while the front face had an antireflection coating (reflection coefficient around 10%). After the coatings had been deposited on the cavity mirrors, the laser diodes were soldered to a nickel-plated copper heat sink with the $p$-layers facing downward.

A calibrated Coherent LaserMate power meter was used to measure the power-current characteristics, spectral measurements were made using a KSVU-23M spectral complex, and an apparatus described in Ref. 4 was used for near- and far-field measurements.

Figure 1a shows power-current characteristics of the fabricated laser diodes operating in the cw mode at heat sink temperatures of + 20 °C and + 52 °C. The maximum optical output power ($P$) without any appreciable deterioration in the differential quantum efficiency was 4 W at +20 °C and 3 W at +52 °C. In this case, the threshold currents ($I_{th}$) were 1200 mA ($j_{th} = 240$ A/cm$^2$) and $I_{th}$ 1600 mA ($j_{th} = 320$ A/cm$^2$), and the differential quantum efficiencies were 45% and 40% at heat sink temperatures of +20 °C and +52 °C, respectively. The width of the lasing spectrum at half-maximum was less than 2 nm (see Fig. 1b), so that these

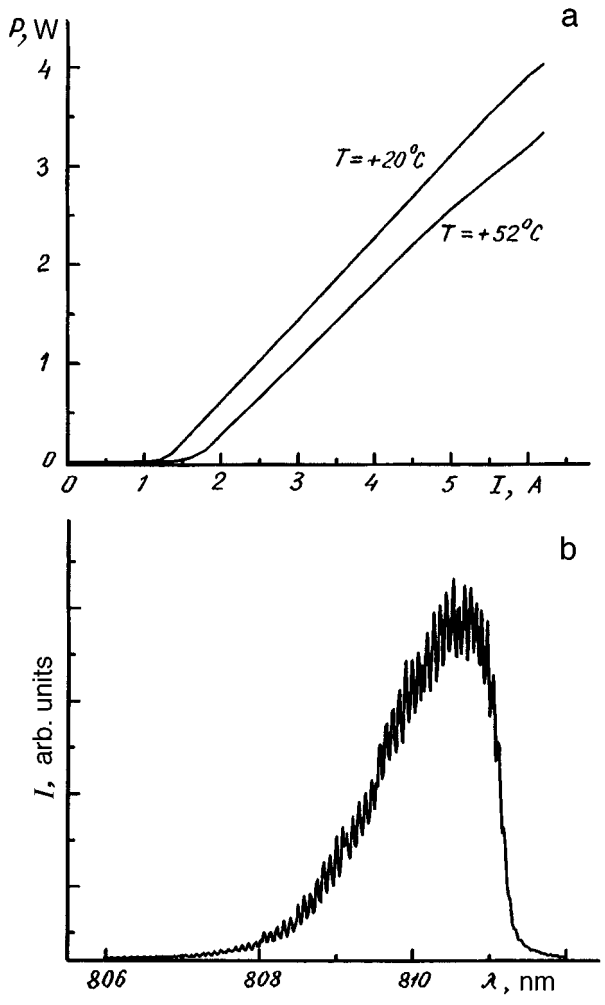


FIG. 1. Watt–ampere characteristics of cw laser diodes at different temperatures (a) and typical lasing spectrum of a three-stripe laser diode at a pump current of 5 A and a temperature of 20 °C (b).

 1063-7850/97/040331-02$10.00  

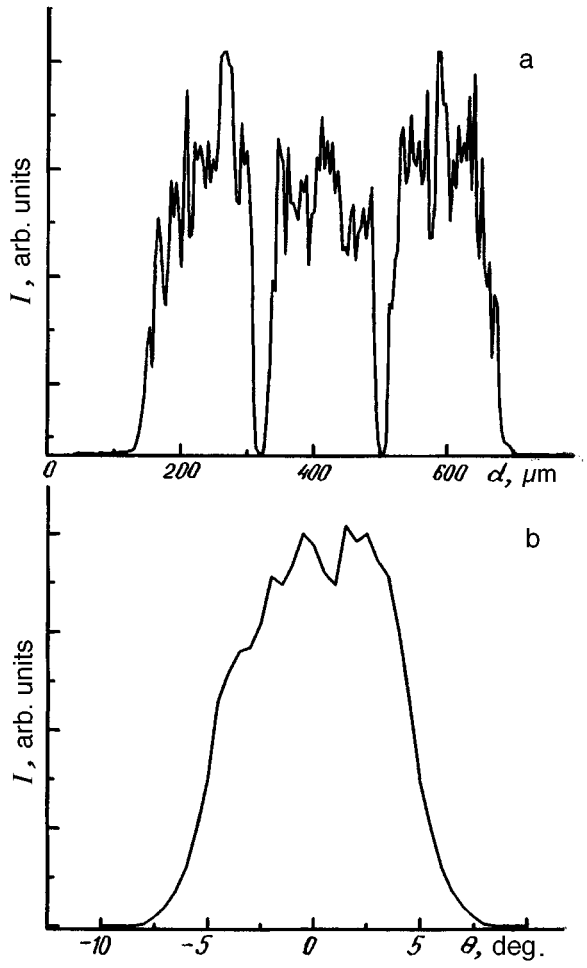


FIG. 2. Typical characteristics of a three-stripe laser diode at a pump current of 5 A and a temperature of 20 °C: a — near field and b — far field.

laser diodes can be used for efficient pumping of $Nd^{3+}$ ions in YAG:Nd solid-state lasers.

Near-field measurements (shown in Fig. 2a) revealed that the optical flux intensity was almost the same in all three emitters, which suggests that the parameters of the laser heterostructure are highly uniform. Since the high-power laser diodes were fabricated using phased arrays with a low interstripe optical coupling coefficient, a typical far-field pattern (Fig. 2b) comprised the weakly modulated field of an individual component of the phased array.

To determine their operating life, the laser diodes were tested at an elevated heat sink temperature of +52 °C and an output optical power of 3 W for 100 h, which corresponds to 2000 h at +20 °C (Ref. 5). The decrease in the optical power of the laser diodes after testing did not exceed 2%.

To sum up, we have succeeded in fabricating and investigating high-power laser diodes ($P=4$ W, $\lambda=0.81$ $\mu$m) with an operating life longer than 2000 h. These diodes are extremely interesting for efficient pumping of $Nd^{3+}$ ions in YAG:Nd solid-state lasers.

[1] S. Yu. Karpov, G. de la Cruz, V. E. Myachin *et al.*, Pis'ma Zh. Tekh. Fiz. **17**(7), 31 (1991) [Sov. Tech. Phys. Lett. **17**, 248 (1991)].
[2] V. P. Chaly *et al.*, Semicond. Sci. Technol. **11**, 372 (1996).
[3] V. P. Chaly *et al.*, Semicond. Sci. Technol. **9**, 345 (1994).
[4] G. A. Gavrilov *et al.*, Pis'ma Zh. Tekh. Fiz. **17**(19), 1 (1991) [Sov. Tech. Phys. Lett. **17**, 681 (1991)].
[5] G. Thompson, *Physics of Semiconductor Laser Devices* (Wiley, New York, 1980), pp. 28–29.

Translated by R. M. Durham